UNIVERSITY OF CALIFORNIA

Los Angeles

Four-wave Mixing of Gigawatt power, Long-wave Infrared Radiation in Gases and

Semiconductors

A dissertation submitted in partial satisfaction of the requirements for the degree Doctor of

Philosophy in Electrical Engineering

by

Jeremy James Pigeon

2017

ABSTRACT OF THE DISSERTATION

Four-wave Mixing of Gigawatt power, Long-wave Infrared Radiation in Gases and

Semiconductors

by

Jeremy James Pigeon

Doctor of Philosophy in Electrical Engineering

University of California, Los Angeles, 2017

Professor Chandra J. Joshi, Chair

The nonlinear optics of gigawatt power, 10 μm, 3 and 200 ps long pulses propagating in gases and semiconductors has been studied experimentally and numerically. In this work, the development of a high-repetition rate, picosecond, CO_2 laser system has enabled experiments using peak intensities in the range of $1-10$ GW/cm^2, approximately one thousand times greater than previous nonlinear optics experiments in the long-wave infrared (LWIR) spectral region.

The first measurements of the nonlinear refractive index of the atomic and molecular gases Kr, Xe, N_2, O_2 and the air at a wavelength near 10 μm were accomplished by studying the four-wave mixing (FWM) of dual-wavelength, 200 ps CO_2 laser pulses. These measurements indicate that the nonlinearities of the diatomic molecules N_2, O_2 and the air are dominated by the molecular contribution to the nonlinear refractive index.

Supercontinuum (SC) generation covering the infrared spectral range, from $2-20\,\mu$m, was realized by propagating 3 ps, 10 μm pulses in an approximately 7 cm long, Cr-doped GaAs crystal. Temporal measurements of the SC radiation show that pulse splitting accompanies the generation of such broadband light in GaAs. The propagation of 3 ps, 10 μm pulses in GaAs was studied numerically by solving the Generalized Nonlinear Schrödinger Equation (GNLSE). These simulations, combined with analytic estimates, were used to determine that stimulated Raman scattering combined with a modulational instability caused by the propagation of intense LWIR radiation in the negative group velocity dispersion region of GaAs are responsible for the SC generation process.

The multiple FWM of a 106 GHz, 200 ps CO_2 laser beat-wave propagating in GaAs was used to generate a broadband FWM spectrum that was compressed by the negative group velocity dispersion of GaAs and NaCl crystals to form trains of high-power, picosecond pulses at a wavelength near 10 μm. Experimental FWM spectra obtained using 165 and 882 GHz beat-waves revealed an unexpected and rapid decrease in the FWM yield that was not predicted by the GNLSE model that accounts for third-order nonlinearities alone. These results suggest that the effective nonlinear refractive index of GaAs, having formidable second- and third-order susceptibilities, may be altered by quadratic nonlinearities.

The dissertation of Jeremy James Pigeon is approved.

Benjamin Williams

Jia-Ming Liu

Christoph Niemann

Warren B. Mori

Chandra J. Joshi, Committee Chair

Dedication

To my family and friends, thank you for your support and understanding.

TABLE OF CONTENTS

LIST OF FIGURES

LIST OF TABLES

ACKNOWLEDGEMENTS

I would like to thank my advisor, Professor Chan Joshi, for giving me the opportunity to work for an incredible research group. Without Professor Joshi's leadership, wisdom, and enthusiasm, this work would not have been possible. I am tremendously grateful to Dr. Sergei Tochitsky for recruiting me to the UCLA laser-plasma group and for the invaluable, daily mentorship and guidance he has provided me over the years. Everything I have become as an experimental scientist I owe to Dr. Tochitsky and, without his expertise, none of the experiments presented in this dissertation would have been possible. I would also like to thank Ken Marsh, Dr. Chris Clayton, and Professor Warren Mori for their mentorship and incredibly useful advice over the years.

I would like to extend my gratitude to those graduate students with whom I have "served in the trenches": Dr. Daniel Haberberger, Dr. Chao Gong, Eric Welch and Daniel Matteo. A special thanks goes to Dan Haberberger and Chao Gong both for their friendship and all that they taught me about working in the lab. I would like to thank Dr. Jessie Shaw and Professor Navid Vafaei-Najafabadi for their camaraderie and support, particularly while working through the first year of advanced courses at UCLA. Thank you also to Dr. Nuno Lemos, Dr. Chaojie Zhang and Chen-Kang Huang for their friendship and support. Last but not least, I would like to thank Maria Guerrero and Michelle Phan for their support, administrative and otherwise.

VITA

2008   B.S. Physics and B.S. Health Physics

       Bloomsburg University of Pennsylvania, Bloomsburg, Pennsylvania

2014   M.S. Electrical Engineering

       University of California at Los Angeles, Los Angeles, California

PUBLICATIONS

J.J. Pigeon, S. Ya. Tochitsky, E.C. Welch and C. Joshi (2016). *Measurements of the nonlinear refractive index of air, N_2, and O_2 at 10 µm using four-wave mixing*. Optics Letters, Vol. 41, No. 17, 3924-3927. (Editor's pick)

C. Gong, S. Ya. Tochitsky, F. Fiuza, J.J. Pigeon and C. Joshi (2016). *Plasma dynamics near critical density inferred from direct measurements of laser hole boring*. Physical Review E., Vol. 93, 061202.

J.J. Pigeon, S. Ya. Tochitsky and C. Joshi (2015). *High-power, mid-infrared, picosecond pulses generated by compression of a CO_2 laser beat-wave in GaAs*. Optics Letters, Vol. 40, No. 24, 5730-5733.

J.J. Pigeon, S. Ya. Tochitsky, C. Gong and C. Joshi (2014). *Supercontinuum generation from 2 to 20 μm in GaAs pumped by picosecond CO$_2$ laser pulses*. Optics Letters, Vol. 39, No. 11, 3246-3249.

S. Ya Tochitsky, J.J. Pigeon, D.J. Haberberger, C. Gong and C. Joshi. (2012). *Amplification of 3 ps pulses in an Atmospheric CO$_2$ Laser Using ac Stark Effect*. Optics Express, Vol. 20, No. 13, 13762-13768.

W. Luo, F. Shabbir, C. Gong, C. Gulec, J. Pigeon, J. Shaw, A. Greenbaum, S. Tochitsky, C. Joshi and A. Ozcan. (2015). *High throughput on-chip analysis of high-energy charged particle tracks using lensfree imaging*. Applied Physics Letters, Vol. 106 151107.

Chapter 1

Introduction

With the advent of the pulsed laser in the 1960s, it became possible to generate focused intensities on the order of 1 MW/cm^2 corresponding to transverse electric fields of ~ 3x10^6 V/m. For such strong fields, the propagation of radiation through a transparent dielectric can no longer be described by a polarizability that scales linearly with the applied field. As the driving field strength becomes a sufficient fraction of the field that binds the electron to the nucleus, the response of the electrons in the dielectric becomes anharmonic. The coupling of aharmonic electron motion to the driving field can manifest as a myriad of nonlinear phenomena such as harmonic generation, self-focusing and self-phase modulation. In order to describe such laser-matter interactions, a new field of optics emerged known as nonlinear optics.

Since the first observation of second harmonic generation by Franken *et. al.* in 1961 [1], the usefulness of nonlinear optics as a method to coherently change the wavelength of laser light has motivated extensive research on the subject. Using nonlinear optics for bandwidth manipulation, scientists have been able to broaden the spectrum of a laser pulse in order to generate so called "white-light" or supercontinuum [2, 3] for applications in spectroscopy and for the production of ultrafast optical pulses [4, 5]. As a tool for optical frequency conversion, researchers have used nonlinear optics to convert laser light from 1 μm to high-frequency X-rays [6, 7] down to the low-frequency terahertz range [8, 9]. Another important application of nonlinear optics is ultrashort pulse characterization by a variety of methods such as auto-correlation and frequency-resolved optical gating that all rely upon optical harmonic generation [10, 11].

The vast majority of the aforementioned studies have been performed in the range of 0.4 – 1 μm where high-power lasers are commercially available. Applications would benefit, however, from extending these studies to the middle infrared (mid-IR) spectral range. The range from 2 – 20 μm, the so-called "molecular fingerprint region", is of particular importance since these frequencies coincide with the rotational-vibrational resonances of most simple molecules. For the nonlinear optics of gases, the use of mid-IR light is advantageous since radiation in this range can propagate in the atmosphere with low loss. On the other hand, the mid-IR nonlinear optics of solids is incredibly interesting since the solids with the highest nonlinearities are only transparent in the mid-IR. For example, bulk semiconductors such as GaAs and CdTe have a nonlinear response one thousand times larger than that of common visible and near infrared materials such as glass or sapphire. These bulk semiconductors also exhibit low optical loss, a spectrally flat transmission curve and are available in large sizes making them ideal media for nonlinear optical applications.

Recently, intense mid-IR light has been used to generate X-ray radiation by high harmonic generation (HHG) since the cut-off of the HHG spectrum scales as $I\lambda^2$, where I is the intensity and λ is the wavelength of the drive laser. Here, 3.9 μm radiation focused to an intensity of 10^{14} W/cm^2 has been used to generate ~ 1 keV X-ray photons in gas-filled waveguides [12]. There is also burgeoning interest in the generation of such HHG spectra in solids where mid-IR drive lasers must be used to avoid irreversible damage to the dielectric. For this application, ~ 3 μm light focused to an intensity of 10^{12} W/cm^2 has been used for the generation of HHG photons in ZnO [13]. The growing interest in the interaction of intense mid-IR fields with gases and solids further motivates the need to study the nonlinear optical properties of these materials.

In this thesis, we present a series of experimental studies dedicated to the nonlinear optics of gases and semiconductors in the long-wave infrared (LWIR). Experiments were carried out using a picosecond CO_2 laser system at the UCLA Neptune laboratory that is capable of producing high-power, picosecond pulses with a central wavelength near 10 μm. For the work in this thesis, GW-class pulses at a pulse repetition rate of 1 Hz are focused to peak intensities of 1 – 10 GW/cm^2 to illicit optical nonlinearities in solids and gases. These intensities are several orders of magnitude higher than in previous studies yet still remain below the ionization threshold of the materials under investigation. The importance of this work is underscored by the fact that there is a lack of literature data for the nonlinearities of both gases and solids in the LWIR region, particularly for field strengths larger than 1 MW/cm^2. The structure of the dissertation is as follows: Chapter 2 presents an introduction to the theory of nonlinear optics and a summary of important nonlinear optical phenomena that occur in both semiconductors and gases. Chapter 2 also includes a description of the model used to numerically simulate the propagation of mid-IR light in nonlinear optical media along with a couple of instructive, sample simulations using this model. Chapter 3 describes the high-repetition rate, picosecond, CO_2 master-oscillator power-amplifier (MOPA) laser system at UCLA that enabled the experiments presented in this thesis. Chapter 4 describes experiments dedicated to the measurement of the third-order nonlinearity of gases by four-wave mixing while Chapter 5 and 6 details experiments on supercontinuum generation and nonlinear pulse compression of intense 10 μm light in GaAs, respectively.

References

[1] P.A. Franken, A.E. Hill, C.W. Peters, and G. Weinreich. "Generation of Optical Harmonics." Physical Review Letters, **7**, 4 (1961)

[2] R.R. Alfano and S.L. Shapiro. "Observation of self-phase modulation and small-scale filaments in crystals and glasses". Physical Review Letters, **24**, 11 (1970)

[3] R.R. Alfano, *The Supercontinuum Laser Source*. Springer, New York (2006)

[4] D. Grischkowsky and A.C. Balant. "Optical pulse compression based on enhanced frequency chirping". Applied Physics Letters, **41**, 1 (1982).

[5] C.V. Shank, R.L. Fork, R. Yen, R.H. Stolen, "Compression of femtosecond optical pulses", Applied Physics Letters, **40**, 761 (1982).

[6] Anne L'Huillier and Ph. Balcou, "High-order harmonic generation in rare gases with a 1-ps 1053-nm laser". Physical Review Letters, **70**, 774 (1993).

[7] J.J. Macklin, J.D. Kmetec and C. L. Gordon III, Physical Review Letters, **70**, 766 (1993)

[8] R. L. Aggarwal and B. Lax, "Noncollinear phase matching in GaAs," Applied Physics Letters, **22**, 329-330 (1973).

[9] W. Shi, Y. J. Ding, N. Fernelius and K. Vodopyanov, "Efficient, tunable, and coherent 0.18 – 5.27-THz source based on GaSe crystal," Optics Letters, **27**, 1452-1456 (2002).

[10] H. P. Weber, "Method for Pulsewidth Measurement of Ultrashort Light Pulses Generated by Phase-Locked Lasers using Nonlinear Optics," Journal of Applied Physics, **38**, 5, (1967).

[11] D. J. Kane and R. Trebino, "Characterization of Arbitrary Femtosecond Pulses Using Frequency-Resolved Optical Gating," IEEE Journal of Quantum Electronics, **29**, 2, (1993)

[12] Tenio Popmintchev, Ming-Chang Chen, Dimitar Popmintchev, Paul Arpin, Susannah Brown, Skirmantas Ališauskas, Giedrius Andriukaitis, Tadas Balčiunas, Oliver D. Mücke, Audrius Pugzlys, Andrius Baltuška, Bonggu Shim, Samuel E. Schrauth, Alexander Gaeta, Carlos Hernández-García, Luis Plaja, Andreas Becker, Agnieszka Jaron-Becker, Margaret M. Murnane, Henry C. Kapteyn, "Bright Coherent Ultrahigh Harmonics in the keV X-ray Regime from Mid-Infrared Femtosecond Lasers", Science, **336**, 1287-1291 (2012)

[13] S. Ghimire, A. D. DiChiara, E. Sistrunk, P. Agostini, L. F. DiMauro, and D. A. Reis, "Observation of high-order harmonic generation in a bulk crystal", Nature Physics, **7**, 138-141, (2011).

Chapter 2

Introduction to Nonlinear Optics

Section 2.1 The nonlinear polarizability

This thesis is concerned with nonlinear optical phenomena in gases and semiconductors driven by gigawatt power, 10 μm laser pulses having a temporal pulse length of 200 and 3 ps. As such, the optical phenomena of four-wave mixing, self-phase modulation, dispersion, pulse compression, harmonic generation, Raman scattering related to optical phonons in solids and rotational-vibration motion in molecular gases, and self-focusing will be important. This chapter is dedicated to reviewing these phenomena in some detail. Although much of the material presented in this chapter is tutorial, the language and definitions introduced here are important to communicate the novel nonlinear optical effects covered in this dissertation. For example, the material presented in Appendix D, describing the contribution of cascaded difference frequency mixing to the effective third-order susceptibility of semiconductors, would not be understandable if not for the content of this chapter.

Nonlinear optical effects are commonly modeled by a perturbative expansion of the macroscopic polarizability. In the frequency domain this can be written as:

$$\vec{P}(\vec{r}, \omega) = \epsilon_0\left(\chi^{(1)} \cdot \vec{E} + \chi^{(2)} \cdot \vec{E}\vec{E} + \chi^{(3)} \cdot \vec{E}\vec{E}\vec{E} + \cdots\right) \tag{2.1}$$

Where ϵ_0 is the permittivity of free space, $\vec{E}$ is the electric field, and $\chi^{(n)}$ is the nth order susceptibility. In the most general case, these susceptibilities are complex valued tensors of order n. All materials have odd order susceptibilities but even order susceptibilities vanish in centro-symmetric media such as gases and glass [1]. Since each term in Eq. 2.1 is much smaller than the

one that precedes it, the quadratic and cubic terms are the most important. The electric field can be expressed as:

$$\vec{E}(\vec{r}, t) = \frac{1}{2}\left(\mathcal{E}e^{i\omega_0 t - i\vec{k}\cdot\vec{r}} + c.c.\right)\hat{e}. \tag{2.2}$$

Where $\vec{k}$ is the wave number and ω_0 is the carrier frequency of the laser. The complex envelope is denoted by $\mathcal{E}$ and $\hat{e}$ represents a unit vector that points in the direction of the electric field. Note that a spatio-temporal envelope could be included within the complex envelope $\mathcal{E}$. In the simple case described by Eq. 2.2, substitution of the electric field into Eq. 2.1 shows that the nonlinear polarizability oscillates at $2\omega_0$ and $3\omega_0$ from the second and third order term, respectively. In a more complicated situation, such as a dual-frequency electric field $\vec{E}(\vec{r}, t) = \frac{1}{2}\left(\mathcal{E}_1 e^{i\omega_1 t - i\vec{k_1}\cdot\vec{r}} + \mathcal{E}_2 e^{i\omega_2 t - i\vec{k_2}\cdot\vec{r}} + c.c.\right)\hat{e}$, the nonlinear polarizability oscillates at all of the possible sum and difference frequencies. This nonlinear polarizability gives rise to new frequencies of light as it acts as a source term in the nonlinear wave equation [2]:

$$\nabla\times\nabla\times\vec{E}(\vec{r}, \omega_q) - \omega_q\mu_0\bar{\epsilon}(\vec{k}, \omega_q)\cdot\vec{E}(\vec{r}, \omega_q) = \omega_q^2\mu_0\vec{P}_{NL}(\vec{r}, \omega_q). \tag{2.3}$$

Where $\bar{\epsilon}$ is the dielectric tensor of the medium and the index q denotes a specific frequency contained within the nonlinear polarizability. The term P_{NL} is the nonlinear polarizability that is defined as:

$$\vec{P}_{NL} = \epsilon_0(\chi^{(2)}\cdot\vec{E}\vec{E} + \chi^{(3)}\cdot\vec{E}\vec{E}\vec{E} + \cdots). \tag{2.4}$$

To understand the physics of nonlinear frequency conversion it is useful to simplify Eq. 2.3 under the conditions that the medium is isotropic, the slowly varying envelope approximation is valid and that the field only changes in the propagation direction, z. Under these three conditions

an ordinary differential equation for the evolution of the complex amplitude as a function of propagation distance can be derived [2]:

$$\frac{d}{dz}\mathcal{E}(z,\omega_q) \approx \frac{-i\omega_q^2\mu_0}{2k_q}P_{NL}(z,\omega_q)e^{-i\omega_q t+ik(\omega_q)z} \tag{2.5}$$

Through examination of Eq. 2.5, it is clear that any electromagnetic wave may be generated in a nonlinear medium so long as the frequency of the electromagnetic wave is present in the nonlinear polarizability. In practical situations, however, it is only those electromagnetic waves having frequencies and wave-numbers constants that satisfy the phase-matching conditions that are efficiently amplified. These conditions will be introduced and explained in the next section.

Section 2.2: Three-wave mixing and phase matching

To understand the basic physics of nonlinear optical mixing it is instructive to consider the simplest case of three-wave mixing — second harmonic generation ($2\omega = \omega + \omega$). It is customary in nonlinear optics to write the photon mixing equation into the argument of the susceptibility, for the case of second harmonic generation the nonlinear polarization takes the form:

$$P_{NL}(z) = \frac{\epsilon_0}{4}\chi^{(2)}(2\omega = \omega + \omega)\mathcal{E}(\omega)\mathcal{E}(\omega)e^{2i(\omega t-k(\omega)z)}. \tag{2.6}$$

Here we have neglected the tensor nature of the susceptibility to simplify this introduction. Substitution of Eq. 2.6 into Eq. 2.5 yields:

$$\frac{d}{dz}\mathcal{E}(z,2\omega) \approx -\frac{i\omega^2\mu_0}{2k(2\omega)}\epsilon_0\chi^{(2)}(2\omega = \omega + \omega)\mathcal{E}(\omega)\mathcal{E}(\omega)e^{-i\Delta kz}. \tag{2.7}$$

Here Δk is the phase mismatch between the fundamental field and the second harmonic, defined as:

$$\Delta k = 2k(\omega) - k(2\omega). \tag{2.8}$$

In the limit of weak depletion, Eq. 2.7 can be integrated to obtain the evolution of the amplitude of the second harmonic field as a function of propagation distance:

$$\mathcal{E}(z, 2\omega) = \frac{\omega^2 \mu_0}{2k(2\omega)} \epsilon_0 \chi^{(2)} \mathcal{E}^2(\omega) \left(\frac{e^{-i\Delta k z} - 1}{\Delta k} \right) \tag{2.9}$$

Here we have dropped the photon mixing arguments in the susceptibility to simplify the notation. Equation 2.9 can be rearranged using trigonometric identities and expressed in terms of intensity by using the relationship $I(\omega) = \frac{c\epsilon_0 n(\omega)}{2} \mathcal{E}(\omega)\mathcal{E}^*(\omega)$ as:

$$I(z, 2\omega) = \frac{\omega^2 \chi^{(2)^2}}{4c^3 \epsilon_0 n^2(\omega) n(2\omega)} I^2(\omega) z^2 \frac{\sin^2 \frac{\Delta k z}{2}}{\left(\frac{\Delta k z}{2} \right)^2} \tag{2.10}$$

Where $n(\omega)$ is the refractive index at frequency ω. The above equation shows that, if the phase-mismatch is finite, the amplitude of the second harmonic field will undergo cycles of conversion and back conversion. In this case, it is useful to define the coherence length as the length in which the second harmonic conversion is at a maximum:

$$l_{coh} = \frac{\pi}{\Delta k} \tag{2.11}$$

Note that the coherence length corresponds to a phase shift of π radians. In practice, phase matching is typically accomplished by the use of birefringent crystals where the second harmonic is polarized orthogonal to the fundamental field. The above analysis can be generally applied for any three-wave mixing process such as difference frequency generation (DFG), sum frequency generation (SFG) and optical parametric amplification (OPA).

Section 2.3: Four-wave mixing

The simplest third-order nonlinear optical effect is four-wave mixing (FWM). In the degenerate

case, two pump photons with frequency with frequency ω_1 annihilate to form sidebands with the

photon conservation of energy argument $\omega_2 + \omega_3 = \omega_1 + \omega_1$, as can be inferred from the

spectrum in Fig. 2.1a. Commonly, two pump waves are used to generate sidebands with a

known frequency separation. This case of nondegenerate FWM is shown schematically in Fig.

2.1b for which the photon conservation of energy argument is $\omega_3 + \omega_4 = \omega_1 + \omega_2$. This can be

rearranged using $\Delta\omega = \omega_2 - \omega_1$ to obtain expressions for the sideband frequencies, $\omega_3 = 2\omega_1 -$

ω_2 and $\omega_4 = 2\omega_2 - \omega_1$. The nonlinear polarizability for the low frequency sideband is:

$$P_{NL}(z,\omega_3) = \frac{3}{4}\epsilon_0 \chi^{(3)}(\omega_3 = 2\omega_1 - \omega_2)\mathcal{E}^2(\omega_1)\mathcal{E}^*(\omega_2)e^{i(\omega_3 t - (2k(\omega_1) - k(\omega_2))z)}. \tag{2.12}$$

Substitution of the above into Eq. 2.5 yields the amplitude equation for the sideband at angular

frequency ω_3:

$$\frac{d}{dz}\mathcal{E}(z,\omega_3) \approx -\frac{i\omega_3^2 \mu_0}{2k(\omega_3)}\epsilon_0 \frac{3}{4}\chi^{(3)}\mathcal{E}^2(\omega_1)\mathcal{E}^*(\omega_2)e^{-i\Delta kz}. \tag{2.13}$$

Here we have once again removed the photon mixing argument from the susceptibility for

simplicity. The phase-mismatch for FWM is defined as $\Delta k = 2k(\omega_1) - k(\omega_2) - k(\omega_3)$. In the

absence of pump depletion we can integrate Eq. 2.13 with respect to z to derive the a formula for

the evolution of the intensity of the low-frequency sideband as a function of propagation

distance:

$$I(z,\omega_3) = \frac{1}{4}\left(\frac{\frac{3}{4}\chi^{(3)}\omega_3}{\epsilon_0 c^2 n(\omega_1)\sqrt{n(\omega_2)n(\omega_3)}}\right)^2 I^2(\omega_1)I(\omega_2)z^2 \frac{\sin^2\frac{\Delta kz}{2}}{\left(\frac{\Delta kz}{2}\right)^2} \tag{2.14}$$

As was the case with three-wave mixing, the sideband will undergo cycles of conversion and back-conversion if the phase-mismatch is finite. The coherence length for FWM is also defined as $l_{Coh} = \frac{\pi}{\Delta k}$.

(a)

ω_1

ω_2 ω_3

Spectral Energy Density

Frequency

$\omega_2 + \omega_3 = \omega_1 + \omega_1$

(b)

ω_1 ω_2

ω_3 ω_4

Spectral Energy Density

Frequency

$\omega_3 + \omega_4 = \omega_1 + \omega_2$
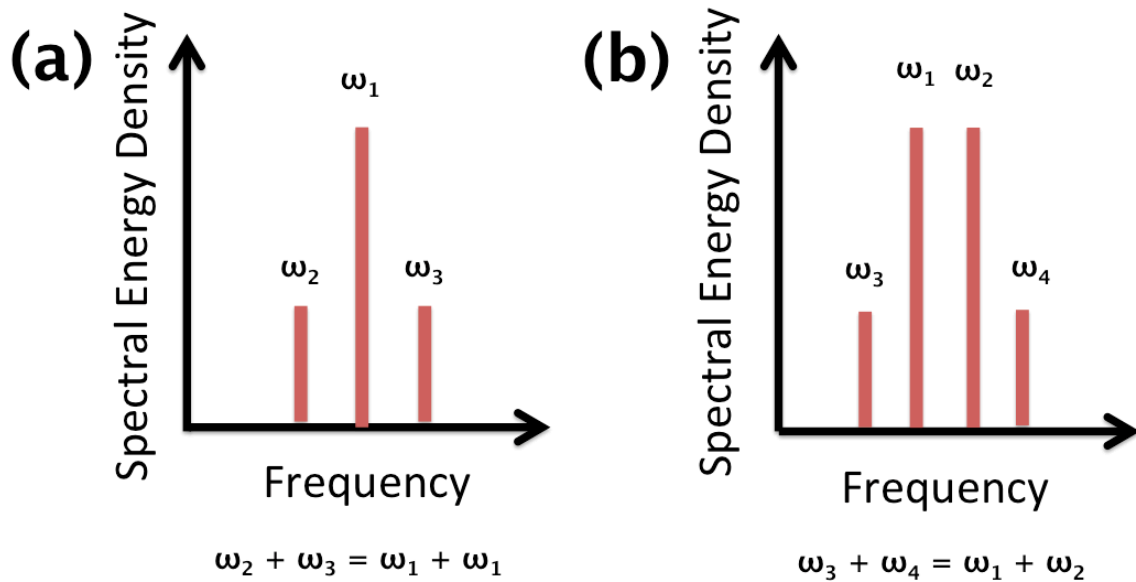
Figure 2.1: Diagram depicting the spectrum for (a) degenerate and (b) non-degenerate FWM mixing. Photon mixing arguments are presented below each spectrum.

Section 2.4: Self-phase modulation and the nonlinear refractive index

One of the most ubiquitous and important phenomena in the field of nonlinear optics is self-phase modulation (SPM). The physics of SPM can be looked at as a special case of FWM in which all four waves are the same frequency. The nonlinear polarizability leading to SPM can be written as:

$$P_{NL} = \frac{3}{4}\epsilon_0\chi^{(3)}(\omega = \omega - \omega + \omega)\mathcal{E}(\omega)\mathcal{E}^*(\omega)\mathcal{E}(\omega)\exp(i\omega t - ik(\omega)z) \tag{2.15}$$

Substitution of the above into Eq. 2.5 yields an expression for the derivative of the complex amplitude with respect to propagation distance:

$$\frac{d}{dz}\mathcal{E}(\omega) = -\frac{i\omega^2}{k(\omega)c^2}\left(\frac{3}{4}\chi^{(3)}\mathcal{E}(\omega)\mathcal{E}^*(\omega)\mathcal{E}(\omega)\right) \tag{2.16}$$

In this case, FWM is naturally phase-matched and the usual exponential factor (*e.g.*, Eq. 2.13) becomes unity. Equation 2.16 can be re-written using the definition of intensity as:

$$\frac{d}{dz}\mathcal{E}(z,\omega) = -\frac{i\omega}{c}\left(\frac{\frac{3}{4}\chi^{(3)}}{n^2(\omega)c\epsilon_0}I(\omega)\mathcal{E}(z,\omega)\right) \tag{2.17}$$

As can be inferred from the above, the result of this implicit phase-matching is that only the phase of the field is effected by the nonlinear response. In this case, the term $\dfrac{\frac{3}{4}\chi^{(3)}}{n^2(\omega)c\epsilon_0}I(\omega)$ acts like a change to the linear index of refraction. The total index of refraction can then be written as:

$$n = n_0 + n_2 I(t) \tag{2.18}$$

Where n_0 is the linear refractive index and I is the intensity of the light. The parameter n_2 is referred to as the nonlinear refractive index or the Kerr coefficient and is of utmost importance for describing nonlinear optical interactions. The nonlinear index is defined as:

$$n_2 = \frac{\frac{3}{4}\chi^{(3)}}{n^2(\omega)c\epsilon_0} \tag{2.19}$$
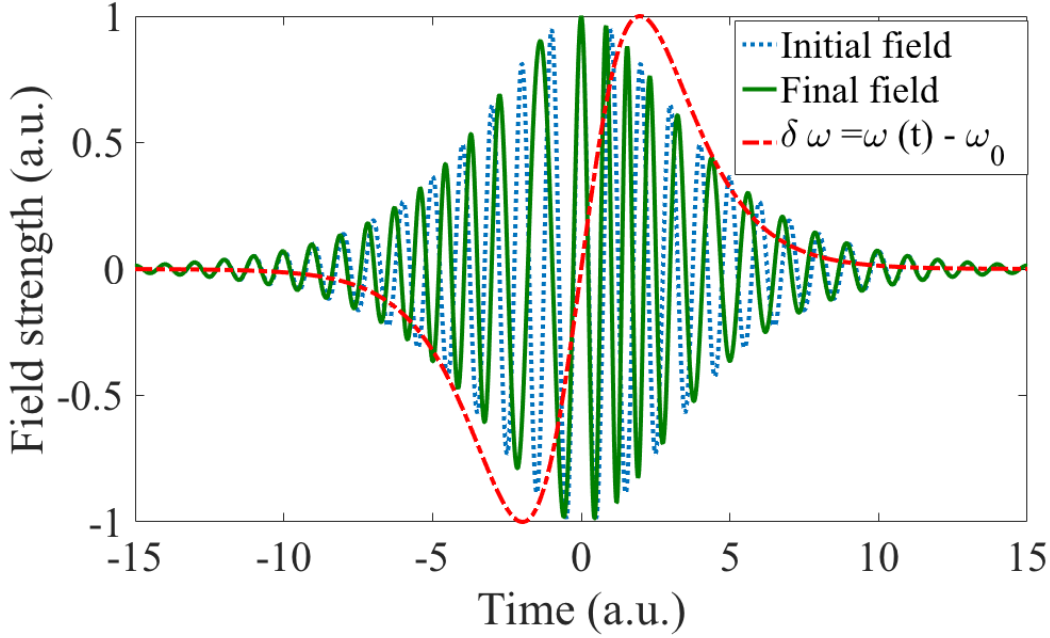
Figure 2.2: A plot of the electric field of an optical pulse before (blue) and after (green) is has been altered by SPM. Plotted in red is the pulse's instantaneous frequency.

Self-phase modulation is a special case of FWM that results in time- and intensity-dependent phase changes. For a laser pulse with finite time duration, these nonlinear phase changes can lead to the generation of new frequencies in the vicinity of the laser pulse's carrier frequency. To investigate changes to the instantaneous frequency we take the time derivative of the phase argument:

$$\omega_i(t) = \frac{\partial}{\partial t}\left(\omega_0 t - \left(n_0 + n_2 I(t)\right)k_0 z\right) = \omega_0 - n_2 k_0 z \frac{\partial}{\partial t} I(t) \qquad (2.20)$$

Where $\omega_i(t)$ is the instantaneous frequency of the laser pulse. As can be seen above, the spectrum of the pulse becomes red-shifted and blue-shifted during the rising and falling edge of the laser pulse, respectively. To visualize this process, Fig. 2.2 is a plot of the electric field from a laser pulse before and after it has undergone self-phase modulation. Plotted with the electric

13

field is a plot of the frequency shift across the pulse. It should be noted that SPM causes an increase of bandwidth but does not change the temporal pulse duration. Instead, the time-bandwidth product of the pulse is increased as it develops a positive chirp, as can be seen in Fig. 2.2. With additional dispersion, however, the bandwidth gained by SPM can be used to compress the pulse to a shorter temporal pulse length.

A physical interpretation of SPM can be gained by imagining the energy flow between the laser field and the medium. During the rising edge of the laser pulse, energy moves from the laser field to the medium's polarizability thus red-shifting these photons. During the falling edge of the pulse this same energy is being transferred back from the medium's polarizability to the laser field, as a result these photons become blue-shifted.

There is an important length scale associated with self-phase modulation. The nonlinear length is defined as:

$$L_{NL} = \frac{1}{n_2 I k_0}$$

(2.21)

Where k_0 is the vacuum wave-number. Considering that the nonlinear phase shift accumulated from SPM after a length L is $\phi_{NL} = k_0 n_2 I L = \frac{L}{L_{NL}}$, the nonlinear length has a nice physical interpretation. After traversing one nonlinear length, the laser pulse gains one radian of nonlinear phase. Under the assumption that the laser pulse is Gaussian in time, it is possible to calculate the maximum frequency shift generated via SPM.   Assuming that the intensity is of the form $I(t) = I_0 \exp{-t^2/\tau^2}$ then the nonlinear frequency shift after a length L is:

$$\delta\omega = \frac{\partial}{\partial t}\phi_{NL} = -\frac{2t}{\tau^2}\frac{L}{L_{NL}} .$$

(2.21)

An expression for the maximum frequency shift can be obtained by setting the derivative of equation 2.21 equal to zero. For a Gaussian, transform-limited pulse the maximum frequency shift is:

$$\delta\omega_{max} \approx \Delta\omega_0 \frac{L}{L_{NL}}$$

(2.22)

Where $\Delta\omega_0$ is the initial bandwidth of the laser pulse. Equation 2.22 allows one to conveniently estimate the amount of broadening achieved via SPM. For example, a Gaussian pulse will be spectrally broadened by a factor of three after traversing three nonlinear lengths and accumulating three radians of nonlinear phase.

Let us calculate the nonlinear length for the 10 μm, $1 - 10$ GW/cm^2 laser pulses used for experiments described in this thesis. For semiconductors such as GaAs the nonlinear index is approximately 10^{-13} cm^2/W and the nonlinear length is $1 - 10$ mm. For gases such as the air the nonlinear index is approximately 10^{-19} cm^2/W corresponding to a nonlinear length of $1 - 10$ km. Finally, it should be mentioned that an additional laser beam could be subjected to nonlinear phase changes generated from an intense laser pulse. In this process of cross-phase modulation (XPM) the nonlinear phase shift imparted to the probe is twice that imparted to the pump. This can be seen by the substitution of a dual-frequency electric field into the nonlinear polarizability (Eq. 2.4)

Section 2.5 Self-focusing and laser filamentation

There is a spatial analogue to SPM known as self-focusing. Since the total index of refraction varies according to $n = n_0 + n_2 I$, a laser beam that has a Gaussian distribution of intensity in space, I(r), will produce a refractive index perturbation that is shaped like a positive lens. This

lens will cause a focusing of the laser beam so long as the strength of the lens can overcome the natural diffraction of the laser beam. The threshold power at which the nonlinear lens balances diffraction is called the critical power of self-focusing and is calculated as [3]:

$$P_{crit} = \frac{3.77\pi n_0}{2k_0^2 n_2}. \tag{2.23}$$

Equation 2.23 is derived assuming a balance between the nonlinear length, $L_{NL} = (n_2 k_0 I)^{-1}$, and the diffractive or Rayleigh length $z_R = \frac{n_0 \pi w_0^2}{\lambda}$, where w_0 is the beam radius. This is why, for example, the threshold for self-focusing is based on the laser pulse's power and not its intensity because both the nonlinear and diffractive lengths scale in direct proportion to the area of the beam. Another interesting aspect of Eq. 2.23 is that the critical power scales quadratically with laser wavelength. This arises because the nonlinear length is inversely proportional to the laser wavelength while the diffractive length is in direct proportion to wavelength.

For the 10 μm laser pulses considered in this thesis, the critical power for self-focusing in semiconductors is approximately 5 MW. Gases such as air, however, have a nonlinear index close to 10^{-19} cm²/W that corresponds to a critical power of 1 TW.

If a laser pulse's power is above the threshold defined by Eq. 2.23 then the beam will focus at a finite distance within a nonlinear medium. For a plane wave this distance can be estimated using [4]:

$$z_{SF} = \frac{n_0 k_0 w_0^2 / \sqrt{2}}{\sqrt{\frac{P}{P_{crit}} - 1}}. \tag{2.24}$$

Where w_0 is the FWHM beam radius and P is the power of the laser pulse. As can be inferred from the above, if the laser's power is exactly the critical power then the self-focusing distance is

infinite. When the laser's power is many times the critical power then the beam tends to break up into a family of beamlets, each containing a critical power for self-focusing [4].

Finally, it should be noted that the self-focusing of a high-power beam is eventually arrested by another nonlinear process. In most cases this arresting mechanism is the negative change to the refractive index that occurs because of photo-ionization or nonlinear loss [5, 6]. The change of the refractive index from plasma can be estimated from the dispersion relation for an electromagnetic wave in a plasma [7]:

$$\Delta n \approx -\frac{1}{2}\frac{N}{N_c}. \tag{2.25}$$

Where N is the density of the plasma and N_c is the critical plasma density defined by $N_c = \frac{\omega_0^2 m \epsilon_0}{e^2}$, where m and e are the mass and charge of the electron, respectively. It is possible for nonlinear self-focusing to be dynamically balanced by plasma-induced defocusing to produce a long channel of guided laser light in a regime known as laser filamentation [5].

Section 2.6: Dispersion and soliton formation

Aside from the nonlinear response itself, dispersion is the single most important phenomenon in all of nonlinear optics. The material's dispersion is of paramount importance because it governs phase-matching and determines the relative velocity between the spectral components in a pulse of light. To understand the important aspects of a material's dispersion it is useful to express wave-number $k(\omega) = \frac{n(\omega)\omega}{c}$, as a Taylor series expansion:

$$k(\omega) = k_0 + k_1(\omega - \omega_0) + \frac{1}{2}k_2(\omega - \omega_0)^2 + \cdots \tag{2.26}$$

Where $k_n = \frac{\partial^n k(\omega)}{\partial \omega^n}$ and ω_0 is the central frequency of the laser pulse. The reciprocal of k_1 is the group velocity given by:

$$\frac{\partial k}{\partial \omega} = v_g^{-1} = \frac{1}{c}\left(n(\omega) + \omega \frac{\partial}{\partial \omega} n(\omega)\right). \tag{2.27}$$

Where v_g is the group velocity that determines the speed at which the laser pulse propagates through a medium. The term in parenthesis is sometimes referred to as the group index $n_g(\omega) = n(\omega) + \omega \frac{\partial n(\omega)}{\partial \omega}$. The second term in Eq. 2.26, k_2, is responsible for group velocity dispersion (GVD):

$$\frac{\partial^2 k}{\partial \omega^2} = \frac{1}{c}\left(2\frac{\partial}{\partial \omega} n(\omega) + \omega \frac{\partial^2}{\partial \omega^2} n(\omega)\right). \tag{2.28}$$

The GVD term determines the relative velocity between different frequency components in a laser pulse and can be used to calculate the amount of temporal pulse broadening per unit length that can be expected when a short pulse traverses a transparent dielectric. The GVD coefficient can be positive or negative, determined by the concavity of the dispersion relation. A positive GVD term implies that red colors travel faster than blue colors and the opposite is true for a negative term. The dispersive length is a length scale upon which temporal pulse broadening occurs [8]:

$$L_D = \frac{\tau_0^2}{|k_2|} \tag{2.29}$$

Where τ_0 is the transform-limited pulse length. The temporal pulse broadening described above follows a law analogous to the evolution of the radius of a Gaussian beam:

$$\tau^2(z) = \tau_0^2 \left(1 + \frac{z^2}{L_D^2}\right) \qquad (2.30)$$

For the picosecond, 10 μm pulses considered in this thesis, the dispersion length is meter-scale in GaAs having a GVD coefficient of ~ -1350 fs^2/mm. For 10 μm pulses far away from the ultraviolet resonances common atomic and molecular gases, the dispersive length is practically infinite.

Similar to SPM, the material's GVD acts to create a frequency chirp across the laser pulse's temporal pulse profile. If the material has negative GVD, however, this chirp can act to compensate the chirp created by the nonlinear response. Further, if the effect of negative GVD perfectly balances with the effect of SPM a soliton, a pulse that propagates in a nonlinear medium without changing shape, can be formed [8]. In most cases the chirp created by the nonlinearity is stronger than that created by GVD and the pulse will self-compress as it propagates in a nonlinear medium. The ratio of the dispersive and nonlinear length, $N^2 = L_D/L_{NL}$, is a useful parameter to categorize such nonlinear optical interactions. Here N is the so-called soliton order for which N =1 implies solitonic propagation and N > 1 implies that the laser pulse is in a self-compression regime.

In the self-compression regime, nonlinear pulse compression acts to increase the laser pulse's intensity that, in turn, enhances the effect of SPM. This process may eventually lead to a modulational instability and the generation of supercontinuum or white-light. Indeed, the majority of supercontinuum sources involve propagation in the negative GVD region of a nonlinear material for this reason. Finally, it should be noted that almost every dielectric that is transparent in the mid-IR exhibits negative GVD with the notable exceptions of germanium and tellurium. In the final section of this chapter we will present numerical simulations depicting the

propagation of intense 10 μm light in both germanium and gallium arsenide to show the differences in the nonlinear propagation of such pulses in materials exhibiting positive and negative GVD.

Section 2.7: Stimulated Raman Scattering

Spontaneous Raman scattering refers to a physical process by which a photon is frequency downshifted via the excitation of a low frequency, optical phonon in a material. In a solid this mode is related to the phonon band and in molecular gases this mode is related to rotational-vibrational transitions.

This process can be explained quantum mechanically as follows: a photon at frequency ω_0 is incident upon a two-level system where the energy difference between the two states is $\Delta E = \hbar \Omega_R$, where Ω_R is the Raman frequency and $\hbar$ is Planck's constant divided by 2π. The incident field causes excitation to a virtual level that exists $\hbar \omega_0$ energy units above the initial state. If the system is initially in the lower level, then it may decay to the first excited state generating a photon at frequency $\omega_S = \omega_0 - \Omega_R$ as can be seen in the energy level diagram of Fig. 2.3. If, instead, the system is initially in the first excited state then the system may relax to the ground level thus emitting a new photon at frequency $\omega_{AS} = \omega_0 + \Omega_R$. The lower frequency photon at ω_S is referred to as the Stokes frequency while the higher frequency photon at ω_{AS} is referred to as the anti-Stokes frequency. It should be mentioned that the anti-Stokes component is typically much weaker than the Stokes component since, at thermal equilibrium, the population in the higher state is smaller than that of the lower state by a factor of $\exp\left(-\hbar \frac{\Omega_R}{k_B T}\right)$, where k_B is the Boltzmann constant and T is the temperature.
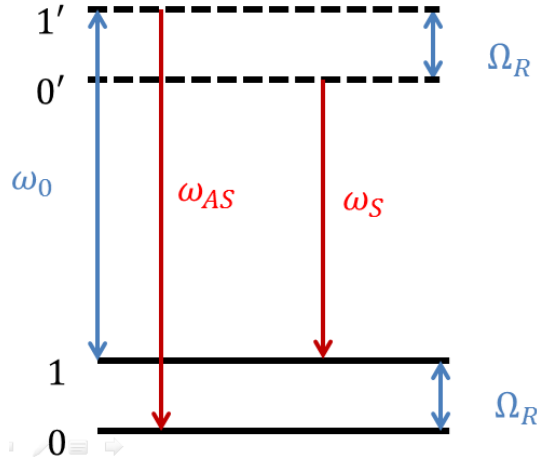
Figure 2.3: Energy level diagram of a two-level system depicting Raman scattering of an incident laser field at frequency ω_0. The Raman frequency is denoted by Ω_R.

In the case of stimulated Raman scattering, the Stokes field generated through spontaneous Raman scattering can beat with the fundamental field generating an intensity modulation at $\omega_0 - \omega_S = \Omega_R$. This intensity modulation can reinforce the Raman process leading to an instability and exponential gain for the Stokes light. Spontaneous Raman scattering is a rather weak process that scatters light in every direction but stimulated Raman scattering (SRS) can convert a large percentage of the incident light, collimated in the forward or backward direction.

There are a variety of methods to model the SRS process. For the work in this dissertation SRS will be treated phenomenologically as a delayed part of the third-order nonlinearity [8]. Since the Raman response time can be comparable to the temporal pulse length of the driving field the nonlinear polarization should be expressed in the time domain:

$$P_{NL}(r,t) = \epsilon_0 \chi^{(3)} E(r,t) \int_{-\infty}^{t} R(t-t_1) |E(r,t_1)|^2 dt_1 . \tag{2.31}$$

Where $R(t - t_1)$ is a function that characterizes the third-order nonlinear response and t_1 is an integration variable. For a third-order nonlinearity consisting of an instantaneous, electronic response and a delayed, Raman response $R(t)$ takes the form:

$$R(t) = (1 - f_R)\delta(t) + f_R h_R(t). \tag{2.32}$$

Where f_R is the fraction of the nonlinear response dedicated to the Raman effect, $\delta(t)$ is a Dirac-Delta function and $h_R(t)$ is the Raman response function. The Raman gain is related to this Raman response function by:

$$g_R(\omega - \omega_0) = \frac{\omega_0}{cn(\omega_0)} f_R \chi^{(3)} Im[\tilde{h}(\omega - \omega_0)] \tag{2.33}$$

where $\tilde{h}(\omega - \omega_0)$ is the Fourier transform of the Raman response function, $h(t)$ [8].

For most crystals, such as the semiconductors studied in this thesis, the Raman response function can be modeled as an exponentially decaying sinusoid of the form [8]:

$$h_R(t) = \frac{\tau_1^2 + \tau_2^2}{\tau_1 \tau_2^2} \exp\left(-\frac{t}{\tau_2}\right) \sin\left(\frac{t}{\tau_1}\right). \tag{2.34}$$

Where $\tau_{1,2}$ are time constants used to match the Raman gain spectrum of the medium in question. Figure 2.4a is a plot of Eq. 2.34 for GaAs where $\tau_1 = 18.6\ fs$ and $\tau_2 = 3\ ps$, were chosen in order to measure the GaAs Raman fluorescence measurements in [9]. Figure 2.4b is a plot of the real and imaginary part of the Fourier transform of the Raman response function showing gain at the Stokes frequency and loss at the anti-Stokes frequency.
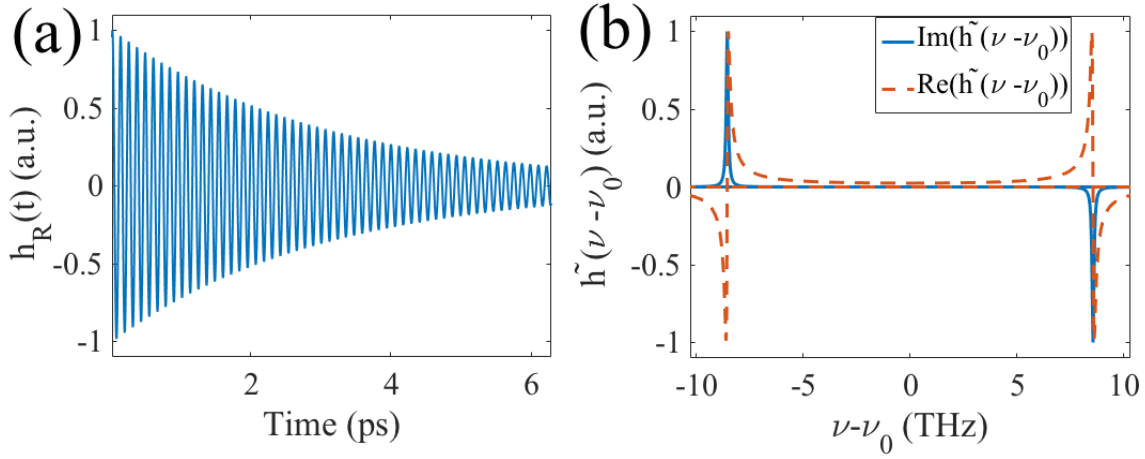
Figure 2.4: A calculated Raman response for GaAs both in the (a) time domain and (b) frequency domain.

For molecular gases such as N_2 and O_2 that will be studied in this thesis, a family of rotational-vibrational resonances complicates the Raman response function [10, 11]. For a mixture of molecular gases, such as the air, the Raman response takes the form:

$$h(t) = \Sigma_i \, h_{ri} + h_{vi}. \tag{2.35}$$

Where h_r is the part of the response from rotations and h_v is responsible for the vibrational response. The index i is summed over the gas species under investigation, in the following $i = 1$ corresponds to nitrogen and $i = 2$ corresponds to oxygen. The rotational response is calculated as [11]:

$$h_r(t) = h_{r1}(t) + h_{r2}(t) = \Sigma_J F_{1J} \sin\left(-\omega_{1J}t\right) + F_{2J} \sin\left(-\omega_{2J}t\right) \tag{2.36}$$

Where J is the rotational quantum number and $\omega_{1,2J} = 4\pi B_{1,2}c(2J + 3)$ where $B_{1,2}$ are the rotational constants, $B_1 \approx 1.99 \, cm^{-1}$ and $B_2 \approx 1.44 \, cm^{-1}$ [11]. Finally, in the above:

23

$$F_{1,2J} = \frac{(\rho_{1,2J+1} - \rho_{1,2J})Z_{1,2J}(J+2)(J+1)}{2J+3} \tag{2.37}$$

Where $Z_{1J} = 1$ and 2 for odd and even J, respectively and $Z_{2J} = 1$ and 0 for odd and even J,

respectively. Finally, ρ is the population in the state defined by the rotational quantum number

that for a Boltzmann distribution is given by:

$$\rho_{1,2J} = \exp\left[-ch\frac{B_{1,2}J(J+1)}{k_BT}\right] \times \left\{\Sigma_J Z_{1,2J}(2J+1)\exp\left[-ch\frac{B_{1,2}J(J+1)}{k_BT}\right]\right\}^{-1}. \tag{2.38}$$

For the picosecond pulse lengths considered in this thesis, the rotational part of the Raman

response dominates over the vibrational part. As a result, the vibrational part will be neglected

for this discussion. Figure 2.5 depicts the rotational Raman response for atmospheric air,

separated for N_2 and O_2 gas. Figure 2.5a shows the time domain representation of this response

function, showing the so-called echo recurrences of rotational wave-packets [12]. The frequency

domain description in Fig. 2.5b shows a family of rotational resonances on either side of the

carrier frequency. As was the case with GaAs, there is gain for the Stokes component and loss

for the anti-Stokes component. Note that only the imaginary part of the response was plotted in

Fig. 2.5b to simplify the figure.
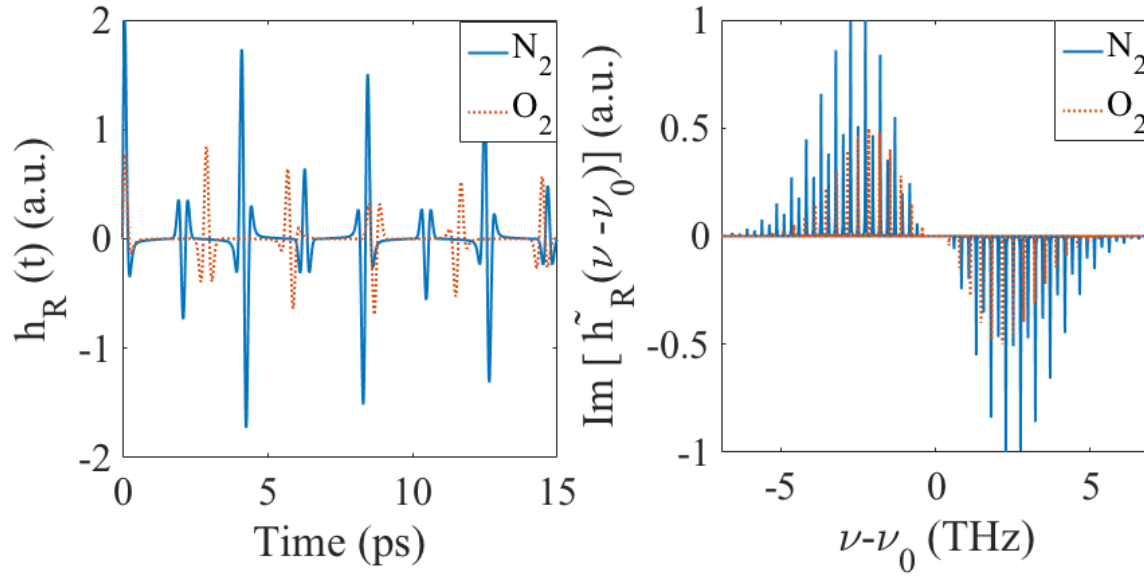
Figure 2.5: A calculated rotational Raman response for atmospheric air, separated into conrtributions from N_2 and O_2 both in the (a) time domain and (b) frequency domain.

Raman scattering in both solids and gases can affect the nonlinear optics of an interaction in different ways depending on how the laser's spectrum overlaps with the Raman gain spectrum (RGS). In the case that the laser's spectrum does not overlap with the RGS, one may observe the growth of distinct Stokes and anti-Stokes components located at $\omega_0 \pm \Omega_R$. If the initial laser spectrum overlaps with the RGS, however, one may observe so-called "intra-pulse" Raman scattering, where the entire spectrum of the laser pulse will shift towards the red with increasing nonlinear phase shift. For the picosecond, 10 μm laser pulses considered in this thesis, the bandwidth is approximately 1 THz. These parameters lead to a regime of classical Raman scattering for the case of GaAs (see Fig. 2.4b) and to the intrapulse Raman Scattering regime for the case of air (see Fig. 2.5b).

Stimulated scattering in molecular gases is even more complicated, however, due to the fact that this scattering has a vibrational and rotational part. The selection rules for Raman scattering

in diatomic molecules is $\Delta J = 0, \pm 2$ [12]. Here $\Delta J = 0$ is often referred to as Rayleigh

scattering and $\Delta J = \pm 2$ is referred to as rotational Raman scattering. Stimulated scattering in

such systems can manifest as an enhancement to the Kerr index creating an effective nonlinear

index:

$$n_{2,eff} = n_2 + n_{2,Molecular}.$$
(2.39)

For narrowband excitation ($\sim$ nanosecond pulses) the effective nonlinear refractive index is

largest in magnitude, instantaneous and dominated by Rayleigh scattering. For broadband

excitation ($\sim$ picosecond pulses) the magnitude of the effective nonlinearity drops and the Raman

component becomes dominated by the delayed, rotational response. For ultrabroadband

excitation (femtosecond pulses), the effective nonlinearity asymptotes to a purely electronic

response [13, 14].

Section 2.8: The generalized nonlinear Schrödinger equation

In principle all nonlinear optical effects can be modeled through Eq. 2.3, the driven wave

equation. However, to save computational time much work has been dedicated to simplify

Maxwell's equations in order to produce pulse propagation equations that are easier to solve

using numerical techniques. There is an entire family of such propagation equations and the

nonlinear Schrödinger equation (NLS) is one such model [15]. Under the unidirectional

approximation, the paraxial approximation, the slowly varying envelope approximation and

using a reference frame moving with the laser pulse's group velocity, the NLS in the time

domain takes the form [8, 15, 16]:

$$\frac{\partial}{\partial \xi}\mathcal{E} = \frac{i}{k_0}\nabla_\perp^2\mathcal{E} - \frac{ik_2}{2}\frac{\partial^2}{\partial \tau^2}\mathcal{E} + \frac{i}{2n(\omega_0)}\frac{\omega_0}{c}\frac{P_{NL}}{\epsilon_0}.$$
(2.40)

Where the following coordinate transformations have been used: $z = \xi$ and $\tau = t - \frac{z}{v_g}$. In the above, the first term accounts for diffraction, the second term accounts for GVD and the third term accounts for the nonlinear response. Strictly speaking the NLS only involves cubic nonlinearities such that $P_{NL} \propto |\mathcal{E}|^2 \mathcal{E}$, however, any nonlinearity can be included. Equation 2.34 works well for picosecond pulses and longer but the model must be adjusted to handle very broadband problems and to include Raman scattering. This modified model is known as the Generalized Nonlinear Schrödinger Equation (GNLSE) and takes the following form [8]:

$$\frac{\partial}{\partial \xi} \mathcal{E} = \frac{i}{2k_0} \nabla_\perp^2 \mathcal{E} - \left(\sum_{n=0}^{m} k_n \frac{i^{n-1}}{n!} \frac{\partial^n}{\partial \tau^n} \right) \mathcal{E}$$
$$+ i n_2 k_0 \left(1 + \frac{1}{\omega_0} \frac{\partial}{\partial \tau} \right) \left\{ (1 - f_R) I \mathcal{E} + f_R \mathcal{E} \int_{-\infty}^{\infty} h_R(\tau) I(z, t - \tau) d\tau \right\}.$$

$$(2.41)$$

There are three main modifications to transform Eq. 2.40 into Eq. 2.41. The first modification involves the second term and is including the entire dispersion relation as defined in Eq. 2.26. The second modification involves the inclusion of a term $\frac{1}{\omega_0} \frac{\partial}{\partial \tau}$ in the nonlinear response that is used to account for self-steepening of the laser pulse. The third modification is the inclusion of the Raman response using Eq. 2.31, 2.32 and 2.34. It should be noted that Eq. 2.41 only accounts for the third-order nonlinearity evident by the inclusion of the nonlinear index n_2. In this thesis, Eq. 2.41 will be solved numerically to simulate the nonlinear propagation of intense 10 μm pulses in semiconductors. In doing so, we will restrict ourselves to 1-D simulations by neglecting the diffraction term in equation 2.41. However, a MATLAB code capable of simulating the 2-D GNLSE is presented in the appendix of this thesis.

Section 2.9: Nonlinear optics simulations of picosecond, 10 μm pulses

To illustrate the physics of mid-IR nonlinear pulse propagation in the positive and negative GVD regime it is useful to show the results of numerical simulations for common IR materials. To this end, the propagation of 1 ps, 10 μm laser pulses with a peak intensity of 10 GW/cm^2 in GaAs and n-Ge are considered. As with all simulations in this thesis, the 1D form of equation 2.41 is solved numerically using the split-step Fourier method [8].

The first simulation is dedicated to nonlinear pulse propagation in the positive GVD regime. For this case, n-Ge is chosen as the nonlinear medium having a nonlinear index of $n_2 = 3.7 \cdot 10^{-13} \frac{cm^2}{W}$ [17] and a GVD coefficient of $k_2 = 342 \frac{fs^2}{mm}$ [18]. The propagation length for both simulations are designed such that the laser pulse accumulates a nonlinear phase of 1.5 π radians, or such that the pulse traverses approximately 4.7 nonlinear lengths.

Figure 2.6 shows the spectral (Fig. 2.6a) and temporal (Fig. 2.6b) pulse profile both before and after propagating through 2 mm of n-Ge. Here the important parameters such as dispersive and nonlinear lengths are included in the title of the figure as a reference. As can be seen in Fig. 2.6, the pulse's spectrum is broadened considerably but the pulse's temporal duration does not change much. The only change in the temporal pulse profile of Fig. 2.6b is caused by the peak of the laser pulse experiencing a larger refractive index than the rest of the pulse. This effect, identified in the previous section, is known as nonlinear self-steepening. It should be noted that the spectral asymmetry apparent in Fig. 6a is also a result of self-steepening.

To illustrate propagation in the negative GVD regime we consider propagation in GaAs a material with a nonlinear index $n_2 = 0.4 \cdot 10^{-13} \frac{cm^2}{W}$ [17] and a GVD coefficient of $k_2 =$

$-1343 \frac{fs^2}{mm}$ [19]. Figure 2.7 depicts the spectral (Fig. 2.7a) and temporal (Fig. 2.7b) pulse

profiles before and after the laser pulse traverses approximately 2 mm of material. It should be

noted that this length in GaAs also results in a total nonlinear phase shift of 1.5 π radians, as was

the case with n-Ge.
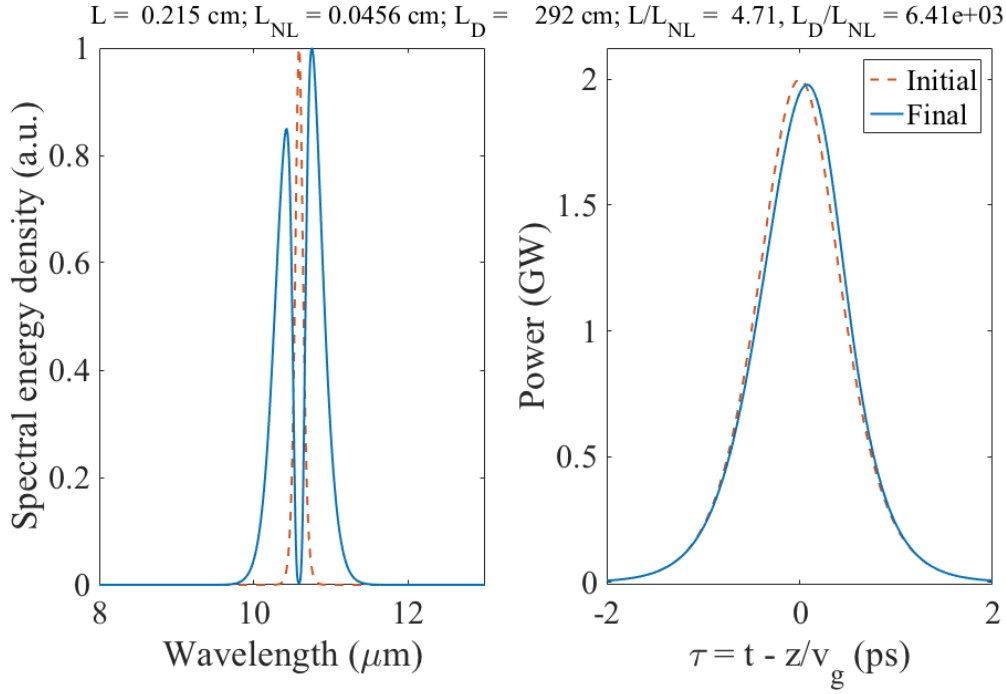
Figure 2.6: The simulated (a) spectral and (b) temporal pulse profile of an initially 1 ps, 10 μm

laser pulse before and after traversing approximately 2 mm of Ge.

   As can be inferred by comparing Fig. 2.6a and Fig. 2.7a, the laser pulse gained much more

bandwidth in the GaAs case, even though the pulse has traversed the same number of nonlinear

lengths. This is because the negative GVD of GaAs causes self-compression of the laser pulse,

evident in Fig. 2.7b where the laser pulse has been compressed such that its peak power has been

increased by a factor of four. It is clear that the negative GVD regime is favorable for the

generation of broadband light but can be problematic for applications requiring stability, such as nonlinear chirping followed by compression.
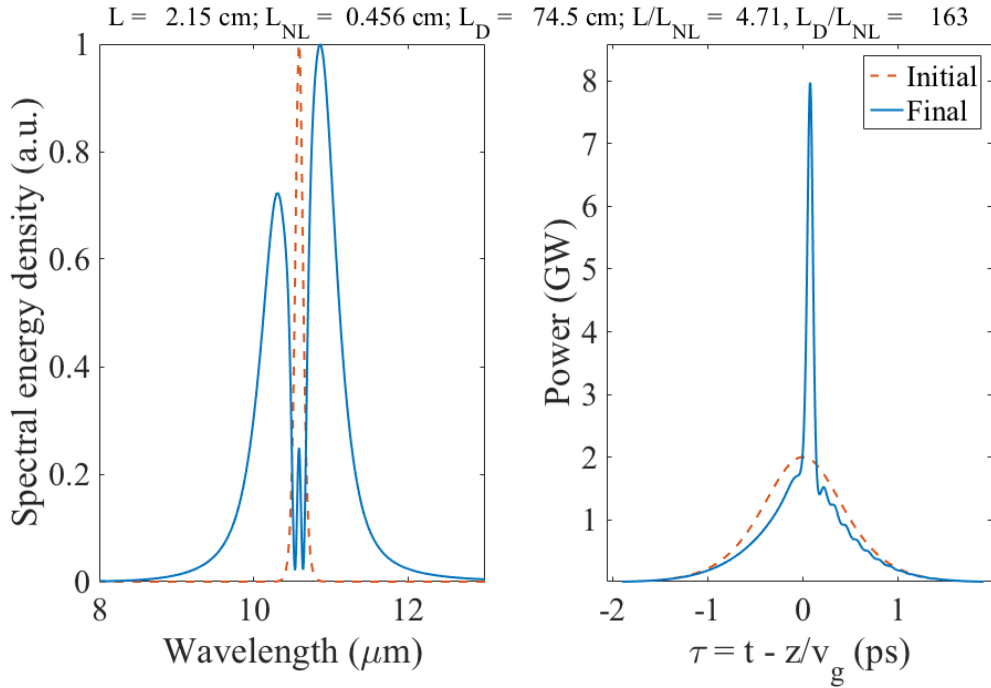
Figure 2.7: The simulated (a) spectral and (b) temporal pulse profile of an initially 1 ps, 10 μm laser pulse before and after traversing approximately 21 mm of GaAs.

References

[1] R. W. Boyd, *Nonlinear Optics*. Academic Press, New York (1992)

[2] J. M. Liu. *Photonic Devices*. Cambridge University Press, New York (2005)

[3] J.H. Marburger, "Self-focusing: Theory", Progress in Quantum Electronics **4**, 1 35-110. (1975)

[4] Y. R. Shen, *The Principles of Nonlinear Optics*. John Wiley & Sons, Inc., New York (1984)

[5] L. Bergé, S. Skupin, R. Nuter, J. Kasparian, J-P. Wolf. "Ultrashort filaments of light in weakly ionized, optically transparent media", Reports on Progress in Physics, **70**, 1633-1713 (2007).

[6] S. Minardi, A. Gopal, M. Tatarakis, A. Couairon, G. Tamosauskas, R. Piskarskas, A. Dubietis, P. Di Trapani, "Time-resolved refractive index and absorption mapping of light-plamsa filaments in water", Optics Letters, **33**, 86 (2008).

[7] F. F. Chen, *Introduction to Plasma Physics and Controlled Fusion,* Springer (2006)

[8] G. P. Agrawal, *Nonlinear Fiber Optics*, Academic Press, New York (2001)

[9] A. M. Ardilla, O. Martínez, M. Avella, J. Jiménez, B. Gérard, J. Napierala, and E. Gil-Lafon, "Temperature dependence of the Raman shift in GaAs conformal layers grown by hydride vapor phase epitaxy", Journal of Applied Physics, **91**, 5045 (2002)

[10] D. P. Shelton, J. E. Rice, "Measurements and Calculations of the Hyperpolarizabilities of Atoms and Small Molecules in the Gas Phase", Chemical Reviews, **94**, 3 (1994)

[11] A. M. Zheltikov, "Raman response function of atmospheric air", Optics Letters, **32**, 14, (2007)

[12] M. Morgen, W. Price, L. Hunziker, P. Ludowise, M. Blackwell, and Y. Chen, "Femtosecond Raman-induced polarization spectroscopy studies of rotational coherence in O2, N2 and CO2", Chemical Physics Letters, **209**, 1, (1993)

 [13] E. T. J. Nibbering, G. Grillon, M. A. Franco, B. S. Prade, and A. Mysyrowicz, "Determination of the intertial contribution to the nonlinear refractive index of air, N_2, and O_2 by

use of unfocused high-intensity femtosecond laser pulses", Journal of the Optical Society of America B, **14**, 3, (1997).

[14] J. K. Wahlstrand, Y. H. Cheng, and H. M. Milchberg, Physical Review A, **85**, 043820 (2012).

[15] A. Couairon, E. Brambilla, T. Corti, D. Majus, O. de J. Ramírez-Góngora, and M. Kolesik, "Practitioner's guide to laser pulse propagation models and simulation", The European Physical Journal Special Topics, **199**, 5-76 (2011).

[16] A. E. Siegman, *Lasers*, University Science Books, Mill Valley (1986).

[17] J. J. Wynne, "Optical Third-Order Mixing in GaAs, Ge, Si, and InAs*", Physical Review, **178**, 3, (1969).

[18] H. W. Icenogle, B. C. Platt, and W. L. Wolfe, "Refractive indexes and temperature coefficients of germanium and silicon", Applied Optics, **15**, 10, (1976).

[19] C. J. Johnson, G. H. Sherman, and R. Weil, "Far Infrared Measurement of the Dielectric Properties of GaAs and CdTe at 300 K and 8 K", Applied Optics, **8**, 8, (1969).

Chapter 3

The picosecond CO_2 laser at the UCLA Neptune Laboratory

Section 3.1 Introduction to picosecond CO_2 lasers

The carbon dioxide laser is the only practical radiation source for generating energetic ($0.1 - 1$ J) pulses of mid-IR light in the vicinity of 10 μm. Despite this fact, the CO_2 laser is not often used for many scientific research problems because it is difficult to amplify short (picosecond), high-power (1-100 GW) pulses in a gas laser having a relatively narrow bandwidth. Nevertheless, picosecond CO_2 lasers have been developed for more than thirty years [1] and have found niche applications where the long wavelength of the radiation provides access to novel parameter spaces for different applications. For example, TW-class CO_2 laser pulses have been applied to accelerate monoenergetic ions from a hydrogen gas-jet plasma where the long wavelength allowed for laser plasma interactions at near critical plasma densities in a gas target [2, 3]. Further, intense sources of mid-IR light can be used to access the negative GVD region of highly nonlinear semiconductors thus opening the possibility of generating white-light in the molecular fingerprint region of the electromagnetic spectrum, from $2 - 20$ μm [4, 5].

There is a two-step scheme for picosecond pulse amplification in the CO_2 laser. In the first step, a picosecond, 10 μm seed pulse is produced using a broadband solid-state laser. In the second step, this short seed pulse is amplified in CO_2 amplifiers where the gain media has been broadened by pressure and/or field broadening that will be described in detail below.

Section 3.2 Mechanisms to broaden the CO_2 gain medium

One method to increase the bandwidth of a gas laser is by pressure broadening. Figure 3.1 depicts a simulated CO_2 gain spectrum in the vicinity of the 10P branch at pressures of 1, 10 and 25 atm. At 1 atm, where CO_2 laser technology (so-called TEA lasers) is the most mature, the gain spectrum is comprised of individual rotational-vibrational lines each having a width of ~ 3.5 GHz/atm (Fig. 3.1a). Such systems are only capable of amplifying ~ 3 ns long pulses defined by the width of an individual rotational-vibrational line. Figure 3.1b and 3.1c show how the gain spectrum is broadened as the pressure of the gas is increased. As can be seen in Fig. 3.1c the gain spectrum becomes a continuum across the entire ~ 1.2 THz vibrational branch due to a complete overlap between the rotational lines when a pressure of 25 atm is achieved. Although the gain spectrum depicted in Fig. 3.1c is ideal for picosecond pulse amplification, it is extremely difficult to build large aperture lasers at pressures much greater than ~ 10 atm, thus limiting the operating pressure for practical power amplifiers. Amplification of a picosecond seed pulse in the 10 atm medium shown in Fig. 3.1b, results in amplification of a frequency-modulated laser pulse. In this scenario, the amplified pulse evolves into a picosecond pulse train with a pulse periodicity of 18.5 ps, a time constant related to the residual 55 GHz modulation visible in Fig. 3.1b. It should be noted that the ~1.2 THz bandwidth is sufficient to amplify picosecond 10 μm pulses.
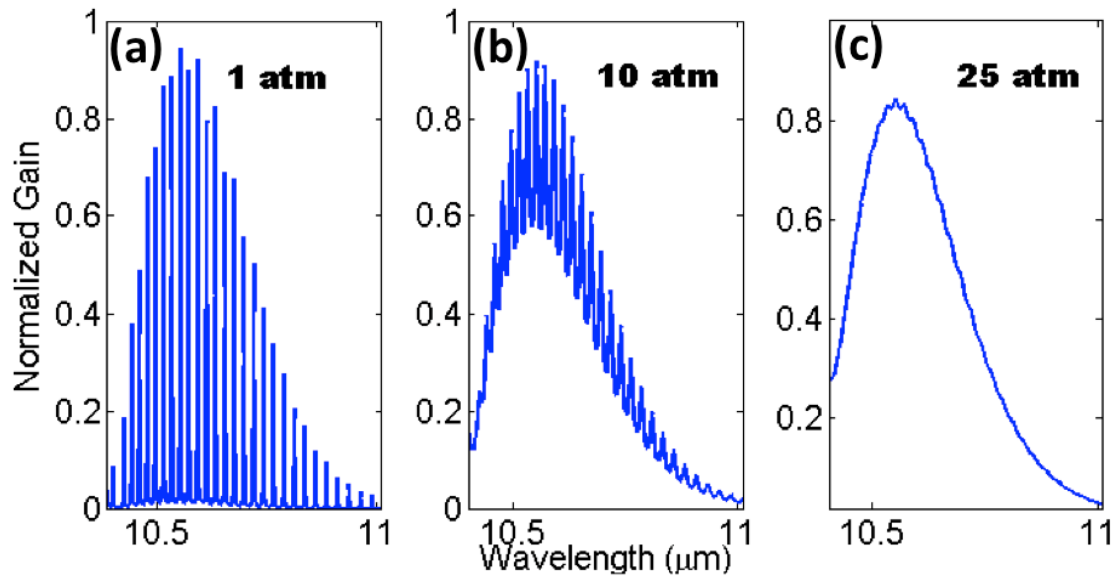
Figure 3.1: Simulated CO_2 gain spectra at (a) 1 atm, (b) 10 atm and (c) 25 atm of pressure illustrating the effect of pressure broadening.

A second method to increase the bandwidth available for amplification in the CO_2 gain medium is to use the strong field of the laser itself in an effect known as field broadening. Similar to how the energy levels in a quantum system can be shifted via the Stark effect, the a.c. electrical field of the laser can impart bandwidth onto a quantum amplifier by shifting the energy levels up and down in a time-dependent manner. Figure 3.2 shows a calculated shape of a CO_2 laser line both with and without the application of a strong laser field resonant with the transition, taken from reference [6]. As can be seen in Fig. 3.2, the application of a 2.8 MW/cm^2 field has broadened this line substantially. In general the amount of broadening gained via field broadening can be estimated using $\Delta v_{Field} \approx \Omega_{Rabi} = 1.38(10^7)\mu\sqrt{I}$. Where Ω_{Rabi} is the Rabi frequency, μ is the molecule's dipole moment in Debye and I is the intensity of the laser in W/cm^2 [6]. It should be noted that the dipole moment for the transition plotted in Fig. 3.2 is

orders of magnitude larger than the one used to amplify 10 µm light. For the 10P(20) transition of the CO_2 laser at 10.59 µm the dipole moment is 0.0275 D [7], therefore at an intensity of 10 GW/cm^2 a 1 atm CO_2 laser will be broadened such that it has comparable bandwidth to a 10 atm laser. In general, the amount of bandwidth available for amplification is a sum of the pressure- and field-broadened terms, $\Delta v_{Total} = \Delta v_{Pressure} + \Delta v_{Field}$.

Finally, it should be mentioned that the inclusion of isotopic CO_2 into the gain medium can also broaden the bandwidth available for picosecond pulse amplification. Here CO_2 molecules comprised of C-12 and O-16 are combined with molecules comprised of C-12 and O-18, where the inclusion of these isotopes has been shown to broaden and smooth the gain spectrum depicted in Fig. 3.1b [8]. The smoothing of the gain spectrum using high-pressure, isotopic CO_2 lasers can be used to produce a single, picosecond pulse as opposed to the picosecond pulse train that would be produced by amplifying a picosecond pulse in the gain spectrum depicted in Fig. 3.1b. Despite this advantage, isotopes are not widely used for large-aperture amplifiers because the large volumes make these systems expensive.
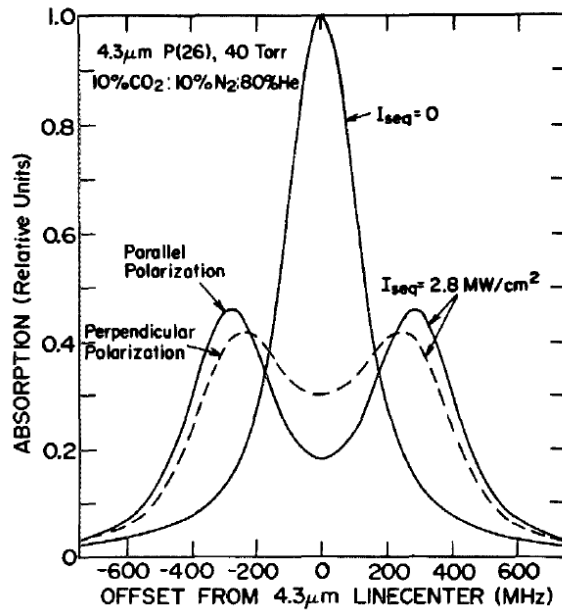
Figure 3.2: Calculated lineshape of a CO_2 gain line taken from reference [6] depicting the effect of a strong field on the bandwidth and shape of the line.

Section 3.3 The high-repetition rate, gigawatt power, CO_2 laser master-oscillator power-amplifier system at the UCLA Neptune Laboratory

The CO_2 laser master-oscillator power-amplifier (MOPA) system at the UCLA Neptune Laboratory relies on a combination of pressure and field broadening in order to amplify picosecond, 10 µm pulses to GW-level peak powers at a relatively high pulse repetition rate of 1 Hz [9] and to multi-TW peak powers using a large-aperture e-beam sustained amplifier that produces a laser pulse every 5-10 minutes. In this work only the high repetition rate configuration of the system was used so we describe it here in more detail. The picosecond seed is first amplified from nanojoule to millijoule energies in ~ 10 atm laser modules where the high pressure sustains the bandwidth necessary for picosecond pulse amplification. After the laser

pulse is sufficiently intense ($\sim 1 - 10$ GW/cm^2) industrial, transversely excited atmospheric (TEA) CO_2 laser modules are used for final amplification. In the final amplification stage it is the strong field of the laser that provides the bandwidth for picosecond pulse amplification.

Figure 3.3 is a block diagram of the UCLA MOPA system. The front-end, marked with the dashed box in Fig. 10, of the system consists of a CO_2 master oscillator and a Nd:Glass, 1 μm chirped pulse amplification (CPA) system. The master oscillator consists of an industrial TEA laser and two intracavity low-pressure lasers that allow for simultaneous amplification of two CO_2 laser lines, each on a single longitudinal mode. The picosecond, mid-IR seed is produced by imparting the bandwidth from the 1 μm CPA system onto the mid-IR output of the master oscillator using a CS_2 Kerr cell. In this scheme, the mid-IR and near-IR pulses, polarized 45^0 relative one another, are collinearly incident upon the Kerr cell. The intense near-IR pulse causes rotation of the mid-IR polarization via the Kerr effect such that the mid-IR pulse is effectively gated by crossed polarizers. This nonlinear optical interaction transcribes the temporal pulse profile from the near-IR light onto the mid-IR beam thus creating a dual-wavelength, picosecond pulse near 10 μm [10]. In this way, the front-end is able to produce $1 - 200$ ps long, mid-IR pulses by changing the compressor settings of the 1 μm system.
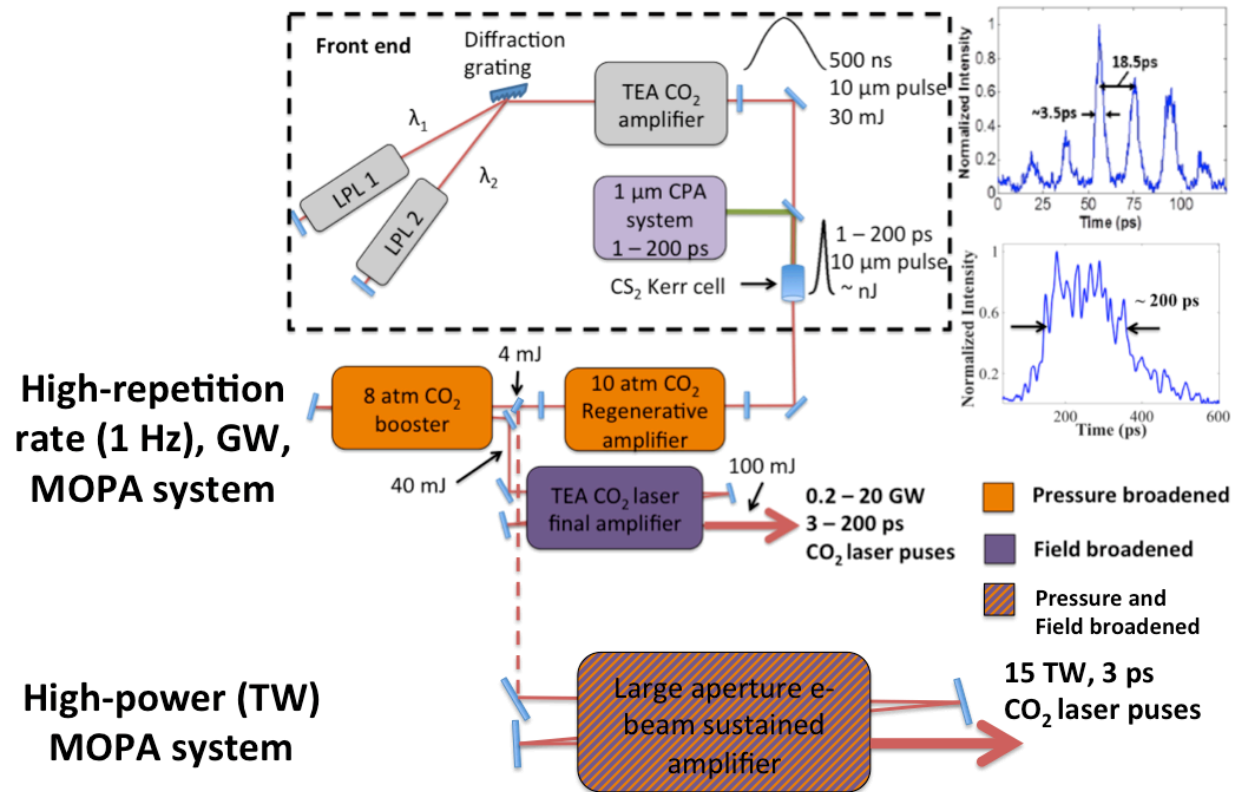
Figure 3.3: Block diagram of the UCLA Neptune Laboratory's picosecond CO_2 laser system. The upper inset is the temporal pulse profile of the 3 ps pulse train. The lower inset is the temporal pulse profile when a 200 ps seed is used. CPA stands for chirped pulse amplification, LPL stands for low-pressure laser and TEA stands for transversely excited atmospheric.

The mid-IR seed is amplified in a series of CO_2 amplifiers, shown in the block diagram of Fig. 3.3. The pulse is first amplified from ~ nJ energies to approximately 4 mJ in a 10 atm, regenerative amplifier. The pulse is then amplified to approximately 40 mJ in an 8 atm, booster amplifier used in a two-pass configuration. Finally, the pulse is amplified to 100 mJ in a TEA CO_2 laser that is used in a three-pass configuration.

If the system is seeded with a $1 - 3$ ps pulse, a ~ 3 ps pulse train is produced that is depicted in the upper inset of Fig. 3.3. This pulse train consists of $5 - 7$ pulses that are separated by 18.5

ps, a constant that is related to the 55 GHz modulation of the 10P branch (see Fig. 3.1b). If, instead, the system is seeded with a pulse that is longer than 20 ps, a smooth 200 ps pulse is amplified instead as can be seen in the lower inset of Fig. 3.3. The difference in temporal pulse formats is caused by how the seed's bandwidth overlaps with the CO_2 gain spectrum. In the case of the 3 ps pulse train, the seed's spectrum covers multiple rotational-vibrational lines, thus causing the 18.5 ps modulation in the time domain. In the 20 ps case, the seed's spectrum is overlapped with only one rotational-vibrational line.

The high-repetition rate, picosecond CO_2 laser system at the UCLA Neptune laboratory is able to provide 20 GW of peak power at a pulse repetition frequency of 1 Hz and is able to produce radiation at one or two wavelengths simultaneously. In the 200 ps configuration the peak-power is limited to approximately 2 GW. For the experiments presented in this thesis, both the 3 ps and 200 ps configurations will be used where the dual-frequency capability of the system has been used for four-wave mixing experiments in gases and solids.

References

[1] P. B. Corkum, "Ampification of Picosecond 10 µm Pulses in Multiatmosphere CO2 Lasers", IEEE Journal of Quantum Electronics, **21**, 3, (1985).

[2] C. A. J. Palmer, N. P. Dover, I. Pogorelsky, M. Babzien, G. I. Dudnikova, M. Ispiriyan, M. N. Polyanskiy, J. Schreiber, P. Shkolnikov, V. Yakimenko, and Z. Najmudin, "Monoenergetic Proton Beams Accelerated by a Radiation Pressure Driven Shock", Physical Review Letters, **106**, 014801, (2011).

[3] D. Haberberger, S. Tochitsky, F. Fiuza, C. Gong, R. A. Fonseca, L. O. Silva, W. B. Mori, and C. Joshi, "Collisionless shocks in laser-produced plasma generate monoenergetic high-energy proton beams", Nature Physics, **8**, 95-99 (2012).

[4] P. B. Corkum, P. P. Ho, R. R. Alfano, J. T. Manassah, "Generation of infrared supercontinuum covering 3 – 14 μm in dielectrics and semiconductors", Optics Letters, **10**, 12 (1985).

[5] J. J. Pigeon, S. Y. Tochitsky, C. Gong, and C. Joshi, "Supercontinuum generation from 2 – 20 μm in GaAs pumped by picosecond CO_2 laser pulses", Optics Letters, **39**, 11 (2014).

[6] R. K. Brimacombe and J. Reid, "Influence of the dynamic Stark effect on the small-signal gain of optically pumped 4.3-μm CO_2 lasers", Journal of Applied Physics, **58**, 1141 (1985).

[7] L. S. Rothman, I. E. Gordon, A. Barbe, D. C. Benner, P. F. Bernath, M. Birk, V. Boudon, L. R. Brown, A. Campargue, and J. -P. Champion, "The HITRAN 2008 molecular spectroscopic database," Journal of Quantitative Spectroscopy and Radiative Transfer, 110, 533-572 (2009).

[8] M. N. Polyanskiy, I. V. Pogorelsky, and V. Yakimenko, "Picosecond pulse amplification in isotopic CO_2 active medium", Optics Express, **19**, 8, 7717-7725 (2011).

[9] S. Ya. Tochitsky, J. J. Pigeon, D. J. Haberberger, C. Gong, and C. Joshi, "Amplification of multi-gigawatt 3 ps pulses in an atmospheric CO_2 laser using ac Stark effect", Optics Express, **20**, 13, 13762-13768 (2012)

[10] C. V. Filip, R. Narang, S. Ya. Tochitsky, C. E. Clayton, and C. Joshi, "Optical Kerr switching technique for the production of picosecond, multiwavelength CO_2 laser pulse", Applied Optics, **41**, 18, 3743-3747 (2002).

Chapter 4

Measurements of the nonlinear refractive index of atomic and molecular gases using four-wave mixing

Section 4.1 Introduction

Measurements of the nonlinear refractive index are of paramount importance both for the planning of nonlinear optics experiments and for the design of high peak-power laser systems. Here, the importance of experimental measurements is compounded by the fact that it is incredibly difficult to calculate the nonlinear index from first principles. Even scaling laws such as the generalized Miller's rule [1, 2] cannot estimate nonlinear index values that are accurate enough for most applications [3].

While the nonlinear refractive indices of most materials have been measured at visible and near-IR wavelengths, there is much less data for the mid-IR spectral range. In the mid-IR, highly nonlinear materials such as bulk semiconductors have been measured [4] but this data is scarce and has a large variation. Further, the low nonlinearities characteristic of gases have only been measured for the first time recently [5]. Indeed, the experiments presented in this chapter represent the first nonlinear index measurements of atomic and molecular gases in the long-wave IR. This data is important for the planning of experiments on mid-IR laser filamentation in the atmosphere where simulations [6] have shown the promise of long range, large diameter filaments in a region of the electromagnetic spectrum in which low-loss propagation in the atmosphere is possible.

42

Section 4.2 Methods to measure the nonlinear refractive index

In principle, any third-order nonlinear optical process can be used to measure the third-order susceptibility $\chi^{(3)}$. From this susceptibility the nonlinear refractive index can then be calculated by using Eq. 2.19 of Chapter 2. For such measurements, the processes of self-phase modulation (SPM) [7, 8], cross-phase modulation (XPM) [9, 10], third-harmonic generation (THG) [11], four-wave mixing (FWM) [4, 12, 13] and self-focusing [14] are most commonly used.

To extract the nonlinear refractive index, one must measure or infer the nonlinear phase shift that is given by $\phi_{NL} = n_2 k_0 IL$ for a diffraction free beam where n_2 is the nonlinear refractive index, k_0 is the vacuum wave number, I is the laser intensity and L is the length of the nonlinear medium. In the case of SPM or XPM, this nonlinear phase shift can be measured directly using interferometry. For THG and FWM the nonlinear phase shift must be inferred indirectly by measuring the efficiency of the production of newly generated frequencies. Direct phase measurements are typically employed for small nonlinear phase shifts on the order of 100 mrad while efficiency measurements are usually used to measure nonlinear phase shifts on the order of one radian or more. Through careful choice of laser pulse parameters and through the use of sensitive detectors it is possible, however, to measure the small nonlinear phase shifts characteristic of direct phase measurements using amplitude measurements. In this chapter we will show the results of FWM measurements that corresponded to < 100 mrad nonlinear phase shifts in gases. Aside from the use of a sensitive detector, these measurements were made possible by using relatively long laser pulses (200 ps) that had a high spectral energy density.

While atomic gases exhibit a purely electronic nonlinear response, nonlinear refractive index measurements of molecular gases represent an effective nonlinear index $n_{2,eff} = n_2 +$

$n_{2,Molecular}$, (see Eq. 2.39 and surrounding discussion in Chapter 2) where n_2 represents the purely electronic nonlinear response and $n_{2,Molecular}$ represents the contribution to the nonlinearity related to the instantaneous Rayleigh ($\Delta J = 0$) or delayed Raman ($\Delta J = \pm 2$) response. Here ΔJ is the change in the rotational quantum number. The relative contributions and magnitudes of the Rayleigh and Raman responses vary greatly dependent on laser pulse parameters with the Rayleigh part dominating for narrowband (~ ns pulse durations) and the Raman response dominating for broadband (~ ps pulse durations) laser pulses. The effective nonlinearity begins to asymptote to a purely electronic response for <100 fs pulse durations. It is therefore only possible to determine the relative contributions of the delayed molecular response and the instantaneous electronic response through time-resolved measurements [9, 10] or by measuring the effective nonlinear index for a range of laser pulse durations.

Section 4.3 Measurements of the nonlinear refractive index via four-wave mixing

All nonlinear index measurements presented in this chapter have been made by studying the FWM of a two-frequency (see Fig. 3.3 of Chapter 3) CO_2 laser pulse propagating through a nonlinear medium (see Chapter 3 for a detailed description of the laser system used for experiments). In doing so we have measured the FWM yield as a function of the intensity contained at each wavelength. To measure the nonlinear index of gases, long interaction lengths were necessary. In order to extract a meaningful nonlinear index, Eq. 2.14 of Chapter 2 was re-derived to account for the diffraction of the laser beam.

For mid-IR FWM experiments in gases, the phase-mismatch is negligible and we can re-write Eq. 2.13 as:

$$\frac{d}{dz}\mathcal{E}(z,\omega_3) \approx -\frac{i\omega_3^2 \mu_0}{2k(\omega_3)} \epsilon_0 \frac{3}{4} \chi^{(3)} \mathcal{E}^2(\omega_1)\mathcal{E}^*(\omega_2). \qquad (4.1)$$

Using the notation introduced in Fig. 2.1b and re-normalizing the complex amplitude such that $a_q a_q^* = I_q$, Eq. 4.1 can be re-written as for the first Stokes FWM component as:

$$\frac{d}{dz} a_3(z) = -\frac{i\omega_3}{c} \frac{\frac{3}{4}\chi^{(3)}}{c\epsilon_0\sqrt{n^2(\omega_1)n(\omega_2)n(\omega_3)}} a_1^2(z)a_2^*(z). \qquad (4.2)$$

Using $k_3 = \frac{\omega_3}{c}$, $n_2 = \frac{\frac{3}{4}\chi^{(3)}}{c\epsilon_0\sqrt{n^2(\omega_1)n(\omega_2)n(\omega_3)}}$ and integrating along the interaction length, L, Eq. 4.2 becomes:

$$a_3 = -ik_3 n_2 \int_0^L a_1^2(z)a_2^*(z)dz. \qquad (4.3)$$

This can be written in terms of intensities as:

$$I_3 = k_3^2 n_2^2 \left(\int_0^L I_1(z)\sqrt{I_2}(z)\,dz \right)^2. \qquad (4.4)$$

Since the energy contained in the FWM sideband and both pump pulses are measured in the experiment, it is useful to express Eq. 4.4 in terms of pulse energy. This is accomplished by using the definition of intensity $I_q = \frac{P_q}{S(z)} = \frac{W_q}{\tau_q S_q(z)}$, where P is the power, W is the energy contained in the pulse, τ is the temporal pulse length and S is the area of the beam given by $S(z) = \pi a(z)b(z)$, where a and b are the major and minor axes of the elliptical beam used in the experiment, respectively. With these definitions Eq. 4.4 can be re-written as:

$$I_3(z) = \frac{k_3^2 n_2^2 W_1^2 W_2}{\tau^3} \left(\int_0^L \frac{dz}{(\pi a(z)b(z))^{\frac{3}{2}}} \right)^2. \qquad (4.5)$$

Note that, for Eq. 4.5 it is assumed that both pumps have the same spatial distribution and temporal pulse length. The integral in Eq. 4.5 was evaluated by high-resolution spatial

measurements of the beam along the entire interaction length as will be explained in the next section of this chapter. Finally, the intensity of the FWM sideband can be expressed as $I_3 = \frac{W_3}{S_3 \tau'}$, where S_3 is the area, and τ' is the pulse length of the FWM beam. In the low efficiency limit $\tau' = \frac{\tau}{\sqrt{3}}$ [15] such that Eq. 4.5 can be written as:

$$W_3 = \frac{k_3^2 n_2^2 W_1^2 W_2 S_3}{\sqrt{3}\tau^2} \left(\int_0^L \frac{dz}{(\pi a(z) b(z))^{\frac{3}{2}}} \right)^2. \tag{4.6}$$

According to Eq. 4.6, the nonlinear index is related to the slope of a plot of the FWM sideband energy as a function of $W_1^2 W_2$.

Section 4.4 Measurements of the nonlinear refractive index of atomic and molecular gases

Measurements were carried out using 200 MW, 200 ps CO_2 laser pulses comprised of radiation amplified on the 10P(20) (10.59 µm) and 10R(16) (10.27 µm) lines of the CO_2 laser, as depicted in Fig. 4.1a. Figure 4.1b shows the experimental set-up for nonlinear index measurements in gases. The laser pulses were focused with a 2.5 m focal length NaCl lens through a 2 m long cell, as shown in Fig. 4.1b. For this experiment peak intensities of ~ 15 GW/cm^2 were used. After the cell, the pump beams were separated from the FWM sideband with the use of a 150 G/mm diffraction grating. After the first diffraction grating, the FWM sideband of interest was sent through a scanning monochromator to further isolate the signal from the energetic pump. This configuration allowed for the detection of FWM energies on the order of 10^{-7} relative to the pump.
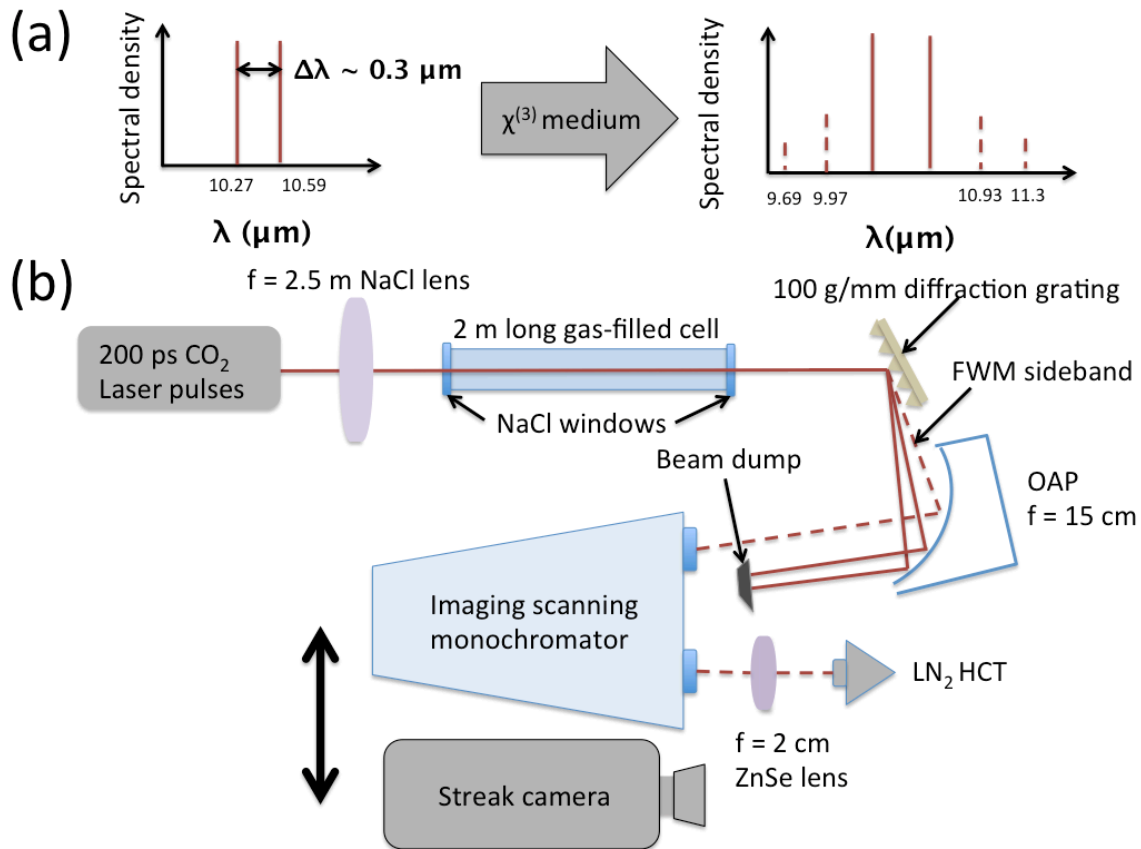
Figure 4.1: (a) A dual-wavelength laser pulse is transformed into a series of sidebands by FWM in a nonlinear medium. (b) Experimental set-up for nonlinear index measurements of gases.

The sensitivity of the detection scheme necessitated a careful analysis of the background FWM light that was produced in several IR optical elements and in the transport of the high-power beam through the air. This was accomplished by taking background measurements in He gas, which has a nonlinear refractive index approximately 20x smaller than that of the air. It should be noted that vacuum measurements did not serve as an adequate assessment of the FWM background because intra-cell optics produced a spatial shift at differing pressures. Temporal measurements of the pump pulses were accomplished by transcribing the temporal pulse length from the mid-IR pump to a 658 nm probe by polarization rotation in a CS_2 Kerr cell [16]. The

visible probe's temporal pulse duration was then measured using a picosecond streak camera

with a ~ 5 ps resolution. Over twelve laser shots the temporal pulse length of the pump was

found to be 197 ± 21 ps. Figure 4.2 depicts a representative temporal pulse profile as measured

with the streak camera.
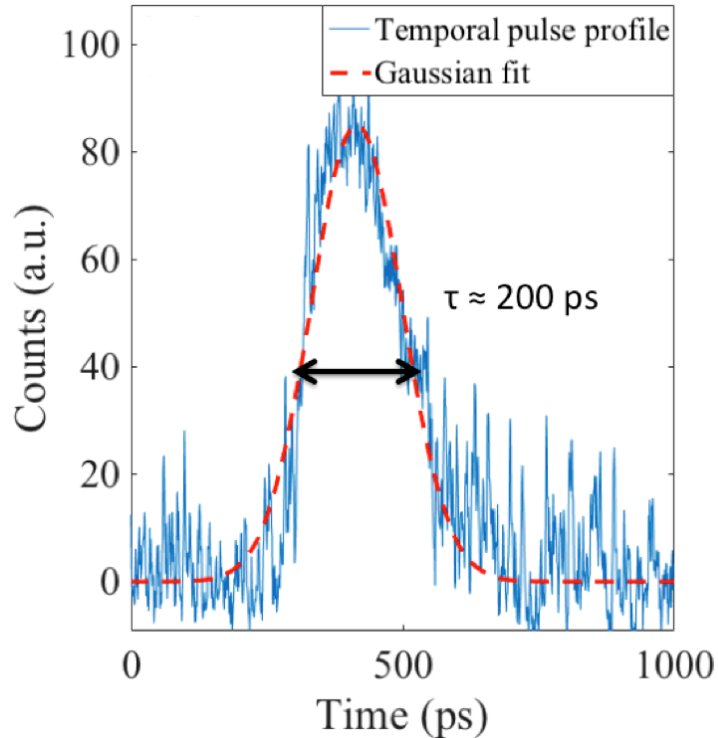
Figure 4.2: (a) Measurement of a representative temporal pulse profile used for nonlinear index

measurements.

To study the FWM process in gases we first measured the dependence of the FWM sideband

yield as a function of cell pressure. Figure 4.3 shows this dependence for the first anti-Stokes

sidebands for input powers of ~ 200 and 130 MW in laboratory air at pressures ranging from 380

to 760 torr. Since the nonlinear index should vary linearly with fill pressure, one would expect

the curves of Fig. 4.3 to be quadratic as a function of pressure. Instead we have observed a linear

dependence for the 130 MW case and saturation for the 200 MW case at high pressure. This

deviation from theoretical scaling is attributed to the onset of collisional ionization near the focus

of the pump beam. This ionization causes refraction of the FWM sideband resulting in a

reduction of the collection efficiency for our detection scheme. This is consistent with the

observation of fluorescence associated with plasma recombination at high pressures and

intensities.
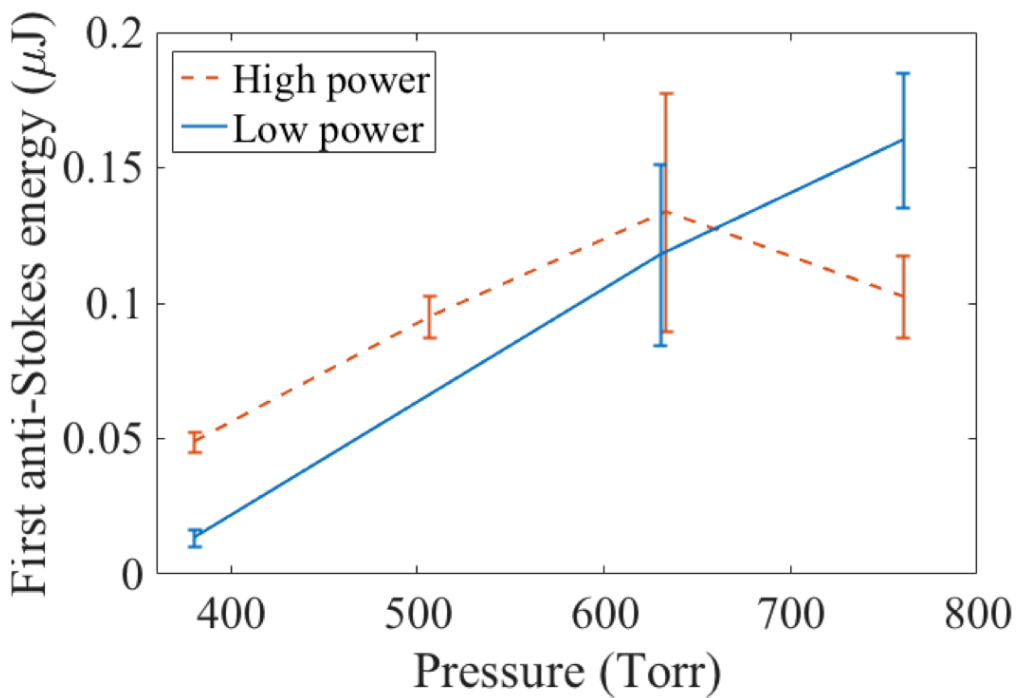
Figure 4.3: Energy of the first anti-Stokes sideband as a function of pressure in laboratory air.

The dashed and solid lines were produced using 200 and 130 MW, respectively.

To avoid the contribution of plasma formation we have limited quantitative measurements of

the nonlinear index to pure gases at pressures below 380 torr. Figure 4.4 shows a result of such a

measurement in 250 torr of oxygen gas and 250 torr of helium gas, used as a background

measurement. In Fig. 4.4 we have plotted the FWM yield as a function of $W_1^2 W_2$ as defined in

Eq. 4.6. As can be seen, the linear dependence obtained for both the sample gas and the background suggests that the effects of ionization are negligible at these pressures. Figures 4.5 and 4.6 show this same dependence for nitrogen gas and for dry air.
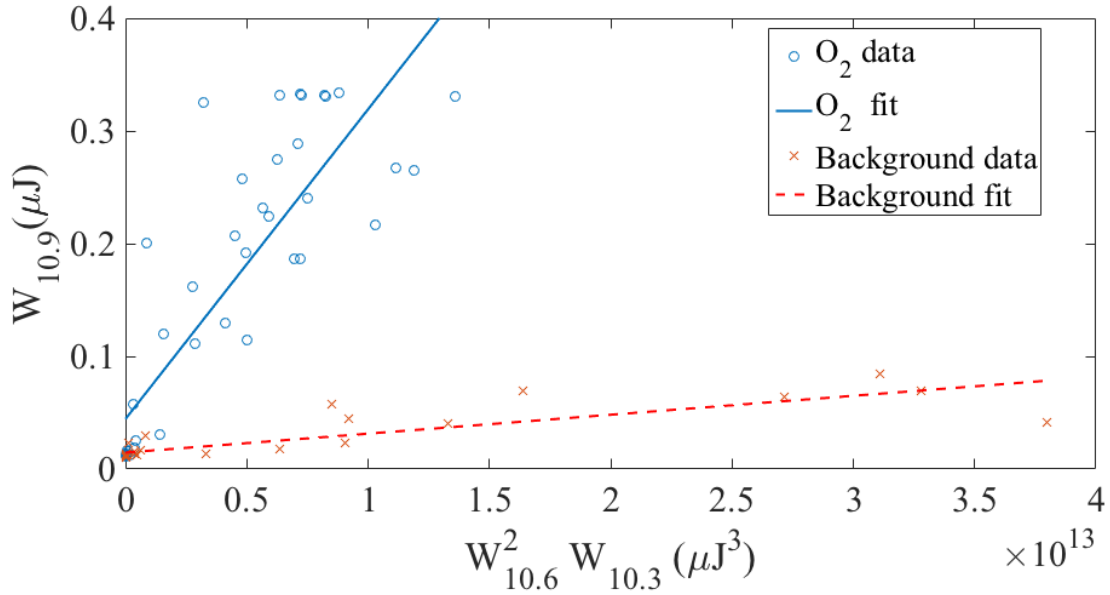
Figure 4.4: Energy in the first stokes sideband plotted as a function of the energy of the 10.6 μm pump times the energy in the 10.3 μm pump squared for 250 torr of oxygen gas. Note that W_λ stands for the energy contained at wavelength λ in microns.
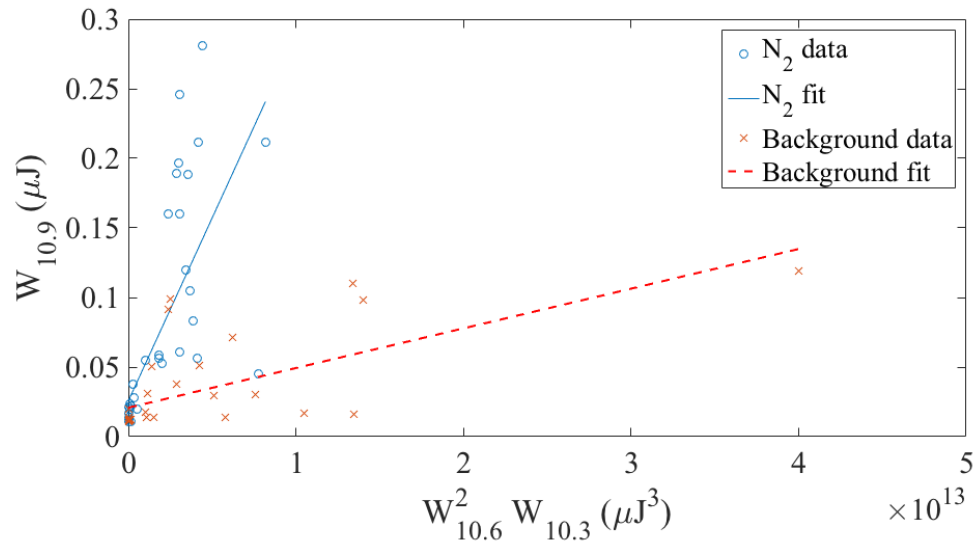
Figure 4.5: Energy in the first stokes sideband plotted as a function of the energy of the 10.6 μm pump times the energy in the 10.3 μm pump squared for 380 torr of nitrogen gas. Note that W_λ stands for the energy contained at wavelength λ in microns.
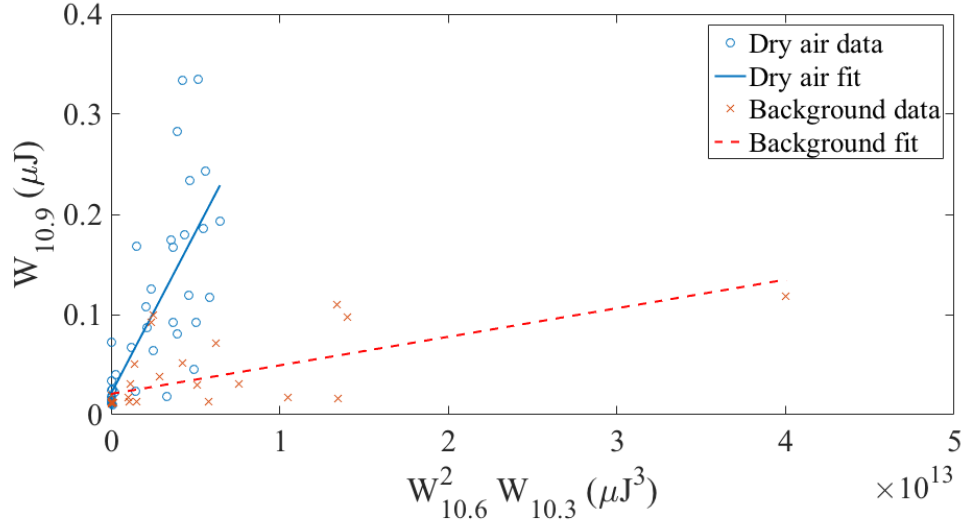
Figure 4.6: Energy in the first stokes sideband plotted as a function of the energy of the 10.6 μm pump times the energy in the 10.3 μm pump squared for 380 torr of dry air. Note that W_λ stands for the energy contained at wavelength λ in microns.

To understand the symmetry of the FWM spectrum we measured the yield of the 2nd Stokes and the 1st and 2nd anti-Stokes sidebands. Figure 4.7 shows a typical FWM spectrum obtained in 380 torr of laboratory air. The amplitude of the FWM sidebands shown in Fig. 4.7 were obtained by taking the difference between the average FWM signal obtained in He gas and laboratory air of the same pressure. In this case, we have averaged 10 laser shots of comparable input pulse parameters. The FWM spectrum depicted in Fig. 4.7 is likely asymmetric because the delayed, rotational Raman response plays a significant role in the effective nonlinearity for 200 ps pulses. The FWM spectra observed for noble gases, exhibiting only an instantaneous electronic nonlinearity, was found to be symmetric. Figures 4.8 and 4.9 show the FWM yield as a function of $W_1^2 W_2$ as defined in Eq. 4.6 for xenon and krypton gas.
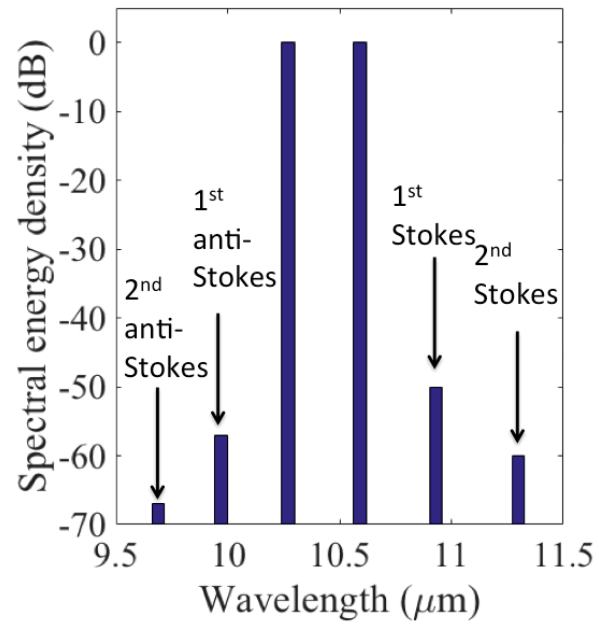
Figure 4.7: A typical FWM spectrum obtained in 380 torr of laboratory air.
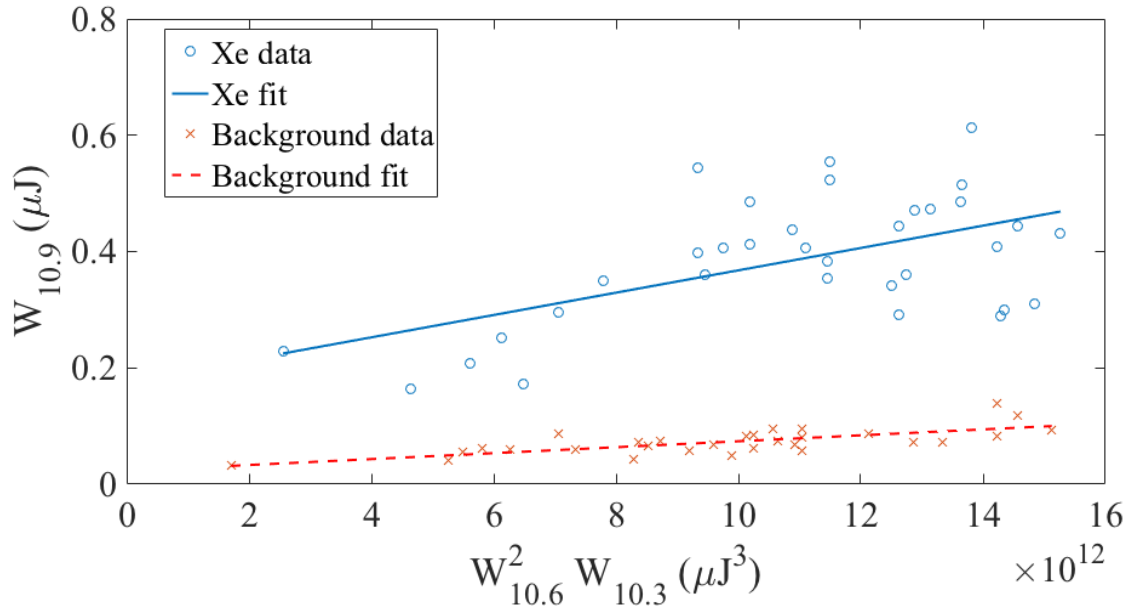
Figure 4.8: Energy in the first stokes sideband plotted as a function of the energy of the 10.6 μm pump times the energy in the 10.3 μm pump squared for 380 torr of Xenon gas. Note that W_λ stands for the energy contained at wavelength λ in microns.
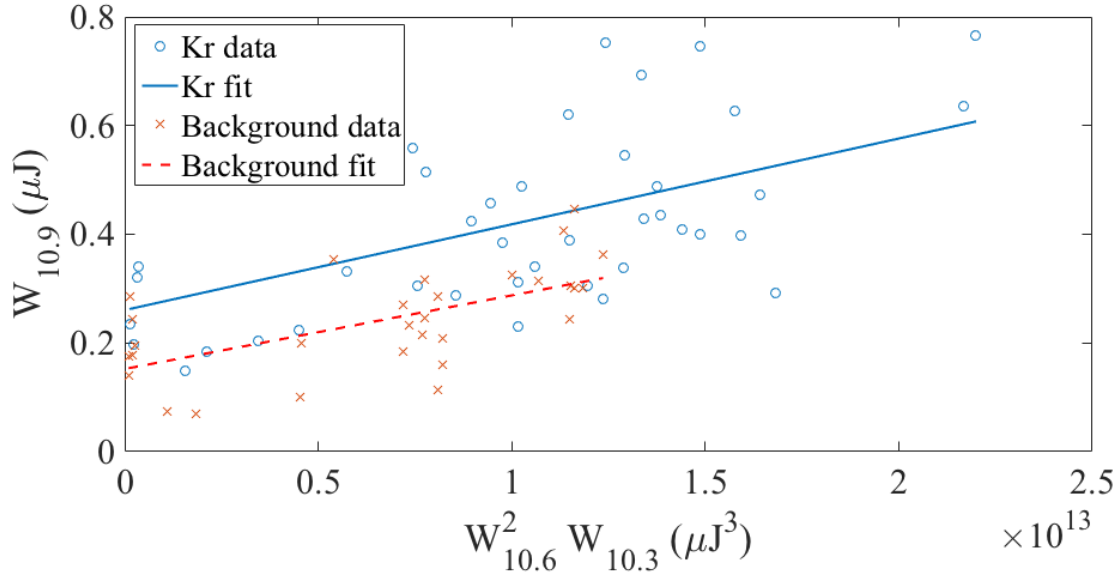
Figure 4.9: Energy in the first stokes sideband plotted as a function of the energy of the 10.6 μm pump times the energy in the 10.3 μm pump squared for 380 torr of krypton gas. Note that W_λ stands for the energy contained at wavelength λ in microns.

The nonlinear index can be extracted from the difference in slope between the sample and background curves of Fig. 4.4 – 4.6 and 4.8, 4.9 in accordance with Eq. 4.6. To calculate these values we first needed to account for the diffraction of the laser beam. This was accomplished by high-resolution spatial measurements of the expansion of the beam using a pyroelectric camera. These images were then manually analyzed to extract the major and minor axes of the elliptical beam used for measurements. Figure 4.10 shows a plot of the extracted major and minor axes, the insets of the figure show sample images obtained with the pyroelectric camera. Here, the use of a single focusing lens resulted in clear astigmatism, visible in Fig. 4.10. Nevertheless, the beam reaches a minimum $1/e^2$ size of ~ 600 μm that corresponds to peak intensities on the order of 15 GW/cm^2 for the highest energy laser pulses shown in Fig. 4.4-4.6 and Fig. 4.8, 4.9. The

area below the curves of Fig. 4.10 were evaluated by numerical integration in order to calculate nonlinear index values using Eq. 4.6.
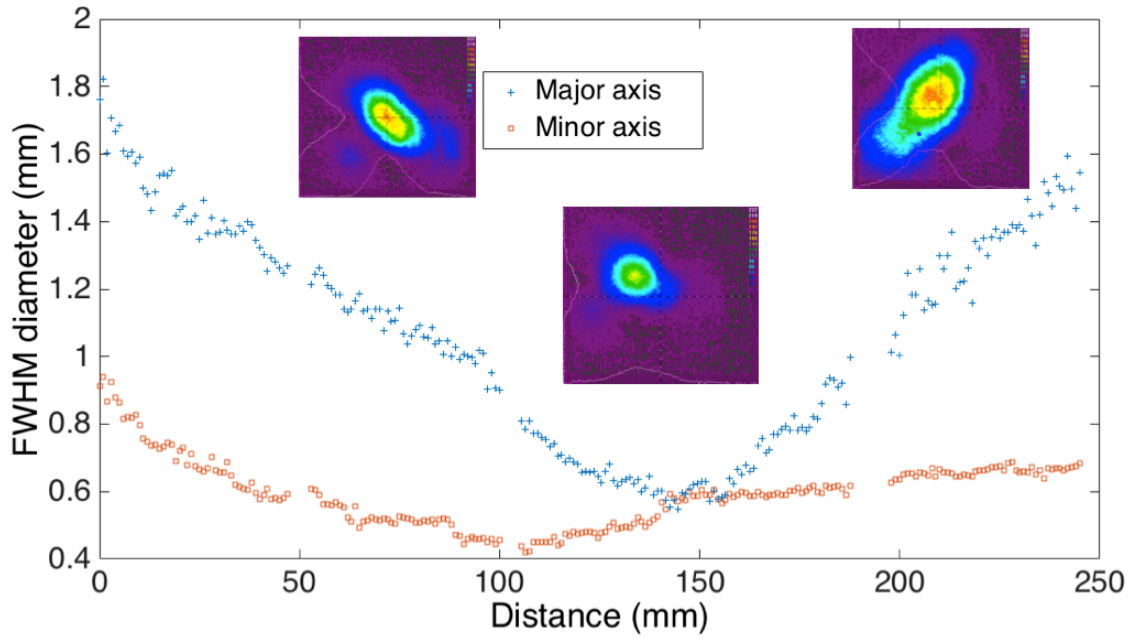
Figure 4.10: The evolution of the major and minor axes of the elliptical beam used for nonlinear refractive index measurements in gases. The insets of the figure show example images of the beam as measured with a pyroelectric camera.

To calculate the experimental uncertainty in these measurements we have included the uncertainty in the least-squares fit of both the sample gas and the He background, the uncertainty in the laser pulse measurements, and the uncertainty in evaluating the integral of Eq. 4.6. The uncertainties were added in quadrature as:

$$\frac{\sigma_{n_2}}{n_2} = \sqrt{\left(\frac{\sigma_{\Delta m}}{2\Delta m}\right)^2 + \left(\frac{\sigma_{\tau}}{\tau}\right)^2 + \left(\frac{\sigma_{\Phi}}{\Phi}\right)^2} \tag{4.7}$$

Where Δm is the difference in slope between the sample and background gas, τ is the laser pulse length, and Φ is the result of the integral of Eq. 4.6. Finally, σ_x is the uncertainty associated with the quantity x. The uncertainty in Δm was found by adding the uncertainty in the least-squares fit of both the sample and background gas in quadrature. This uncertainty, different for all gases, was on the order of $15 - 20\%$ and dominated the uncertainty in the nonlinear index measurements. The uncertainty in the pulse length was taken as the standard deviation of 12 consecutive measurements of the laser pulse length and was found to be $\sim 11\%$. A typical measurement of this type can be seen in Fig. 4.2. Finally, the uncertainty in the numerical integral was estimated by considering the difference between an ideal Gaussian beam and the beam used for measurements. Here we have calculated the area under the curve for an ideal Gaussian beam having a waist of ~ 300 μm, as measured in experiment, and have compared this with the area under the curves plotted in Fig. 4.10. The difference between these two integrals was only found to be 2.3 %. This small difference arises because it is only the focal region that significantly contributes to this integral. In order to remain conservative, however, we have assumed that the uncertainty in our measurements could be off by as much as 10%. Even assuming such a large uncertainty for this integral, it is still the uncertainty in the determination of the slopes of the best-fit lines shown in Fig. 4.4-4.6 and 4.8, 4.9 that dominates the total uncertainty in measurements of the nonlinear refractive index. The MATLAB code used to extract the slope uncertainties and to calculate the numerical integral can be found in the Appendix C of this dissertation.

We first present nonlinear refractive index values obtained for the noble gases since they exhibit a solely electronic nonlinearity. Table 4.1 summarizes our measurements for the nonlinear index of noble gases. Here we were able to measure the nonlinearity of Kr and Xe but were unable to detect substantial

FWM in Ar gas. In presenting our data we have compared our measurements with those measured at 0.8 μm [17]. In addition, we have calculated theoretical values of the nonlinear index by extrapolating the 0.8 μm data to 10.6 μm using the generalized Miller's rule [2] (see Appendix E for a simple derivation of Miller's rule for the third-order susceptibility). As can be seen in Table 4.1, we have observed a faster decrease in the nonlinear index than what is predicted by the Miller's rule scaling.

Table 4.1: Nonlinear indices for noble gases scaled to 1 atm

Gas species	$\lambda = 0.8$ μm [17]	$\lambda = 10.6$ μm (calculated)[a]	$\lambda = 10.6$ μm (measured)
	$n_2(10^{-19}\,cm^2/W)$	$n_2(10^{-19}\,cm^2/W)$	$n_2(10^{-19}\,cm^2/W)$
Ar	0.97 ± 0.12	0.95 ± 0.12	<1[b]
Kr	2.2 ± 0.4	2.2 ± 0.4	1.4 ± 0.3
Xe	5.8 ± 1.1	5.6 ± 1.1	3.5 ± 0.8

[a]Calculated using the generalized Miller's formula [2]

[b]Not measureable using our set-up.

One possible explanation for this decrease may be strong field effects caused by the large ponderomotive energy generated by 10.6 μm radiation focused to intensities of 10^{10} W/cm^2. This is an equivalent ponderomotive energy as a 0.8 μm pulse being focused to an intensity of 10^{12} W/cm^2 for which saturation of the electronic nonlinearity has been predicted to occur [18-21]. This saturation may result from higher-order, self-defocusing susceptibilities [18, 19] or from the dynamics of weak ionization that affect the nonlinear polarizability [20, 21]. These higher-order effects may not be observable in the near-IR since they occur at intensities that inevitably cause optical field ionization [17, 18] but may be observable in the long-wave IR. Another possible explanation for these observations is a strong coupling

between the fundamental field and harmonic components that are perfectly phase-matched in the mid-IR causing a steepening of the optical waveform thus changing the nonlinear polarizability [22]. However, it should be noted that no significant third or fifth harmonic was observed in these experiments. Clearly, additional experimental data is required to fully determine the cause of these observations. Future experiments dedicated to nonlinear refractive index measurements at other mid-IR wavelengths or as a function of intensity may elucidate how the nonlinear polarizability changes at long wavelengths.

Table 4.2 summarizes the measurements for molecular nitrogen, oxygen, and the air. Here we have presented our measurements for the effective nonlinear index of refraction, $n_{2,eff} = n_{2,elec} + n_{2,Molecular}$, and have compared these results to those obtained at 0.8 and 2.4 μm. As can be seen from Table 4.2, our nonlinear index measurements are very close to those obtained at near-IR wavelengths.

Table 4.2: Effective nonlinear indices for major air constituents scaled to 1 atm

Gas Species	λ = 0.8 μm [8]	λ = 2.4 μm [10]	λ = 10.6 μm
	$n_{2,eff}$ (10^{-19} cm^2/W)	$n_{2,eff}$ (10^{-19} cm^2/W)	$n_{2,eff}$ (10^{-19} cm^2/W)
N_2	3 ± 0.7	3.2 ± 0.5[b]	4.5 ± 0.9
O_2	8 ± 2.2	6.4 ± 0.8[b]	8.4 ± 1.3
Air	4 ± 1.1[a]	-	5.0 ± 0.9

[a]Calculated from measurements of N_2, O_2 and Ar.

[b]Calculated from measurements in S. Zahedpour, *et. al.* using $n_{2, eff}$=n_2 + $n_{2,rot}$ [10].

Since we have used FWM of an 882 GHz beat-wave for these measurements, it behooves us to argue that we have measured the non-resonant third-order nonlinearity that is related to the nonlinear refractive

index. Indeed, nitrogen and oxygen have multiple rotational transitions that occur in a frequency range close to the 882 GHz beat-frequency used for measurements and the use of nondegenerate FWM may introduce an increase to the nonlinear response of a molecule [3]. To investigate the potential contribution of a resonant enhancement to the rotational nonlinearity we have plotted the resonant, rotational hyperpolarizability of single oxygen and nitrogen molecules in the vicinity of 882 GHz using Eq. 34 of reference [3]. It should be noted that the hyperpolarizability is related to the third-order nonlinear polarizability by $P_{NL}^{(3)} = N\gamma$, where N is the number of molecules and γ is the hyperpolarizability. The results of this calculation are presented in Fig. 4.11 that shows a plot of the resonant hyperpolarizability as a function of beat-frequency in the range from 400 to 1200 GHz (see Fig. 4.11a) and zoomed in the vicinity of the 882 GHz beat frequency (see Fig. 4.11b). In Fig. 4.11, the peaks are related to the Raman lines of nitrogen and oxygen.

The selection rules for Raman scattering of diatomic molecules is $\Delta J = 0, \pm 2$, where $\Delta J = J_f - J_i$ is the change in the rotational quantum number between initial state i and final state f. Here $\Delta J = 0$ is responsible for elastic, Rayleigh scattering and $\Delta J = \pm 2$ is related to inelastic, Raman scattering. As seen in Fig. 4.11 the closest transition to the beat-frequency used in measurements is at 840 GHz and is related to the J = 4 to J = 2 transition of the nitrogen molecule. However, since the both the linewidth of this transition and the bandwidth of the pump pulse used for measurements are ~ 2 GHz, the 42 GHz separation between this transition and the beat-frequency may make the resonant contribution negligible. However, additional measurements using a degenerate four-wave mixing process such as SPM are still required to rule out a possible resonant contribution to the effective nonlinear refractive indices presented in Table 4.2.
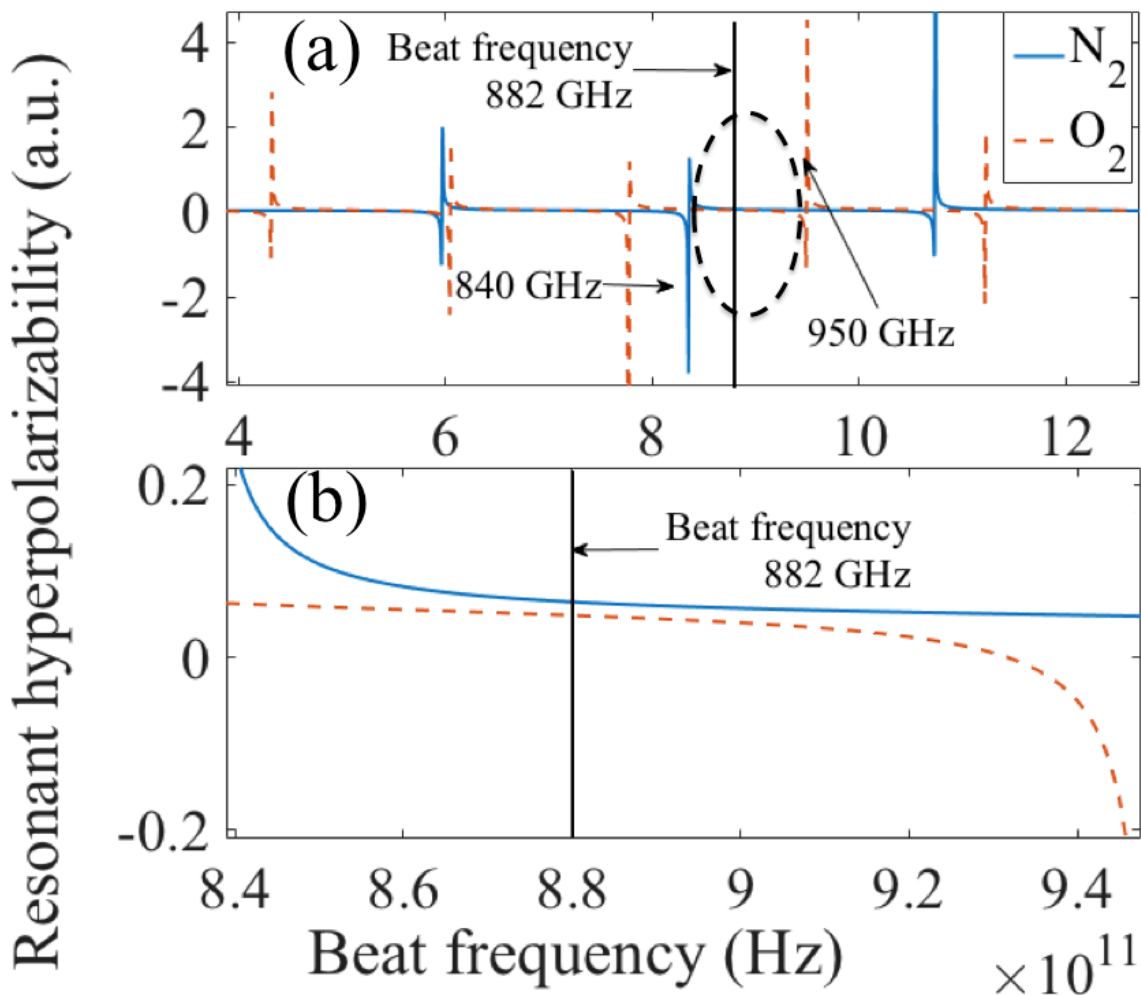
Figure 4.11: (a) The resonant third-order polarizability per molecule of N_2 and O_2 in the range of 400 to 1200 GHz and (b) zoomed in the vicinity of the 882 GHz beat frequency used for nonlinear refractive index measurements. The zoomed area is denoted by the dashed oval in (a).

Finally, the fact that we have measured smaller nonlinearities in the noble gases Xe and Kr than what was calculated using Miller's scaling implies that the purely electronic nonlinearity may be smaller in the long-wave IR than at shorter wavelengths. This finding has implications for our measurements in molecular gases as well since the effective nonlinearity is a combination of an electronic and rotational response. Since we have measured a comparable nonlinearity at 10.6 μm than that observed in the near-

IR, this implies that the rotational nonlinearity is larger in magnitude in the long-wave IR. Additional measurements of the nonlinear refractive index using shorter laser pulses or using a time-resolved measurement technique are required to quantify the magnitude of the rotational nonlinear response in this spectral range. The use of shorter pulses may make it possible to measure nonlinearities using ~ 100 GW/cm^2 intensities with a reduced probability of avalanche ionization. Such fields may be used to study whether or not there is intensity dependence to electronic nonlinearities driven by long-wave IR fields.

Section 4.5 Measurements of the nonlinear refractive index of GaAs

Since the next two chapters of this thesis will be dedicated to nonlinear optics experiments in semiconductors, we have also measured the nonlinear index of GaAs using the same FWM technique described above. In doing so, we have effectively repeated an experiment carried out by Wynne [4] in which the nonlinear index of GaAs was measured via FWM of a CO_2 laser pulse comprised of radiation near ~ 9 μm and ~ 10 μm.

For nonlinear index measurements in GaAs ~ 300 ns long CO_2 laser pulses, produced with the master-oscillator of the CO_2 MOPA system (see Chapter 3), were focused to a peak intensity of ~ 1 MW/cm^2 and transmitted through a 7 mm long, AR-coated GaAs slab. The output radiation was dispersed on a single diffraction grating such that the sideband energy and the energy in each pump could be measured as shown in Fig. 4.12.
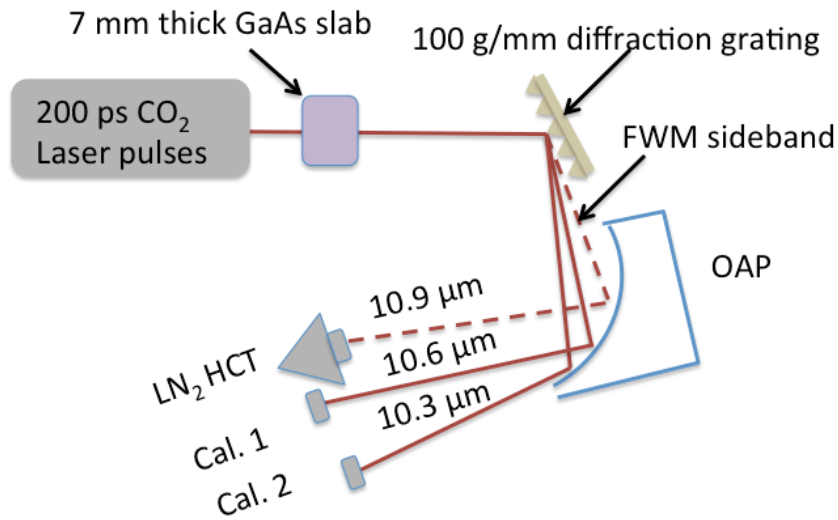
Figure 4.12: The experimental set-up for nonlinear refractive index measurements in GaAs.

OAP: off-axis parabolic mirror, HCT: HgCdTe and Cal.: calorimeter.

The nonlinear index of GaAs was extracted from the slope of a plot of the FWM sideband energy as a function of the energy in the pump waves as was described in section 4.4. Table 4.3, below, shows the result of our measurement and that obtained by Wynne [4]. As can be inferred from Table 4.3, our nonlinear index measurement is equal to the literature value but with a smaller error bar. It should be noted that this measurement also provides additional validity to the analysis presented in section 4.4 for atomic and molecular gases.

Table 4.3: Nonlinear refractive index of GaAs obtained via FWM at UCLA compared with the value reported in [4].

	Result from J. J. Wynne [4]	UCLA Experiment
n_2 of GaAs (10^{-14} cm^2/W)	4 ± 2	4.1 ± 0.5

References

[1] R. C. Miller, "Optical second harmonic generation in piezoelectric crystals", Applied Physics Letters, **5,** 1 (1964).

[2] W. Ettoumi, Y. Petit, J. Kasparian, and J.-P. Wolf, "Generalized Miller Formulae", Optics Express", **18**, 7, 6613-6620 (2010).

[3] D. P. Shelton and J. E. Rice, "Measurements and Calculations of the Hyperpolarizabilities of Atoms and Small Molecules in the Gas Phase", Chemical Review, **94**, 3-29, (1994).

[4] J. J. Wynne, "Optical Third-Order Mixing in GaAs, Ge, Si, and InAs*", Physical Review, **178**, 3, (1969).

[5] J. J. Pigeon, S. Ya. Tochitsky, E. C. Welch, and C. Joshi, "Measurements of the nonlinear refractive index of air, N_2, and O_2 at 10 μm using four-wave mixing", Optics Letters, **41**, 16 (2016).

[6] Y. E. Geints and A. A. Zemlyanov, "Single and multiple filamentation of multi-terawatt CO_2-laser pulses in air: numerical simulations", Journal of the Optical Society of America B, **31**, 4, 788-797 (2014).

[7] M. J. Shaw, C. J. Hooker, and D. C. Wilson, "Measurement of the nonlinear refractive index of air and other gases at 248 nm", Optics Communications, **103**, 153 (1993).

[8] E. T. J. Nibbering, G. Grillon, M. A. Franco, B. S. Prade, and A. Mysyrowicz, "Determination of the intertial contribution to the nonlinear refractive index of air, N_2, and O_2 by

use of unfocused high-intensity femtosecond laser pulses", Journal of the Optical Society of America B, **14**, 650 (1997).

[9] J. K. Wahlstrand, Y. H. Cheng, and H. M. Milchberg, "Absolute measurement of the transient optical nonlinearity in N_2, O_2, N_2O, and Ar", Physical Review A, **85**, 043820 (2012).

[10] Z. Zahedpour, J. K. Walstrand, and H. M. Milchberg, "Measurement of the nonlinear refractive index of air constituents at mid-infrared wavelengths", Optics Letters, **40**, 5794 (2014).

[11] J. J. Lehmeier, W. Leupacher, and A. Penzkofer, "Nonresonant third order hyperpolarizability of rare gases and N_2 determined by third harmonic generation", Optics Communications, **56**, 67 (1985).

[12] W. G. Rado, "The nonlinear third order dielectric susceptibility of gases and optical third harmonic generation", Applied Physics Letters, **11**, 123 (1967).

[13] Y. Kitigawa, R. L. Savage, Jr., and C. Joshi, "Demonstration of collisionally enhanced degenerate four-wave mixing in a plasma", Physical Review Letters, **62**, 151 (1989).

[14] M. Sheik-Bahae, A. A. Said, T. Wei, D. J. Hagan, and E. W. Van Stryland, "Sensitive measurement of optical nonlinearities using a single beam", IEEE Journal of Quantum Electronics, **26**, 760 (1990).

[15] V. G. Dmitriev, G. G. Guzadyan, and D. N. Nikogosyan, *Handbook of Nonlinear Optical Crystals*, Springer, New York (1999).

[16] C. V. Filip, R. Narang, S. Ya. Tochitsky, C. E. Clayton, and C. Joshi, "Optical Kerr switching technique for the production of picosecond, multiwavelength CO_2 laser pulse", Applied Optics, **41**, 18, 3743-3747 (2002).

[17] J. K. Wahlstrand, Y.-H. Cheng, and H. M. Milchberg, "High Field Optical Nonlinearity and the Kramer-Kronig Relations", Physical Review Letters **109**, 113904 (2012).

[18] A. Taleki, E. M. Wright, and M. Kolesik, "Microscopic model for the higher-order nonlinearity in optical filaments", Physical Review A, **82**, 065801 (2010).

[19] C. Brée, A. Demircan, and G. Steinmeyer, "Saturation of the All-Optical Kerr Effect", Physical Review Letters, **106**, 183902 (2011).

[20] E. E. Serebryannikov and A. M. Zheltikov, "Quantum and Semiclassical Physics behind Ultrafast Optical Nonlinearity in the Midinfrared: The Role of Ionization Dynamics within the Field Half Cycle", Physical Review Letters, **113**, 043901 (2014).

[21] K. Schuh, J. V. Moloney, and S. W. Koch, "Interaction-induced nonlinear refractive-index reduction of gases in the midinfrared regime", Physical Review E, **93**, 013208 (2016).

[22] P. Whalen, P. Panagiotopoulos, M. Kolesik, and J. V. Moloney, "Extreme carrier shocking of intense long-wavelength pulses", Physical Review A, **89**, 023850 (2014).

Chapter 5

Supercontinuum generation from 2 – 20 μm in GaAs pumped by 3 ps CO_2 laser pulses

Section 5.1: Introduction to mid-IR supercontinuum generation

Supercontinuum (SC) generation involves the production of coherent, white-light via a combination of nonlinear optical processes. The bandwidth of the white-light is such that $\Delta v / v_0$ approaches unity where Δv is the bandwidth of the radiation and v_0 is the carrier frequency. Such light may be spatially coherent, spectrally coherent or both and is typically generated through a combination of nonlinear optical effects such as self-phase modulation (SPM), self-focusing, stimulated Raman scattering (SRS), and four-wave mixing (FWM) [1, 2].

The broadest SC are generated in media that exhibit group velocity dispersion (GVD) and a nonlinear response that are opposite in sign because this creates a condition in which a pulse will become self-compressed as its spectrum is broadened via SPM, as was discussed in section 2.4 of Chapter 2. For conventional, self-focusing nonlinearities this is accomplished by propagating a pulse in the negative GVD region of a material. Alternatively, the self-defocusing nonlinearities attainable by cascaded quadratic processes can be used to generate SC in crystals that exhibit positive GVD [3].

The vast majority of SC generation experiments have been performed using self-focusing nonlinearities pumped by near-IR lasers. Since all near-IR materials have positive GVD, the waveguide properties of optical fibers are used to shift the materials' zero dispersion wavelength toward shorter wavelengths thus ensuring that the pump pulse propagates in the negative GVD regime [1, 2]. Here, broadband SC spectra have been generated using nanosecond [4], picosecond [5] and femtosecond [6] pulses propagating in micro-structured or tapered fibers.

Although the use of a near-IR pump limits the long-wavelength extent of the SC, spectra extending to ≤ 5 µm have been realized using fluoride [4] and chalcogenide [6] IR fibers.

Applications would benefit from extending SC sources to longer wavelengths. The region from $2 - 20$ µm is of particular importance since all simple molecules have a fundamental rotational-vibrational bands in this range. By pumping chalcogenide fibers with mid-IR (4.5 µm) pulses researchers have shown SC generation from $1.4 - 13.3$ µm [7]. However, chalcogenide fibers are difficult to create and have a complicated transmission spectrum. Bulk semiconductors such as GaAs and CdTe have a spectrally flat transmission curve in the mid-IR region, exhibit low optical loss, are available in large sizes, and possess nonlinearities $\sim 1000x$ that of silica making them excellent candidates for SC generation. However, the optimal pump for these materials is in the range of $7 - 10$ µm range where high-power lasers are scarce.

A picosecond CO_2 laser provides a means to study SC generation in bulk semiconductors. Before now there has only been one reported experiment where a SC spectrum from 3 to 14 µm was generated in GaAs pumped by intense CO_2 laser pulses [8]. Here researchers used tightly focused, 600 µJ, 9.3 µm pulses at an intensity of 10^{11} W/cm^2. These pulse parameters resulted in an exponentially decaying, SC spectrum characteristic of SPM rather than the plateu-shaped SC spectrum characteristic of SC experiments in fibers that rely on a combination of SPM, SRS and FWM. In this chapter we will present an experiment on the generation of SC from $2 - 20$ µm in GaAs crystals pumped by 20 mJ, 3 ps CO_2 laser pulses centered at 10.6 µm [9]. In doing so we will identify and study a regime of SC generation that is dominated by FWM, SRS and modulational instability, similar to experiments in near-IR pumped fibers. Finally, it should be mentioned that a similar SC generation mechanism in GaAs using 150 fs, 2 µJ, 8 µm pulses has been recently reported [10].

Section 5.2: Measurements of mid-IR supercontinuum generation in GaAs pumped by 3 ps CO_2 laser pulses

Figure 5.1a depicts the experimental set-up used to measure the mid-IR SC spectrum and temporal pulse profile of the laser pulses used in the experiment. For this experiment we have used 20 mJ, 3 ps CO_2 laser pulse trains that are described in detail in Chapter 3 of this dissertation. These pulses were focused to a peak intensity of 10^{10} W/cm^2 and sent through various lengths of AR-coated GaAs crystals. Note that semi-insulating, Cr-doped GaAs crystals possessing extremely low optical loss were used for this experiment. The small reflection from the AR-coatings was monitored using a HgCdTe detector to account for shot-to-shot fluctuations of the laser system. After the GaAs crystal the spectrum of the output radiation was measured using a scanning monochromator and a cryogenically cooled HgCdTe detector. The temporal pulse format of the IR radiation was measured using a picosecond streak camera. In order to realize temporal measurements with a streak camera, the pulse profile of the IR radiation was converted to visible light by co-propagating a diode laser with the IR radiation in a CS_2 filled Kerr cell [11]. A representative measurement of the CO_2 laser pulse train without propagation through GaAs is shown in Fig. 5.1b.

To understand the evolution of the SC spectrum we studied SC generation in 2, 30 and 67 mm long GaAs crystals. We did not observe significant spectral broadening in the 2 mm sample but the 30 mm GaAs crystal produced a SC spectrum from $2 - 20$ μm as shown in Fig. 5.2. Here each point on the plot in Fig. 5.2 was obtained by averaging three laser shots of comparable input energy. The spectrum shown in Fig. 5.2 has a bandwidth of ~ 135 THz and is limited by the transmission of the material [12]. As can be seen in Fig. 5.2, the SC spectrum has three peaks identified with third harmonic generation (THG), second harmonic generation (SHG) and SRS

near 3.5, 5.3 and 16 μm respectively. The 16 μm feature is consistent with the 8.55 THz Raman

shift in GaAs [13].

Figure 5.3 shows the SC spectrum generated in 67 mm of GaAs. In this case, the spectrum

features a long-wavelength plateau that extents from 12 – 20 μm. We have also observed an

order of magnitude greater yield than was observed in the 30 mm case of Fig. 5.2. The spectrum

was more modulated than in the 30 mm case and contains a measurable Raman anti-Stokes peak

near 8 μm.
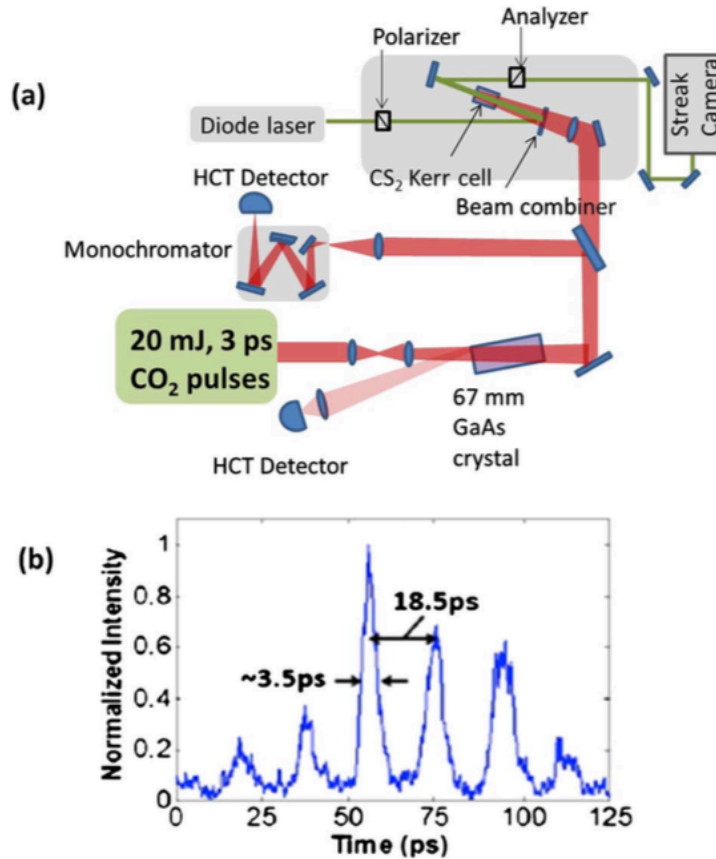
Figure 5.1: (a) Simplified experimental set-up for supercontinuum generation. HCT stands for

HgCdTe. (b) Representative temporal pulse format used for SC generation.

Figure 5.4 summarizes the results of temporal measurements of the laser pulses after the GaAs crystal. Figure 5.4a shows the temporal pulse format observed for the 2 and 30 mm case. For these lengths of GaAs, we did not observe any significant changes in the temporal pulse format. Figure 5.4b depicts temporal measurements after the 67 mm crystal. In this case, although the pulse train retains its original 18.5 ps modulation, each individual pulse has broken into a series of sub-pulses. These sub-pulses were measured to be ~ 1.5 ps long, limited by the time resolution of the streak camera and the nonlinear response of the CS_2 Kerr cell.
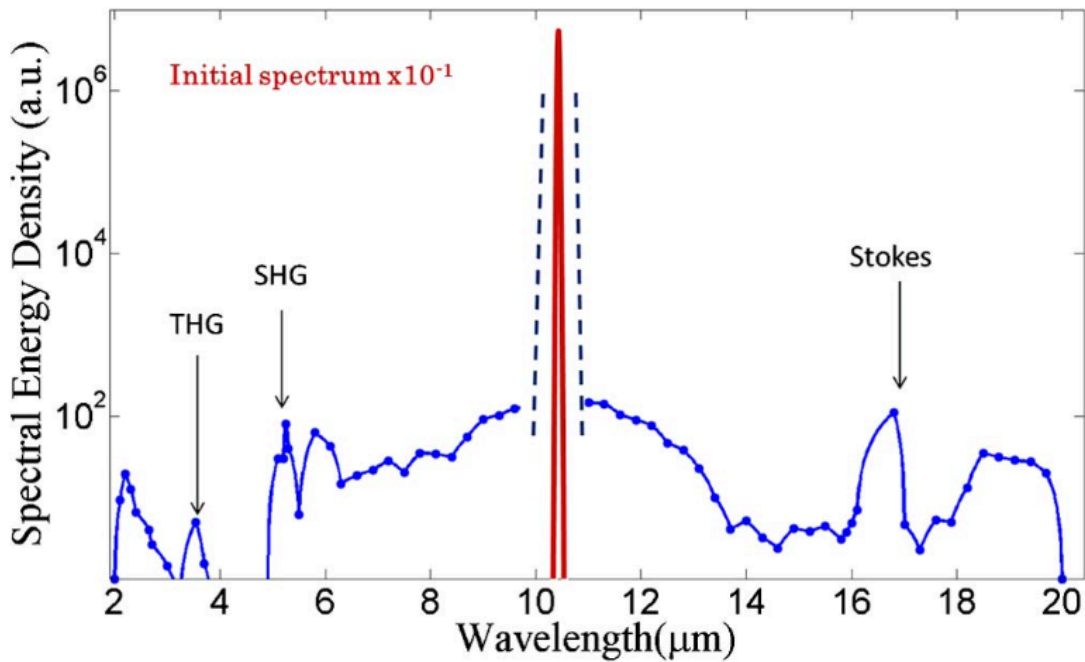
Figure 5.2: SC spectrum measured after 30 mm of GaAs. SHG and THG stand for second harmonic generation and third harmonic generation, respectively.

The observed pulse splitting in the negative GVD regime can occur from modulational instability (MI), soliton fission (SF) or a combination of both [14]. According to numerical simulations presented in [2], nonlinear optical interactions with soliton orders less than ~ 16 tend

to be dominated by SF while soliton orders greater than ~ 16 lead to MI. The soliton order can be calculated using $N^2 = L_D/L_{NL}$, as defined in section 2.4 of Chapter 2. For our experimental conditions we have calculated a soliton order of ~ 45, suggesting that this SC is dominated by MI. Since the MI is seeded from noise, this suggests that the SC generated in this experiment is spectrally incoherent. In general, additional measurements of the coherence of the SC radiation is needed to determine whether MI or SF dominates the observed behavior.

We have also studied SC generation in 134 mm of GaAs by arranging two 67 mm crystals in tandem. For this configuration we observed a very similar spectrum as was shown in Fig. 5.3 and did not observe any substantial increase in the yield of the long-wavelength section of the plateau. These observations indicate that the SC process is likely terminated shortly after 67 mm of propagation distance.
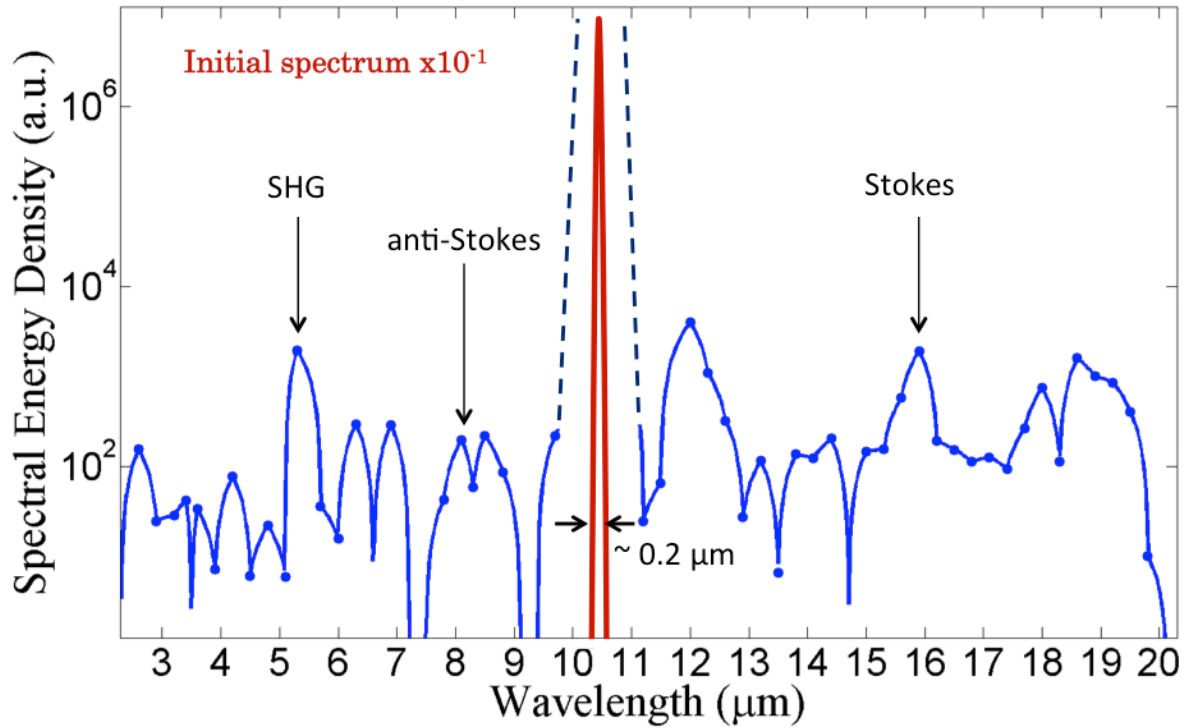
Figure 5.3: SC spectrum measured after 67 mm of GaAs. SHG and THG stand for second harmonic generation and third harmonic generation, respectively. Note that the width of the initial spectrum of a 3 ps, 10.6 µm pulse at the 10^{-6} level is ~0.2 µm.

We have estimated the efficiency of the SC generation process in GaAs by using narrow band pass filter centered at 12.1 µm. For the 67 mm case the yield is approximately 10^{-5} relative to the carrier. Despite this low conversion efficiency, we estimate the SC spectrum has a spectral energy density of 200 pJ nm^{-1} – 2 nJ nm^{-1}, that is comparable with the high spectral energy densities characteristic of SC generation via laser filamentation in a bulk crystal [15].
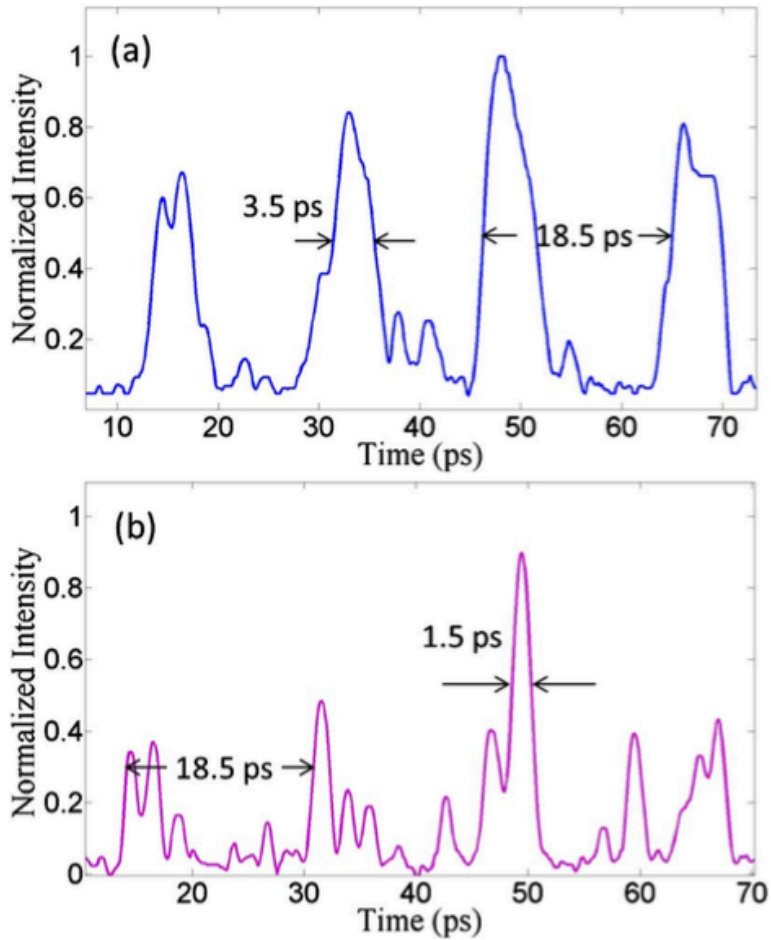
Figure 5.4: (a) Input temporal pulse profile zoomed in the vicinity of maximum peak power. (b) Temporal pulse profile after propagating through 67 mm of GaAs.

Section 5.3: Simulations of mid-IR supercontinuum generation in GaAs using the Generalized Nonlinear Schrödinger Equation

We have modeled the SC generation process in GaAs by numerically solving the one dimensional Generalized Nonlinear Schrödinger Equation (GNLSE) that was defined by Eq. 2.41 of Chapter 2. In doing so, we have modeled the propagation a 3 ps pulse train, similar to the one used in the experiment. Plots of the spectrum and temporal pulse profile of the numerical 3

ps pulse train can be seen in Fig. 5.5a and 5.5b, respectively. For the dispersion of GaAs we have used the measurements reported in reference [12] and have included up to the eighth term of the Taylor series approximation of the dispersion relation in order to match the long-wavelength portion of the SC spectrum. For the nonlinear index of GaAs we have used $n_2 = 0.6$ x 10^{-13} cm^2/W, similar to the value measured by the four-wave mixing experiment described in section 4.5 of Chapter 4. To include SRS we have modeled the Raman response as an exponentially decaying sinusoid of frequency 8.55 THz and a bandwidth of ~ 100 GHz, to match the Raman fluorescence measurements [13]. Figure 2.4 of chapter 2 depicts the time- and frequency-domain representation of the Raman response used for these simulations. Finally, a stochastic amount of noise with a standard deviation equal to the square root of the photon number in one temporal discretization bin was included as prescribed in [2]. This noise is necessary to observe MI in the numerical simulations, as will be shown below.
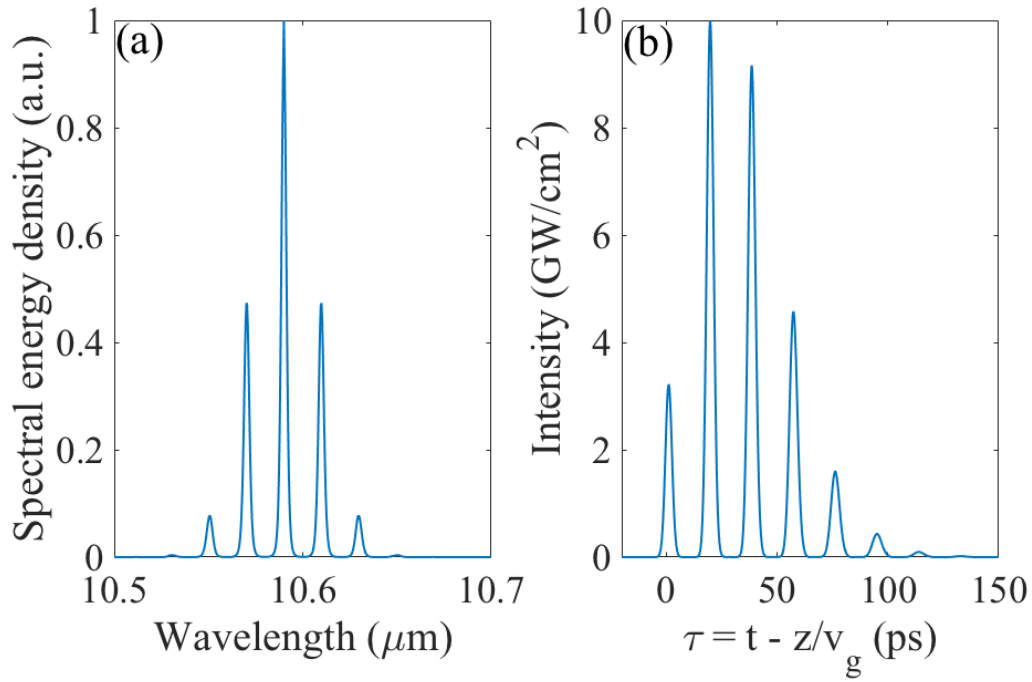
Figure 5.5: (a) Input spectrum used for SC simulations. (b) Input temporal pulse profile used for SC generation simulations.

Figure 5.6a and 5.6b show the simulated spectrum and temporal pulse profile after propagating through 67 mm of GaAs. The spectrum is broadened to 45 THz or from 5 to 20 μm and is qualitatively similar to the measured SC spectrum depicted in Fig. 5.3. The simulations also predict the pulse break-up via MI as can be seen in Fig. 5.6b. It should be noted that we have zoomed the time-domain figures in the vicinity of maximum peak power.
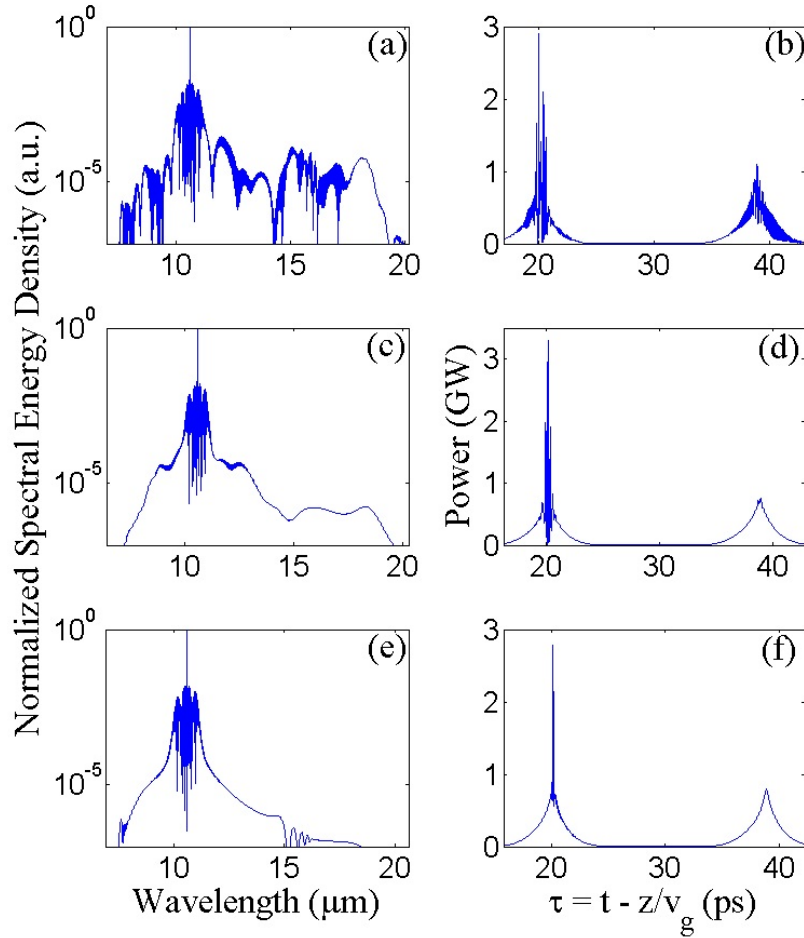
Figure 5.6: (a), (c), and (e) are simulated SC spectra and (b), (d), and (f) are simulated temporal pulse profiles in the vicinity of the two most intense pulses after propagating through 67 mm of GaAs. (c) and (d) represent results obtained with SRS disabled. (c) and (f) are results obtained without noise.

To understand the effect of SRS on SC generation in GaAs we have performed simulations with SRS disabled. Figure 5.6c and 5.6d show the simulated spectrum and temporal pulse profile after 67 mm of GaAs with SRS disabled. As can be seen in the figure, SRS increases the yield on the long wavelength plateau by as much as two orders of magnitude. In the time-domain, disabling SRS has manifested in less temporal pulse splitting from MI, as can be seen in Fig.

77

5.6d. It should be noted that SRS has been identified as a major mechanism for inducing MI and SF in SC experiments in fibers [2].

Finally, to analyze the effect of MI on the SC spectrum we have performed simulations without the inclusion of stochastic noise. Figures 5.6e and 5.6f depict the simulated spectrum and temporal pulse profiles after propagating 67 mm in GaAs without noise. As can be seen in Fig. 5.6e, the yield of the long-wavelength part of the SC spectrum has decreased even further than the result depicted in Fig. 5.6d, with SRS disabled. In addition, the total extent of the SC spectrum has also been greatly diminished without noise. In the time-domain, shown in Fig. 5.6e, it is clear that MI has been completely disabled without the inclusion of noise. Instead, the most intense pulse has been compressed, without splitting. Similar to near-IR experiments in fibers, it is the action of pulse splitting that causes such broadband light to be generated in the SC generation process.

The major discrepancies between the experimental and simulated spectra are on the high-frequency side of the SC spectrum. This arises because we have used an envelope model that is unable to account for harmonic generation. Another significant limitation is that this model does not include second order nonlinear effects, such as second harmonic generation and cascaded quadratic nonlinearities. These effects certainly play a role in this experiment, evident by the large SHG peak in the experimental spectrum of Fig. 5.3. Three-wave mixing processes governed by the second-order nonlinearity may be responsible for the additional features shown in the experimental spectrum. Finally, there is a discrepancy between the simulated and experimental temporal pulse profile measurements. In the experiment, there are sub-pulses that appear between the 18.5 picosecond separations of the CO_2 pulse train that are absent in the simulated temporal pulse profiles. This discrepancy may occur because we have neglected

spatial effects such as self-focusing. Indeed, self-focusing can cause additional pulse splitting even in media with positive GVD [16].

To benchmark these simulations, we have also simulated SC generation using the pulse parameters used by Corkum, *et. al.* [8]. Figure 5.7a depicts the experimental spectrum obtained in 6 cm of GaAs when 2.5 ps, 9.3 µm CO_2 laser pulses were focused to a peak intensity of 10^{11} W/cm^2 and Fig. 5.7b shows the simulated SC spectrum using the GNLSE. As can be seen in the figure, the calculation qualitatively predicts the shape and extent of the SC, except for the high-frequency components generated via harmonic generation. The main difference in SC spectrum obtained using 10.6 and 9.3 µm pulses is attributed to the change in the GVD. Since GaAs is less dispersive at 9.3 µm, the pulses do not have a sufficient length to undergo MI resulting in a narrower SC spectrum, as can be seen in Fig. 5.7. Although, 1-D simulations using the GNLSE are able to qualitatively predict the shape of the SC spectrum, more detailed calculations including harmonic generation, self-focusing, second order nonlinearities and optical field ionization are required to quantitatively predict the outcome of experiments.
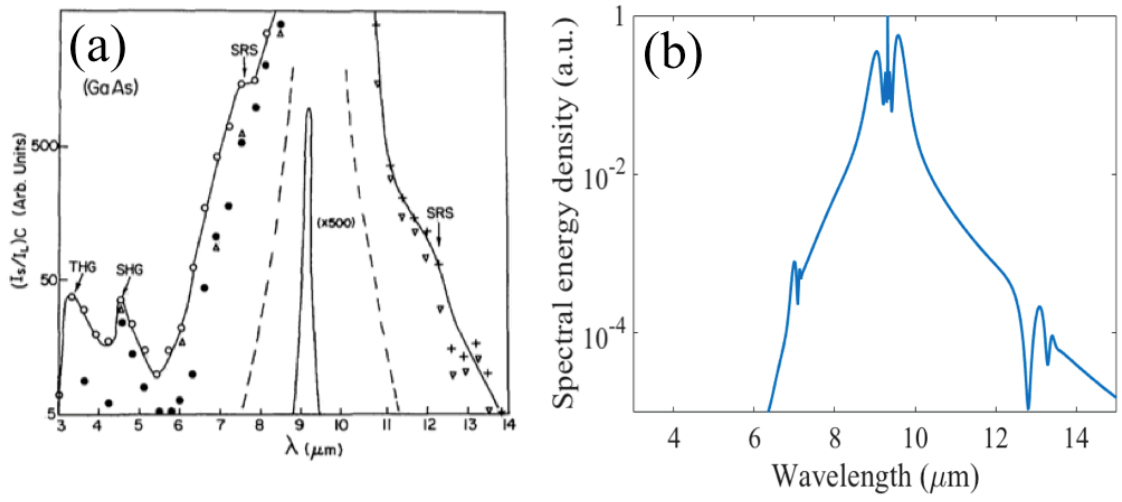
Figure 5.7: (a) Experimental SC spectrum obtained in a 6 cm GaAs crystal pumped by 9.3 μm, 2.5 ps and 8 ps CO_2 laser pulses from reference [8]. The open circles correspond to data taken with 2.5 ps pulses at full power, the open triangles are 2.5 ps pulses with half power, the closed circles are 8 ps pulses with full power, the crosses are 8 ps pulses with half power and the upside down triangles are 8 ps pulses with quarter power. (b) Simulated SC spectrum using 9.3 μm pulses with a 2.5 ps pulse duration as described in reference [8].

References

[1] R.R. Alfano, *The Supercontinuum Laser Source*. Springer, New York (2006)

[2] J.M. Dudley, G. Genty and S. Coen. "Supercontinuum generation in photonic crystal fiber." Reviews of Modern Physics, **78** (2006).

[3] M. Bache, H. Guo, and Binbin Zhou, "Generating mid-IR octave-spanning supercontinua and few-cycle pulses with solitons in phase-mismatched quadratic nonlinear crystals", Optical Materials Express, **3**, 10 (2013).

[4] C. Xia, M. Kumar, O. P. Kulkarni, M. N. Islam, and F. L. Terry, Jr., "Mid-infrared supercontinuum generation to 4.5 μm in ZBLAN fluoride fibers by nanosecond diode pumping", Optics Letters, **31**, 17 (2006).

[5] S. Coen, A. H. L. Chau, R. Leonhardt, J. D. Harvey, J. C. Knight, W. J. Wadsworth, and P. St. J. Russel, "White-light supercontinuum generation with 60-ps pump pulses in a photonic crystal fiber", Optics Letters, **26**, 17 (2001).

 [6] C. W. Rudy, A. Marandi, K. L. Vodopyanov, and R. L. Byer, "Octave-spanning supercontinuum generation in *in situ* tapered As_2S_3 fiber pumped by a thulium-doped fiber laser", Optics Letters, **38**, 15 (2013).

[7] C. R. Petersen, U. Møller, I. Kubat, B. Zhou, S. Dupont, J. Ramsay, T. Benson, S. Sujecki, N. Abdel-Moneim, Z. Tang, D. Furniss, A. Seddon, and O. Bang, "Mid-infrared supercontinuum covering 1.4-13.3 μm molecular fingerprint region using ultra-high NA chalcogenide step-index fibre", Nature Photonics , **8**, 830-834 (2014).

[8] P.B. Corkum, P.P. Ho, R.R. Alfano, and J.T. Manassah. "Generation of infrared supercontinuum covering 3-14 μm in dielectrics and semiconductors." Optics Letters, 1-**10**, 12 (1985).

[9] J. J. Pigeon, S. Ya. Tochitsky, C. Gong, and C. Joshi, "Supercontinuum generation from 2 – 20 μm in GaAs puped by picosecond CO_2 laser pulses", Optics Letters, **39**, 12 (2014).

[10] A. A. Lanin, A. Voronin, E. A. Stepanov, A. B. Fedotov, and A. M. Zheltikov, "Multioctave, 3 – 18 μm sub-two-cycle supercontinua from self-compressing, self-focusing soliton transients in a solid", Optics Letters, **40**, 6 (2015).

[11] C. V. Filip, R. Narang, S. Ya. Tochitsky, C. E. Clayton, and C. Joshi, "Optical Kerr switching technique for the production of a picosecond, multiwavelength CO_2 laser pulse", Applied Optics, **41**, 18 (2002).

[12] C. J. Johnson, G. H. Sherman, and R. Weil, "Far Infrared Measurement of the Dielectric Properties of GaAs and CdTe at 300 K and 8 K", Applied Optics, **8**, 8 (1969).

[13] A. M. Ardila, O. Martínez, M. Avella, J Jiménez, B. Gérard, J. Napierala, and E. Gil-Lafon, "Temperature dependence of the Raman shift in GaAs conformal layers grown by hydride vapor phase epitaxy", Journal of Applied Physics, **91**, 8 (2002).

[14] A. Demircan, U. Bandelow, "Analysis of the interplay between soliton fission and modulational instability in supercontinuum generation", Applied Physics B, **86**, 31-39 (2007).

[15] F. Silva, D. R. Austin, A. Thai, M. Baudisch, M. Hemmer, D. Faccio, A. Couairon, and J. Biegert, "Multi-octave supercontinuum generation from mid-infrared filamentation in a bulk crystal", Nature Communications, **3**, 807 (2012).

[16] J. K. Ranka, R. W. Schirmer, and A. L. Gaeta, "Observation of Pulse Splitting in Nonlinear Dispersive Media", Physical Review Letters, **77**, 18 (1996).

Chapter 6

Broadband four-wave mixing compression of a 200 ps CO_2 laser beat-wave in GaAs

Section 6.1: Multiple four-wave mixing compression as a method to produce high-power, picosecond pulses in the mid-IR

In the previous chapter we have shown that supercontinuum generation in the molecular fingerprint region is one application for GW-class, picosecond pulses with a wavelength near 10 μm. It is still challenging, however, to produce high-power, picosecond pulses in this spectral range. Indeed, picosecond CO_2 laser systems are complicated in that they require a broadband solid-state laser front-end and high-pressure CO_2 lasers for picosecond amplification, as was discussed in Chapter 3.

In this chapter, we present an experiment in which we test an idea of compressing the approximately 1 ns long pulses available from common TEA CO_2 lasers to a train of picosecond pulses using nonlinear optics. In the previous chapters of this thesis, we have considered four-wave mixing (FWM) in which only two sidebands are generated. For this chapter we will rely on so-called multiple FWM, in which many sidebands are generated. The bandwidth generated by the multiple FWM of a CO_2 laser beat-wave, if compressed, can result in the reduction of the initial beat-period to ultrafast time scales. This technique of multiple FWM compression has been used to convert CW light at a wavelength of 1.5 μm to trains of $0.1 - 1$ ps pulses in fibers with negative GVD [1-3]. In this chapter, we will explore this technique using 200 ps CO_2 laser beat-waves similar to the pulse format used for the nonlinear index measurements detailed in

Chapter 4. One of the possible applications of such a source can be the generation of broadband radiation from $8 - 14$ μm as was studied theoretically by Kapetanakos *et. al.* [4].

Section 6.2: Multiple four-wave mixing compression in GaAs and NaCl crystals using 106 GHz, CO_2 laser beat-waves

Experiments were carried out using the 200 ps pulses produced by the Neptune laboratory's MOPA system, as described in Chapter 3. For this experiment 106 GHz beat-waves were produced by mixing radiation produced on the 10P20 (10.59 μm) line with radiation produced on the 10P16 (10.55 μm). Both CO_2 laser lines were amplified synchronously in a bifurcated CO_2 laser cavity with independent control of the gain to loss ratio for each wavelength (see Chapter 3 for more information).

Figure 6.1a shows the general scheme of this experiment, where a dual-frequency beat-wave is transformed into a manifold of sidebands in a cubic nonlinear medium. Figure 6.1b shows a simplified set-up for measurements of the FWM spectrum and temporal pulse profile after the 150 MW, 106 GHz beat-wave, focused to a peak intensity of ~ 0.75 GW/cm^2, was propagated through GaAs and NaCl crystals of various lengths. It should be noted that NaCl was used as a pulse compressor in this experiment since it has a similar negative GVD as GaAs but has 1000x less nonlinearity. After the crystals we have measured the FWM spectrum using two diagnostics. The first was a single-shot spectrometer employing a pyroelectric camera as a detector, a typical FWM spectrum showing the first two red-shifted sidebands can be seen as the left inset of Fig. 6.1b. Here, the use of a pyroelectric camera allowed for a calibration of the side-band yield on an absolute scale. The second spectral diagnostic comprised of a scanning monochromator and a cryogenically cooled HgCdTe and was used to perform high-resolution measurements of the

FWM spectrum. Finally, measurements of the temporal pulse profile were accomplished using a picosecond streak camera, as described in chapter 5.
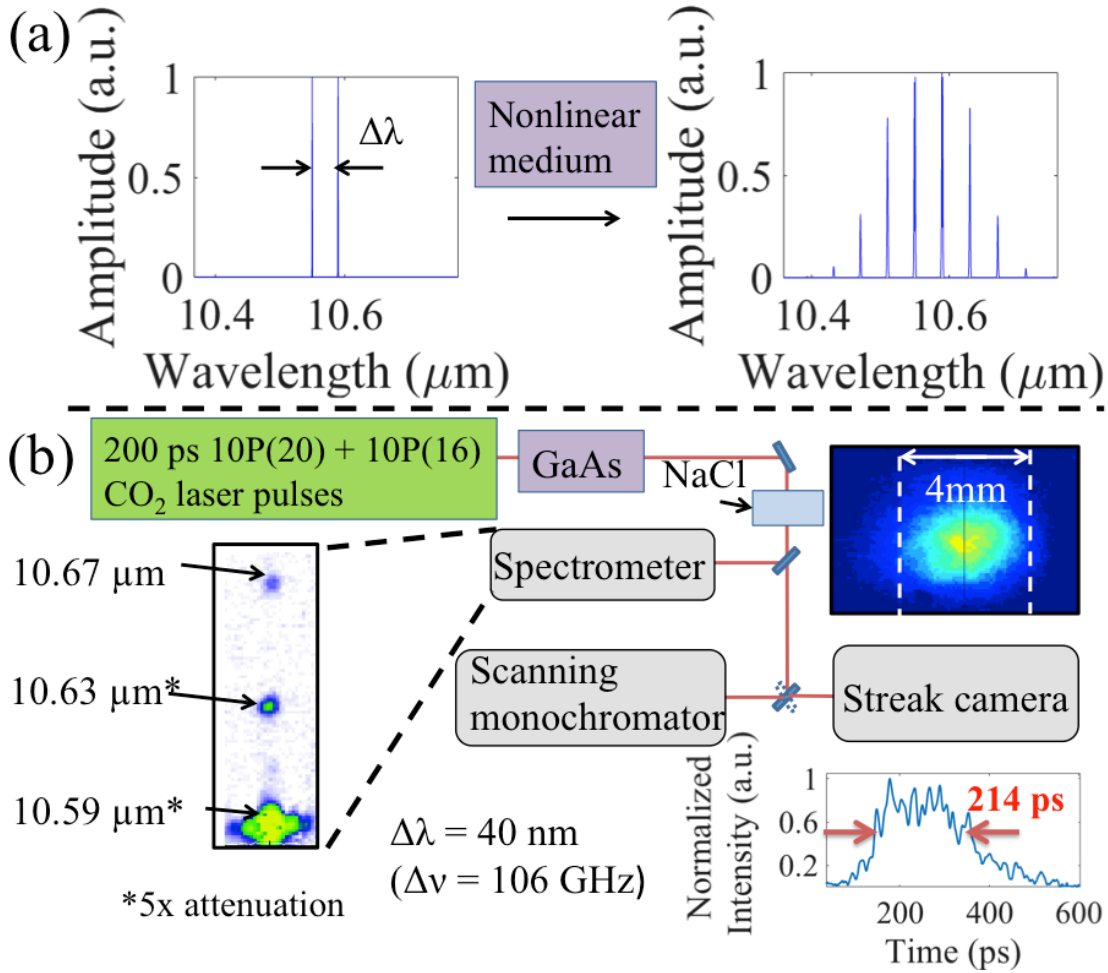
Figure 6.1: (a) A dual-frequency beat-wave is transformed into a family of sidebands after propagation through a nonlinear medium. (b) Simplified experimental set-up to measure the spectral and temporal profiles of CO_2 laser beat-waves after multiple four-wave mixing in GaAs followed by compression in NaCl. The inset is a measurement of the spatial profile of the beam measured with a pyroelectric camera.

We have simulated FWM and compression in GaAs and NaCl by numerically solving the 1-D, Generalized Nonlinear Schrödinger Equation (GNLSE), introduced in section 2.6 of Chapter 2. Spatial effects, free-carrier formation from optical field ionization, harmonic generation, and second order effects were neglected in this model. Due to these limitations we have used the nonlinear index as a fitting parameter, using $n_2 = 0.9$ x10^{-13} cm^2/W, similar to the value obtained from FWM measurements and presented in section 4.5 of Chapter 4. As was the case in the previous chapter, we have used the dispersion relation measured by Johnson, *et. al.* [5] and have modeled the Raman response as an exponentially decaying sinusoid with a frequency of 8.55 THz and a bandwidth of ~ 100 GHz, consistent with the Raman fluorescence measurements of reference [6]. (See Chapter 2, section 2.5 for detailed information on the Raman response of GaAs).

We first studied FWM mixing and compression in 67, 134 and 268 mm of GaAs. In doing so we have used two 67 mm long Cr-doped GaAs crystals in tandem to study 134 mm of nonlinear propagation length and in a double-pass configuration to study 268 mm. We have observed a significantly broadened FWM spectrum after propagation through GaAs as can be seen in Fig. 6.2. The vertical lines shown on Fig. 6.2 represent the maximum amplitude of the side-bands as measured with the monochromator. We have also produced simulated FWM spectra for these lengths by solving the GNLSE for our experimental parameters. As can be seen in Fig. 6.2b, the FWM spectrum reached a maximum bandwidth of 1.76 THz after 134 mm of GaAs. We observed a saturation of the spectral broadening as scaling the interaction length to 268 mm did not produce additional bandwidth, as could be seen in Fig. 6.2c.
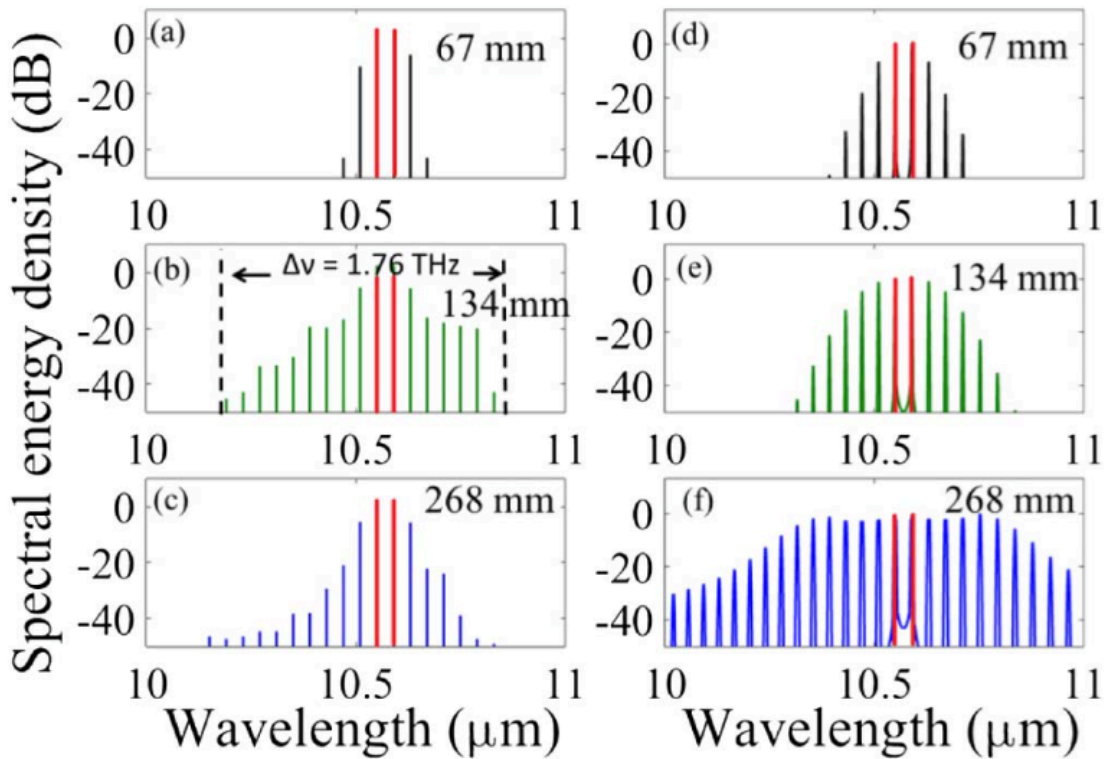
Figure 6.2: Experimentally measured FWM spectra (a), (b) and (c) and the simulated FWM spectra (e), (f), (g) after passage of the 106 GHz beat-wave through various lengths of GaAs, as indicated on the figures. The initial pump wavelengths are shown in red.

We have also measured the temporal pulse profiles corresponding to nonlinear propagation in 67, 134 and 268 mm of GaAs. Figure 6.3 depicts the results of these measurements. Here, there is an approximately 9 ps modulation corresponding to the 106 GHz beat-frequency for all cases. After propagation in the nonlinear medium, however, the pulses are compressed by the combined action of FWM and the negative GVD of GaAs. To analyze this pulse compression we have presented the average and the standard deviation of the FWHM pulse length, obtained by fitting $5 - 10$ pulses from the same train with a $sech^2$ shape. In doing so, it was necessary to correct for the finite temporal resolution of the streak camera and for the rotational response time of the CS_2

Kerr cell. The presented pulse lengths are obtained by $\tau^2 = \tau_{Meas}^2 - \tau_r^2 - \tau_{ins}^2$, where τ_{Meas} is

the measured pulse length, $\tau_r \sim 1$ ps is the rotational response of CS_2 and $\tau_{ins} \sim 1.5$ ps is the

temporal resolution of the streak camera. These measurements indicate that the pulses are

compressed from an average pulse length of 5.7 to 2.3 ps in 268 mm of GaAs, as shown on Fig.

6.3. It should be noted that the temporal profile after 67 mm of GaAs (see Fig. 6.2a) was

indistinguishable from the temporal profile without propagation in a nonlinear medium. We have

also shown the simulated temporal pulse profiles for the same lengths, shown in Fig. 6.3d, 6.3e

and 6.3f for comparison.
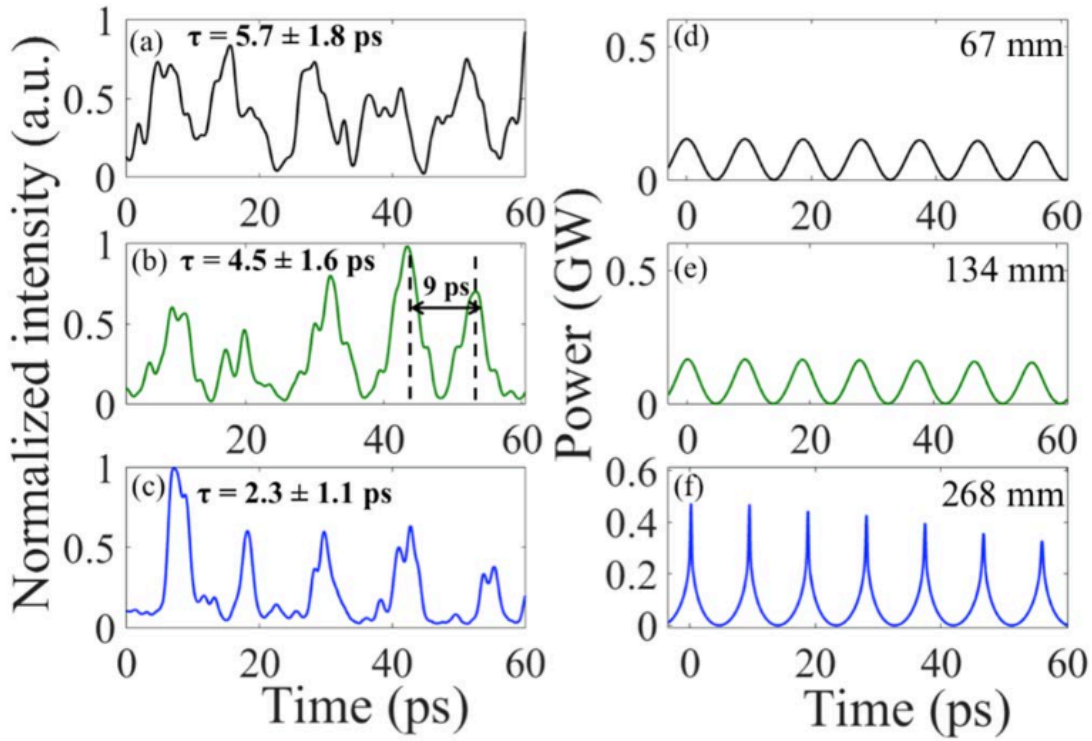
Figure 6.3: Experimentally measured temporal pulse profiles measured after nonlinear

propagation in (a) 67, (b) 134 and (c) 268 mm of GaAs. Simulated temporal pulse profiles

corresponding to propagation in (e) 67, (f) 134, and (g) 268 mm of GaAs.

The simulation results presented in Fig. 6.2 and Fig. 6.3 qualitatively match the observed spectral broadening and pulse compression for the 67 and 134 mm propagation lengths. A striking discrepancy between simulation and experiment is observed, however, for the 268 mm case. In the experiment, we have observed saturation in the spectral broadening whereas the simulations predict that this broadening should continue. Similarly, the simulations predict more pulse compression than what is observed in experiment for the 268 mm case. These qualitative discrepancies indicate that there are serious limitations in the 1-D GNLSE model for such large nonlinear phase shifts.

One possible explanation for the discrepancy between simulations and experiment is that two-dimensional effects such as self-focusing may begin to play a role. For these pulse parameters the ratio of P/P_{crit} is approximately 40 and the self-focusing distance (see Eq. 2.23 and 2.24 of Chapter 2) is 220 mm, shorter than the 268 mm interaction length used in the experiment. We have analyzed the beam profile after the 67 and 134 mm of GaAs using magnified images of the laser beam with 20 μm resolution. No signs of self-focusing or beam distortion was observed for these conditions. Spatial measurements for the 268 mm case were not possible because of the double pass configuration. However, tighter focusing of a single-line beam (10.6 μm) – reducing the beam radius by a factor of two – resulted in observable beam distortion after 134 mm of GaAs. For the 268 mm case a possible beam break-up via self-focusing coupled with a meter-scale distance from the GaAs crystal to our spectral diagnostic could manifest in a poor collection for the most broadband components of the FWM spectrum. Another critical limitation of this modeling is the fact that second order processes were not taken into account. Cascaded quadratic processes, such as second harmonic generation (SHG) and difference frequency generation (DFG) can manifest in a reduction of the nonlinearity (see

Appendix D for a detailed description of cascaded quadratic nonlinearities). These cascaded quadratic effects will be discussed in more detail in the next section of this chapter.

Finally, we have carefully optimized this pulse compression scheme in an attempt to obtain short, high-quality pulses. To obtain transform-limited pulses it is necessary to balance the effects of nonlinearity and GVD [1]. To accomplish this we have replaced the last 134 mm of GaAs with a 234 mm long, bulk NaCl pulse compressor ($k_2 = -1645$ fs^2/mm). Figure 6.4 depicts the measured and simulated temporal pulse profiles for this configuration. Here we have produced ~ 1.6 ps pulses, shorter than the 2.3 ps pulses produced with GaAs alone. The transform limited pulses for the FWM spectrum shown in Fig. 6.2b is ~ 1.2 ps.
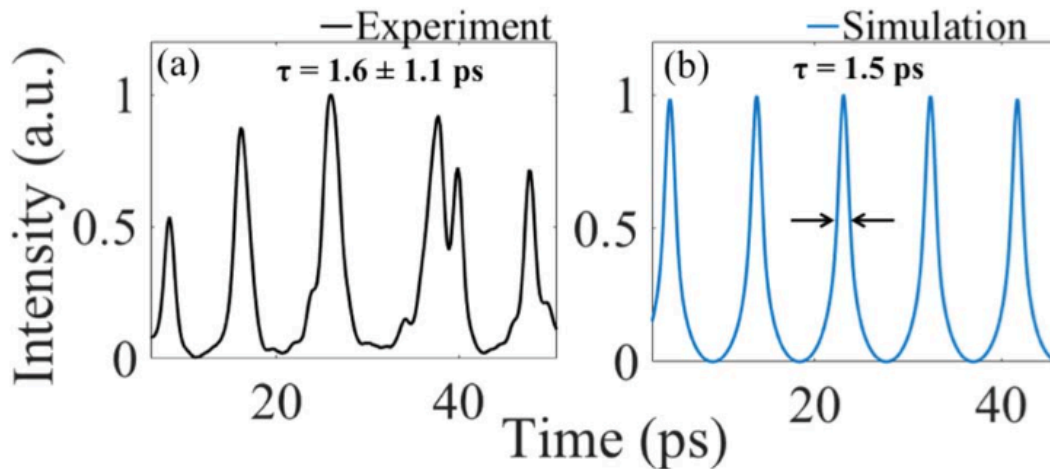
Figure 6.4: (a) Experimental and (b) simulated temporal pulse profiles after the 106 GHz beat-wave propagates through 134 mm of GaAs and 234 mm of NaCl.

Section 6.3: Multiple FWM GaAs crystals using 165 and 882 GHz, CO_2 laser beat-waves and cascaded quadratic difference frequency mixing

In addition to the results presented above, we have also studied multiple FWM using faster beat-frequencies of 165 and 882 GHz obtained by mixing the 10P20 (10.59 μm) line with the 10P14 (10.55 μm) and 10R16 (10.27 μm) lines of the CO_2 laser, respectively. Although the streak camera did not have a sufficient temporal resolution to measure pulse compression we were still able to study how the broadening via FWM changed as a function of beat-frequency.

We have observed significantly less efficient and asymmetric spectral broadening as we increased the beat-frequency. Figure 6.5 shows the experimentally measured FWM spectra for the 882 GHz case obtained by using 7, 30 and 67 mm of GaAs. Interestingly, whereas the 106 GHz FWM spectrum only exhibited strong asymmetry after 268 mm of GaAs (see Fig. 6.2c), the 882 GHz FWM spectrum was asymmetric after just 7 mm of GaAs. It should be noted that the rate at which the FWM spectrum is generated scales as the inverse of the dispersive length [3] $L_D = \frac{\tau_0^2}{|k_2|} = \frac{(2f)^{-2}}{|k_2|}$, where f is the beat-frequency (See Eq. 2.24 of chapter 2), which is why the 882 GHz produced FWM sidebands in a comparatively short GaAs crystal.
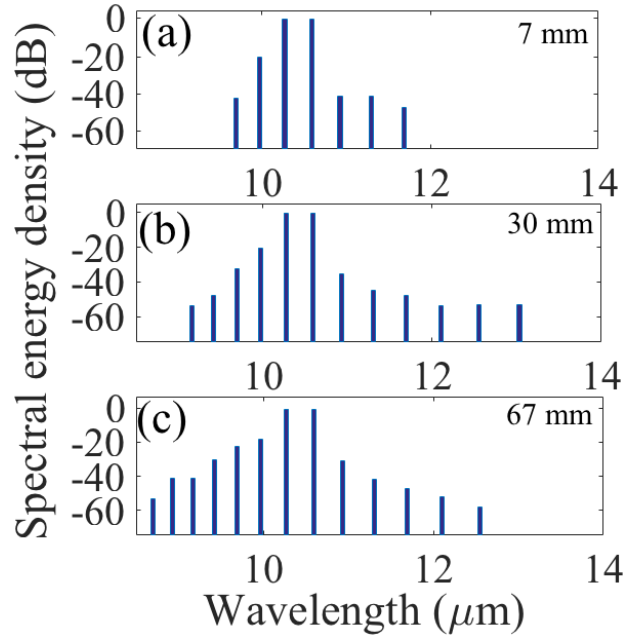
Figure 6.5: Experimentally measured spectra obtained by propagating the 882 GHz beat-wave through (a) 7, (b) 30 and (c) 67 mm of GaAs.

To investigate the observed decrease in FWM efficiency we have simulated the 67 mm case, for which a fair comparison can be made with the 106 GHz case presented in Fig. 6.2a. Figure 6.6 shows a comparison of the experimental (Fig. 6.6a) and simulated (Fig. 6.6b) FWM spectrum. To match the observed spectral broadening we needed to simulate this case with a nonlinear index of 0.5×10^{-13} cm^2/W, a value ~ 40% smaller than the nonlinear index found to match the FWM spectra obtained with the 106 GHz beat-wave.
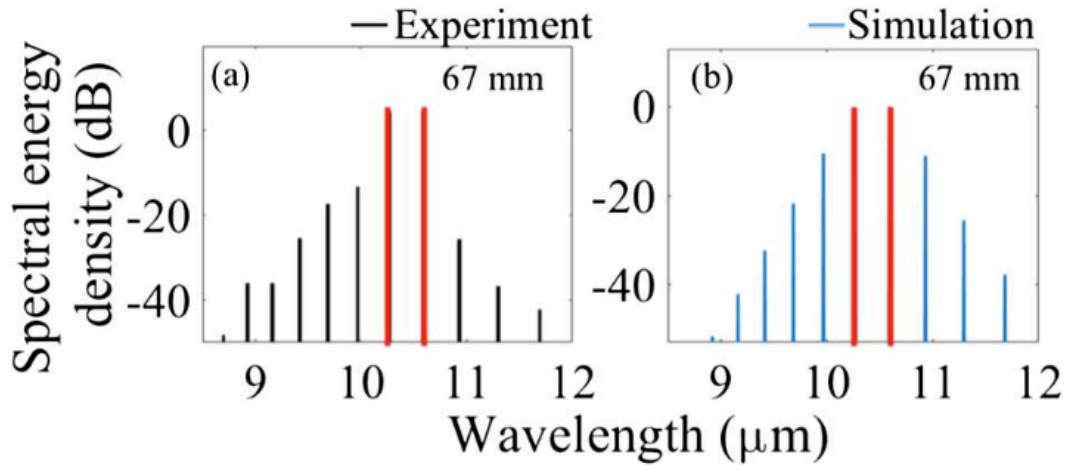
Figure 6.6: Experimentally measured (a) and simulated (b) spectra after the 882 GHz beat-wave propagated through 67 mm of GaAs. The pump wavelengths are colored red.

Quadratic nonlinearities, for which GaAs is known, may be the cause behind these observations. As is discussed in Appendix D, it is now well established that cascaded three-wave mixing can manifest in an effective third-order nonlinearity. The three-wave mixing processes of importance here are SHG and DFG. Analytic estimates (see Eq. D.6 of Appendix D) indicate that SHG may be responsible for decreasing the intrinsic third-order nonlinearity by ~ 10 %. It should be noted that this value may be increased by other sum frequency generation (SFG) processes among the various sidebands. It is unlikely, however, that cascaded SHG and SFG can explain our observation that the nonlinear index decreases as a function of beat-frequency since the linear refractive index does not change rapidly in the range from 10.5 – 10.6 μm or 5.2 – 5.3 μm. The phase-matching condition for the DFG component, however, changes much more rapidly since this frequency is in the vicinity of the phonon-band.

It has been shown that DFG between CO_2 laser lines can be used to generate THz radiation in room temperature GaAs, where the DFG process is phase-matched by the anomalous dispersion of the phonon band [7]. Figure 6.7, taken from Tochitsky *et. al.*, shows the external phase-

matching angle as a function of the DFG wavelength for GaAs. For the 106 GHz beat-wave, the DFG component has a wavelength of 2.8 mm where the phase-mismatch is zero for collinear propagation, as can be inferred from Fig. 6.7. For the 882 GHz beat-wave, however, the DFG wavelength, approximately 340 μm, suffers a finite phase-mismatch for collinear propagation. This phase-mismatch may manifest as an effective third-order nonlinearity according to Eq. D.15 that was derived in Appendix D.

Estimation of the contribution from cascaded DFG using Eq. D.15 of Appendix D shows that this effect can only account for a reduction of the intrinsic third-order nonlinearity by ~ 1%. This number may be increased, however, in the case that there are multiple sidebands since each DFG combination can contribute to the effective nonlinearity. Examination of Eq. D.10 and Eq. D.11 of Appendix D shows that the cascaded contribution should be much more pronounced for the red-shifted side of the FWM spectrum than for the blue-shifted side (see the relevant discussion in Appendix D). This is consistent with our experimental observation that the blue-shifted side of the FWM spectrum was generated with ~ 100x more efficiency than the red (see Fig. 6.6a). The observed asymmetry may also be analogous to the asymmetry observed in cascaded SHG that is caused by large group velocity mismatch between the fundamental field and the SHG component [8]. Nevertheless, this cascaded DFG process, while still not well understood, is likely a universal nonlinear optical phenomenon of mid-IR pumped solids that deserves its own detailed study.
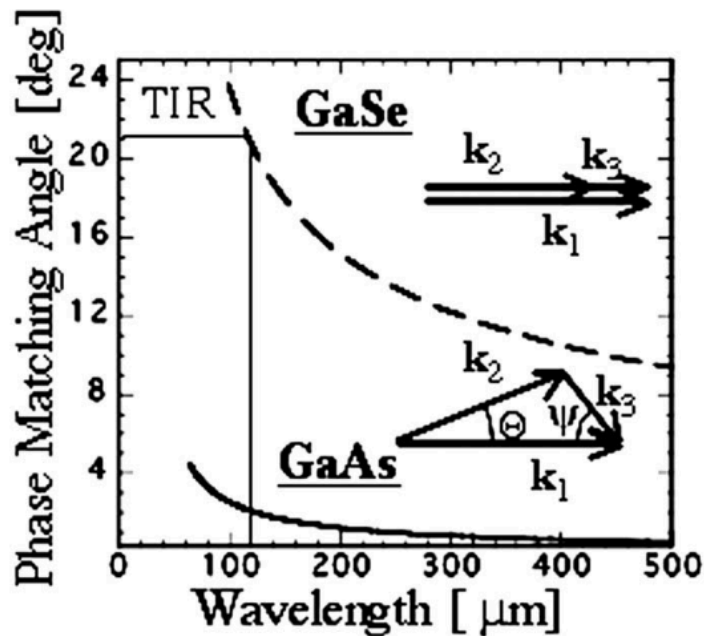
Figure 6.7: External phase-matching angle versus wavelength for DFG between two CO_2 laser lines in GaSe and GaAs. This plot was taken from reference [7].

References

[1] S. Pitois, J. Fatome, and G. Millot, "Generation of a 160-GHz transform-limited pedestal-free pulse train through multiwave mixing compression of a dual-frequency beat signal", Optics Letters, **27**, 19, (2002).

[2] S. Pitois, C. Finot, J. Fatome, B. Sinardet, G. Millot, "Generation of 20-GHz picosecond pulse trains in the normal and anomalous dispersion regimes of optical fibers", Optics Communications, **260**, 301-306 (2006).

[3] J. Fatome, S. Pitois, and G. Millot, "20-GHz-to-1-THz Repetition Rate Pulse Sources Based on Multiple Four-Wave Mixing in Optical Fibers", IEEE Journal of Quantum Electronics, **42**, 10, (2006).

[4] C. A. Kapetanakos, B. Hafizi, H. M. Milchberg, P. Sprangle, R. F. Hubbard, and A. Ting, "Generation of High-Average-Power Ultrabroad-Band Infrared Pulses", IEEE Journal of Quantum Electronics, **35**, 4, (1999).

[5] C. J. Johnson, G. H. Sherman, and R. Weil, "Far Infrared Measurement of the Dielectric Properties of GaAs and CdTe at 300 K and 8 K", Applied Optics, **8**, 8 (1969).

[6] A. M. Ardila, O. Martínez, M. Avella, J Jiménez, B. Gérard, J. Napierala, and E. Gil-Lafon, "Temperature dependence of the Raman shift in GaAs conformal layers grown by hydride vapor phase epitaxy", Journal of Applied Physics, **91**, 8 (2002).

[7] S. Ya. Tochitsky, C. Sung, S. E. Trubnick, C. Joshi, and K. L. Vodopyanov, "High-power tunable, $0.5 - 3$ THz radiation source based on nonlinear difference frequency mixing of CO_2 laser lines", Journal of the Optical Society of America B, **24**, 2509 (2007).

[8] J. Moses and F. W. Wise, "Controllable Self-Steepening of Ultrashort Pulses in Quadratic Nonlinear Media", Physical Review Letters, **97**, 073903 (2006).

Chapter 7

Conclusion

This dissertation has been wholly concerned with the first experimental studies of the third-order nonlinear optics of gases and semiconductors driven by gigawatt power, long-wave infrared (LWIR) radiation. Here, the development of a high-repetition rate CO_2 laser system enabled experiments using 1- 10 GW/cm^2, picosecond pulses at a wavelength of 10 μm. These intensities are three to four orders of magnitude larger than those used in past experiments yet still remain below the ionization threshold of the materials under investigation. As a result, we have been able to study a new regime of LWIR nonlinear optics whereby materials are driven by electric field strengths just below the ionization or damage threshold. The use of such high intensity pulses has enabled major contributions including, the first measurements of the nonlinear refractive index of atomic and molecular gases at a wavelength of 10 μm, the generation of the broadest infrared supercontinuum by nonlinear propagation of 10 μm pulses in GaAs, and the production of ultra-fast 10 μm pulses by four-wave mixing compression in GaAs. Through these experiments, we have shown that the nonlinear optics of gases and semiconductors driven by gigawatt, LWIR radiation is not a trivial extension of the nonlinear optics explored using near-IR lasers. The experiments presented in this dissertation rather suggest that the nonlinear optics of high-intensity, long-wavelength radiation may prove to be a rich sub-field, both for its great practical promise and for furthering our understanding of light-matter interactions.

Future work on the LWIR nonlinear optics of gases might include measurements of the nonlinear refractive index of atomic and molecular gases using shorter, 3 ps, pulses as opposed to the 200 ps pulses that were used for the measurements detailed in Chapter 4. The application

of such short pulses may allow for nonlinear refractive index measurements at a range of intensities from $1 - 100$ GW/cm^2 while still remaining below the threshold for avalanche ionization. These measurements are necessary to understand the origin of the anomalously low electronic nonlinearities observed in Kr and Xe. The use of such short pulses combined with time-resolved nonlinear refractive index measurement techniques may also be used to measure the relative contributions of the electronic and molecular nonlinearities to the effective nonlinear refractive indices of the diatomic molecules N_2 and O_2. Such measurements will be useful in understanding the origin of the large molecular nonlinearities that were observed using 200 ps, 10 μm pulses.

We have shown that the LWIR nonlinear optics of semiconductors may have potential for applications such as white-light generation in the molecular fingerprint region (see Chapter 6). To enable such applications, however, future work in this area should be devoted to basic research since the nonlinear optics of semiconductors in the LWIR is not well understood. For example, we have observed that the effective nonlinear refractive index of GaAs is a strong function of the beat frequency in FWM experiments (see Chapter 6). This observation suggests that the effective nonlinear refractive index of semiconductors may be dependent on the bandwidth of the driving laser pulse. While we have hypothesized that cascaded difference frequency mixing may be the cause of these observations, FWM measurements over a range of beat frequencies available by amplification on various CO_2 laser lines may be used to study this effect in detail and determine whether or not this hypothesis is correct. Aside from the interplay between second- and third-order nonlinearities in semiconductors such as GaAs, the nonlinear optics of semiconductors using $1 - 10$ GW/cm^2 LWIR radiation is an unexplored area of research. Here, experiments using such high intensities may result in optical field ionization and

a shifting of the band-gap via the dynamic Franz-Keldysh effect that is expected to lead to intensity dependent changes to both the linear and nonlinear properties of the material. These considerations underscore the importance of measuring the nonlinear refractive indices of semiconductors driven by intense LWIR radiation.

Appendix A

The design of a Martinez-style, grating-based stretcher for 3 ps, 10.59 μm pulses

We have a designed a Martinez-style [1], grating-based stretcher capable of stretching few picosecond pulses to tens of picoseconds at a wavelength near 10 μm. A simplified diagram of the Martinez-style stretcher is depicted in Fig. A.1, below. The device consists of two diffraction gratings with a 1:1 telescope placed between them. By changing the distance between the focus of the telescope and the second diffraction grating, (G in Fig. A.1) it is possible to achieve both negative and positive group velocity dispersion (GVD). It is possible, therefore, to use a Martinez-style stretcher as either a pulse stretcher or a pulse compressor. It should be noted that both diffraction and refraction always impart negative GVD to a laser pulse unless there is a focusing optic placed between the dispersive elements [1]. As can be seen in Fig. A.1, the input beam is incident on the first diffraction grating and is reflected through the two lenses. After the lenses the beam is incident upon the second diffraction grating that reflects the beam upon a retro-reflector. The retro-reflector sends the beam back along the exact beam path with a shift in the vertical direction, thus reflecting four times from a diffraction grating before leaving the optical system along the same beam path as the input beam.
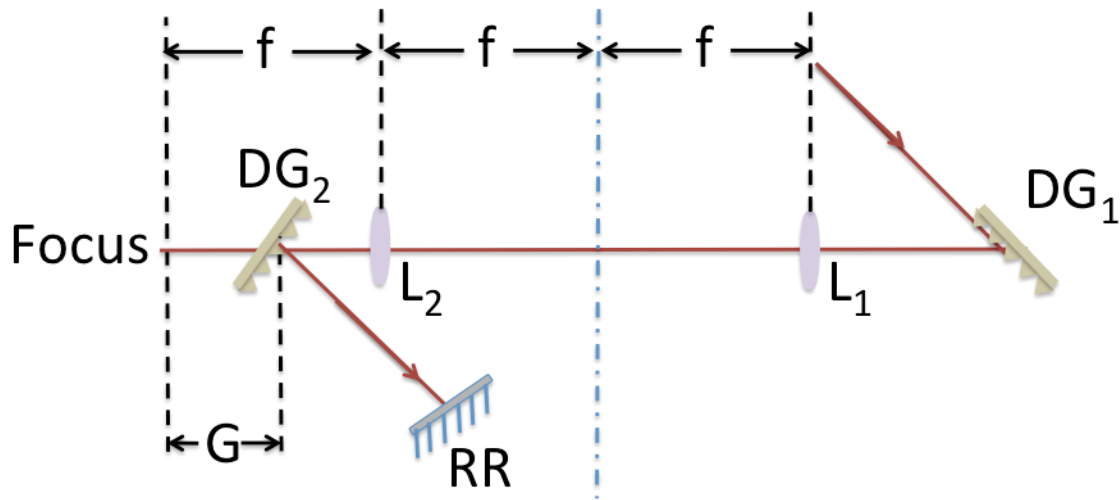
Figure A.1: A schematic of a Martinez-style, grating-based stretcher. $L_{1,2}$ are two lenses with a focal length f, $DG_{1,2}$ are diffraction gratings with the same grating period, RR is a retro-reflector, and G is the distance between the second diffraction grating and the focus of the telescope, used to control dispersion.

Although it is possible to build a stretcher as depicted in Fig. A.1, it is more convenient to build the device in a folded design that can be visualized by folding the schematic of Fig. A.1. about the blue line of symmetry. In this configuration, it is possible to use a single diffraction grating and a single curved mirror thereby saving optics and simplifying the alignment procedure of the device.

Figure A.2 shows a detailed schematic of the grating-based stretcher for 10 μm light. The input beam is sent through an alignment iris and transmitted between the two mirrors of the retro-reflector. The beam is then incident upon a 150 g/mm diffraction grating that reflects the light onto a curved mirror with a focal length of 762 mm. The beam is then transmitted through a second alignment iris and focused on a flat-mirror as depicted in Fig. A.2. The flat mirror reflects the beam back upon the same beam path with a slight shift in the vertical direction such

that the beam intercepts the retro-reflector. The retro-reflector imparts a vertical shift unto the

beam and reflects it back through the system once more such that the beam is incident on the

diffraction grating four times. After the beam's fourth reflection from the diffraction grating it is

reflected from a pick-up mirror and transmitted through the third and final alignment iris.

Finally, Fig. A.3 is a photograph of the actual stretcher, with red lines indicating the path of the

laser beam.
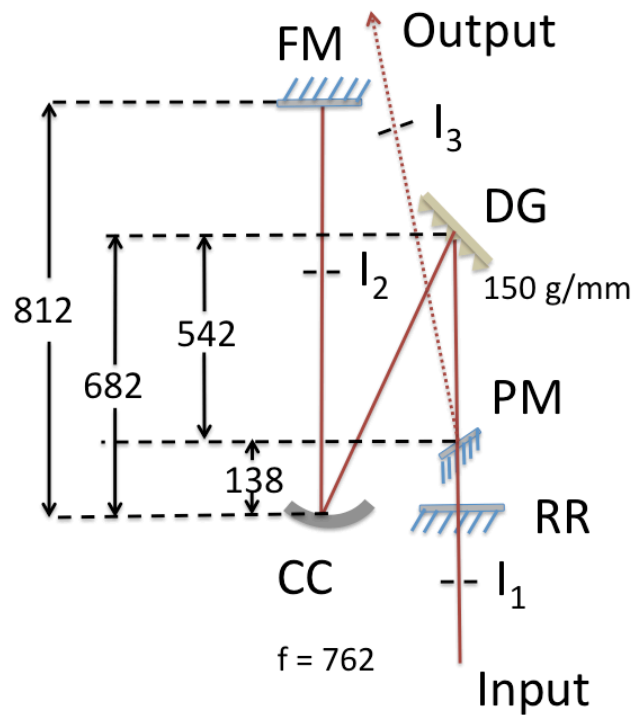
Figure A.2: A schematic of the 10 μm grating-based stretcher. $I_{1,2,3}$ are irises used for alignment

of the system. PM is a pick-up mirror used to reflect the radiation out of the system. DG is the

150 g/mm diffraction grating. CC is a curved mirror with focal length 762 mm and FM is a flat

mirror. All measurements are in millimeters.
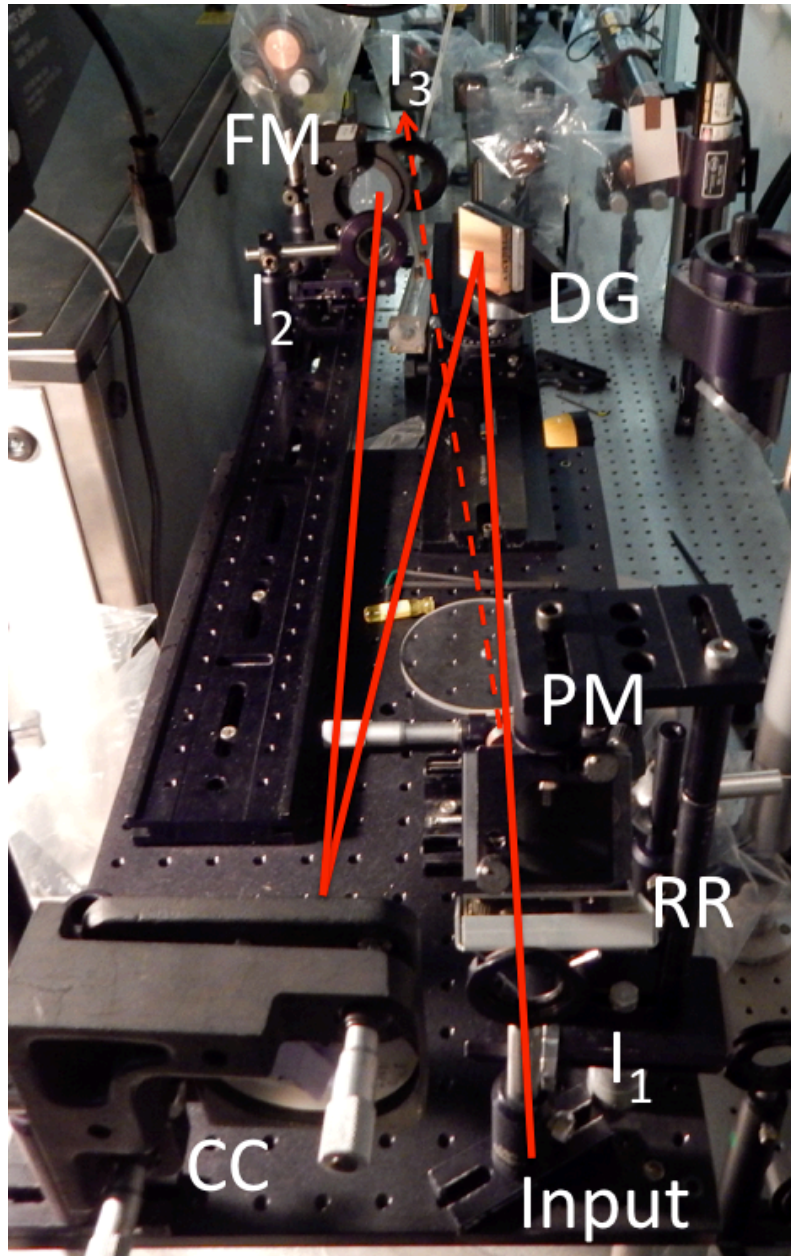
Figure A.3: A photograph of the 10 μm grating-based stretcher. $I_{1,2,3}$ are irises used for alignment of the system. PM is a pick-up mirror used to reflect the radiation out of the system. DG is the 150 g/mm diffraction grating. CC is a curved mirror with focal length 762 mm and FM is a flat mirror.

The initial distances used to build the stretcher were calculated using Lab2 [2], a free

Labview program that is capable of simulating a variety of experiments in ultrafast optics. The

actual distances, shown in Fig. A.2, were found empirically by stretching a ~ 3.5 ps, 10 μm laser

pulse to ~ 20 ps. The stretching factor was measured using a picosecond streak camera.

Temporal measurements were realized by converting the temporal information from the mid-IR

light onto a visible diode laser probe via polarization rotation inside of a CS_2 filled Kerr cell [3].

Figure A.4a and A.4b show show temporal pulse profiles of a 3.5 ps, CO_2 laser pulse train

(see Chapter 2 for more information) with (Fig. A.4b) and without (Fig. A.4a) dispersion. The

dispersed case was measured with the distances indicated in Fig. 4a and the undispersed case was

measured with g of Fig. A.1 set to zero. Note that this was accomplished by setting the distance

from the curved mirror and the flat mirror of Fig. A.2 to 682 mm. As can be seen in Fig. A.4, the

stretcher has increased the pulse duration of the initially 3.5 ps pulses to approximately 20 ps,

thereby transforming the picosecond pulse train into a smooth pulse. It should be noted that the

throughput of the stretcher after optimization was found to be ~ 50%. The spatial beam profile

after the stretcher is shown on the inset of Fig. A.4.
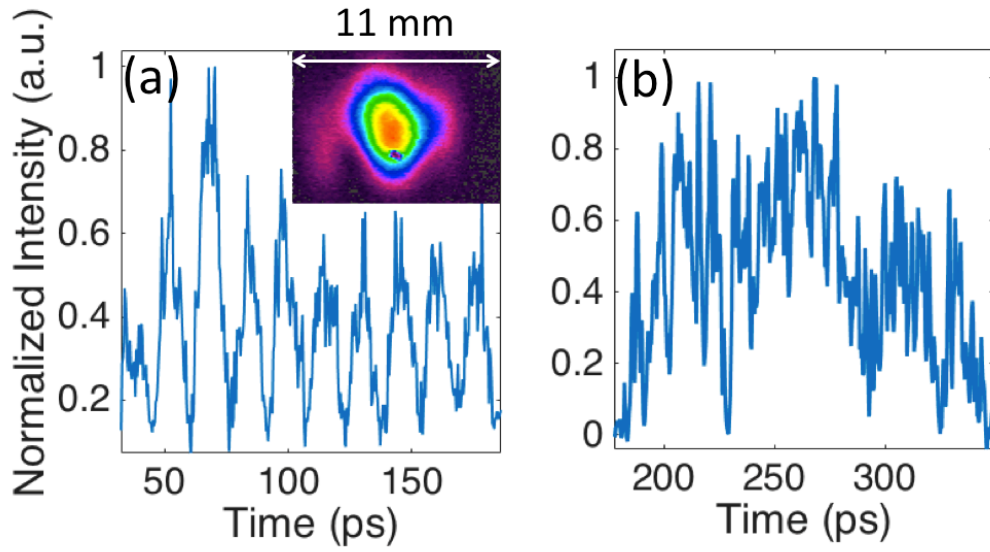
Figure A.4: (a) A temporal pulse profile measured with the stretcher in its nominal (unstretched position) and (b) the temporal pulse profile measured with the distances indicated in Fig. A.2. The inset of the figure is the spatial profile of the output beam as measured with a pyro-electric camera.

Appendix B

Software used to simulate the 2D, cylindrically symmetric generalized nonlinear Schrödinger equation

B.1 Introduction

We have developed a MATLAB code to simulate nonlinear pulse propagation using the cylindrically symmetric, generalized nonlinear Schrödinger equation (GNLSE). The GNLSE is described in Chapter 2 (see Eq. 50 and surrounding discussion) and accounts for diffraction, self-focusing, self-phase modulation (SPM), stimulated Raman scattering (SRS), self-steepening, and dispersion.

The GNLSE is solved using the split-step Fourier method that is described in detail elsewhere [4]. Here the dispersive and diffractive terms are separated from the nonlinear term such that the GNLSE can be expressed as:

$$\frac{\partial \mathcal{E}}{\partial z} = (\widehat{D} + \widehat{N})\mathcal{E} \qquad \text{(A.1)}$$

where $\widehat{D}$ represents the dispersive and diffractive terms and $\widehat{N}$ represents the nonlinear term. In the limit of small longitudinal step-sizes, the field at the next spatial step can be approximated as a function of the field at the previous step:

$$\mathcal{E}(z + h, \tau) \approx \exp h\widehat{D} \exp h\widehat{N}\, \mathcal{E}(z, \tau). \qquad \text{(A.2)}$$

Where h is the step-size. In the standard split-step Fourier method, used to solve the simplified nonlinear Schrödinger equation (see Eq. 49) each spatial step is split in half. In the first half-step, the initial field is Fourier transformed and the diffractive and dispersive operators are solved for in the frequency domain. The field is then inverse Fourier transformed and the nonlinear operator is evaluated in the time-domain for the second half-step. Here, the dispersive and diffractive terms are solved for in the Fourier domain to simplify the spatial and temporal derivatives that appear in the model. It should be noted that, for the GNLSE, both the nonlinear and linear operators must be solved for in the frequency domain in order to account for the time derivative and convolution of the field with the Raman response function (See Eq. 50 of Chapter 2 and surrounding discussion).

To reduce computational time the GNLSE is simulated in a cylindrically-symmetric coordinate system. To solve the diffractive term in the GNLSE the field is transformed into the frequency domain using a Hankel transform. Numerically, the quasi-discrete Hankel transform is computed by a matrix multiplication that can be performed quickly using MATLAB. The description of the Hankel transform and its numerical implementation can be found in references [6] and [7], respectively.

B.2 MATLAB code

```
clear variables;
close all;


% Physical quantities and medium properties
%========================================================
```

```matlab
%Physical parameters describing the radiation


c1 = 2.998e-2; %vacuum speed of light in cm/ps

lambda = 1.06e-4; %Laser central wavelength in cm

nu_0 = c1/lambda;

w0_FWHM = 3e-1;%2e-2; % Initial laser beam radius in cm

w0= 1.1774*w0_FWHM;

f = 200; %Focal length of lens in cm

Chirp = 0;%-2.47; %Initial gaussian chirp parameter (negative is
negative chirp)

k0 = 2*pi/lambda; %Propagation constant in cm ^(-1)

k = n0*k0;

tau_FWHM = 1.5;%50e-3; %Pulse length in ps

tau = 1.1774*tau_FWHM;  %Intial 1/e pulse length in picoseconds


%Medium parameters


n0 = 1.4802;%1.328;  %Refractive index at the carrier frequency

b2 = 7.6959e-4;%2.41e-4; %GVD in ps^2/cm

b3 = 4.2652e-7; %TOD in ps^3/cm

b4 = 1.3826e-10; %FOD in ps^4/cm


K = 5;          %Multiphoton number mod(hw/ui + 1)

beta_k = 0;% 8e-50;%7; %cross section for MPI 5th order
cm^7/GW^4

n2 = 0.80e-15; %Nonlinear index of Benzene in cm2/W literature
value is 1e-15
```

```matlab
n4 = -1e-5;


% Raman parameters


t1 =5.34e-3;%18.6e-3 for GaAs  (8.55 THz) *2 for CdTe 16.3 for
9.76 THz; raman parameter t1 [ps] frequency

t2 = 3.6;%1.32;%1.32;%3;    %originally 3ps for GaAs, 1.2 for
CdTe       % raman parameter t2 [ps] decay time

fr =0.08;%0.10;%0.18;%0.17;%0.245;    %0.25 for GaAs 0.18 for
glass % fraction of chi3 related to raman


%Power and field strength


Pcrit = 3.77*pi*n0/(2*k^2*n2); %critical power for self-focusing

PonPc = 108;%40.5;%50.6;%100; %ratio of the beam power to the
critical power

Power = PonPc*Pcrit; %input peak power in GW

Aeff = pi*w0_FWHM^2; %Effective initial area in mm^2

Int = Power/Aeff;   %Input intensity in GW/cm2

u0 = sqrt(Int); %Initial amplitude of the field sqrt(PeakPower)


%Derived quantities (Length scales etc)


zr = n0*k0*w0^2/2;

L0 = 1/(n2*k0*u0^2);

Ld = tau^2/abs(b2);
```

```matlab
%===============Windows and
discretization=====================

N_t = 2^14;%2^14;  %Number of sampling points

N_r = 2^7;


t_win = 50; %Time window in ps

r_win = 0.7;   %Space window in cm

dt = t_win/N_t;                          % ps

t = -t_win/2:dt:(t_win/2-dt);



%==============================================================



%===============%Fourier space=========================

nu_win = 1/dt;  %nu is in THz

dnu = 1/t_win;

nu = [(0:N_t/2-1),(-N_t/2:-1)]/(dt*N_t);


nu = fliplr(nu);


%  Raman response function



tres = t - t(1);
```

```matlab
hr =((t1^2+t2^2)/(t1*t2^2)).*exp(-tres/t2).*sin(tres/t1);

hrw = fft(hr, N_t);


hrw = 1*hrw;              %Multiplying by a neg. 1
hr = ifft(hrw, N_t);     %ensures that
                         %Stokes grows first JP 4/1/2016



%Diagnostic code to look at raman response function
figure(5)
plot(t, hr/max(hr));
figure(6)
plot(nu, imag(hrw));


%============================%Hankel Transform setting up the
matrices% ============================
ord = 0;       %% Transformation order
load c.mat;
c = c(ord+1,1:N_r+1);


k_win = c(N_r+1)/(2*pi*r_win);    % Maximum frequency
r = c(1:N_r)'*r_win/c(N_r+1);     % Radius vector
k_r = c(1:N_r)'/(2*pi*r_win);     % Frequency vector


[Jn,Jm] = meshgrid(c(1:N_r),c(1:N_r));
C =
```

```matlab
(2/c(N_r+1))*besselj(ord,Jn.*Jm/c(N_r+1))./(abs(besselj(ord+1,Jn
)).*abs(besselj(ord+1,Jm)));



m1 = (abs(besselj(ord+1,c(1:N_r)))/r_win)';    %% m1 prepares
input vector for transformation

m2 = m1*r_win/k_win;                            %% m2 prepares
output vector for display

clear Jn

clear Jm


%new stuff to make the code faster


    m1_inverse = 1./m1;

    m1_inverse_diag = diag(m1_inverse); %Prepare vector for
transform

    m1_diag = diag(m1);


% %============================================================

% %Initialize the field (vertical direction for space,
horizontal for time)

%=================================================

NC = 1e-6;%1e-12;%1e-15; %Input quantum noise


u_t = exp(-(1 + 1i*Chirp)*(t/tau).^2);% + NC*u0*randn(1, N_t);

u_t = u_t + NC*u_t.*randn(1, N_t);

u_r = exp(-(r/w0).^2- 1i*(k0*r.^2)/(2*f));

U0 = u0*u_r*u_t; %Matrix containing the values of the initial
```

```matlab
complex envelope

U = U0;

%u_spec0 = fftshift(fft(fftshift(U0,2), N_t ,2 ),2);

u_spec0 = fft(U0, N_t, 2);

%============Space and time resolution diagnostic===========

%Test code to make sure I have good resolution in space and time

figure (1)

subplot(1,3,1)

plot(nu, abs(u_spec0(1,:)).^2);

xlabel('Frequency (THz)');

ylabel('Spectral density (a.u.)');

% axis([-1, 1, 0, 1])

subplot(1,3,2);

plot( t, abs(U0(1, :)).^2);

xlabel('Time (ps)');

ylabel('Intensity (W/cm^2)')

% axis([-10, 10, 0, 10]);

subplot(1,3,3)

plot(r, abs(U0(:, N_t/2)).^2);

xlabel('Space (cm)');

ylabel('Intensity (W/cm^2)');


figure (300)

plot(t, U0(1, :)/max(U0(1, :)), t, atan(real(U0(1,
:))./imag(U0(1, :)))));
```

```matlab
% %====================Main
calculation===========================


% % Propagate the field through space

L = 13; %40%Propagation distance in cm

dz =3.25e-2;%6.5e-2; %Step size in cm

z_initial = 270; %Used to move the diffraction calculation
forward

steps = L/dz; %# of steps

N_dump = 10;

dump_counter = 1;

u_r_0 = u_r;

u_t_0 = u_t;




%
%================================================================
======

% %  %Main loop for nonlinear pulse propagation

%================================================================
========




total_length = 0;

tic;
```

```matlab
fprintf(1, '\nSimulation running...        ');

interval = steps/N_dump;

data = zeros(N_r, N_t, N_dump);


for ii = 1 : steps



% ====================dispersion operator 1
======================



    %u_spec = fftshift(fft(fftshift(U,2), N_t ,2 ),2);

     u_spec = fft(U, N_t, 2);

    disp_k = 1i*b2/2*(2*pi*nu).^2 + 1i*b3/6*(2*pi*nu).^3  +
1i*b4/24*(2*pi*nu).^4;



     for jj = 1 : size(U,1)

    u_spec(jj, :) = u_spec(jj, :).*exp(disp_k*(dz));

    end



    U = ifft(u_spec, N_t, 2);

    %U = ifftshift(ifft(ifftshift(u_spec,2), N_t ,2 ),2);

%===============================================================
======

%================Diffraction operator
1==============================



 %This if statement is to start the diffraction calculation at
```

```matlab
 %another Z location other than Z = 0.


if ii == 1

U_r = m1_inverse_diag*U;     %prepare vector for transform

U_kspec = C*U_r;             %Hankel transform

kk = (-1i*(z_initial)*(2*pi*k_r).^2)/(2*k0);

U_kspec = diag(exp(kk))*U_kspec;

U_r = C*U_kspec;                         %Inverse Hankel transform

U= m1_diag*U_r;                           %prepare matrix for
display

end




U_r = m1_inverse_diag*U;     %prepare vector for transform

U_kspec = C*U_r;             %Hankel transform


kk = (-1i*(dz)*(2*pi*k_r).^2)/(2*k0);

U_kspec = diag(exp(kk))*U_kspec;

U_r = C*U_kspec;                         %Inverse Hankel transform

U= m1_diag*U_r;                           %prepare matrix for
display
```

```matlab
%==============================================================
=====




%================Nonlinear operator
==============================


for jj = 1 : size(U,1)

    %U(jj, :) = U(jj, :).*exp(1i*(n2*k0*((abs(U(jj,
:))).^2)*(dz)) - (beta_k/2)*(abs(U(jj, :))).^(2*(K-1))*dz);

    ie_spec = fft(U(jj, :).*abs(U(jj, :)).^2, N_t);

    i_spec = fft(abs(U(jj, :)).^2, N_t);

    U_spec = fft(U(jj,:), N_t);

    rconv = ifft(hrw.*i_spec, N_t);

    rr = fft(U(jj,:).*rconv, N_t);




    K_NLfd = 1i*dz*n2*k0*((1-fr)*ie_spec +fr*dt*rr);

    K_NLfd = (1 + (nu/nu_0)).*K_NLfd;

    U_spec = U_spec + K_NLfd;

    U(jj, :) = ifft(U_spec, N_t);

    U(jj, :) = U(jj, :).*exp(-dz*(beta_k/2)*(abs(U(jj,
:))).^(2*(K-1)));

end
```

117

```matlab
%=================================================================
=====



    if mod(ii, interval) == 0

        data(:, :, ii/interval) = U;

    end




total_length = total_length + dz;

    fprintf(1, '\b\b\b\b\b\b%5.2f%%', total_length * 100.0 /L )



end
%
final_lineout_center_cylindrical;
radial_evolution;
```

Appendix C

MATLAB code to calculate the uncertainty of best fit lines for nonlinear refractive index measurements in atomic and molecular gases.

```matlab
close all;

clear all;

clc;



file1 = sprintf('5-17-16_S1/minus15inHg_Kr_751pm');

file2 = sprintf('5-17-16_S1/minus15inHg_He_729pm');



path1 =
strcat('/Users/jeremypigeon/Documents/Science/Experimental
data/data 2016/2016 Large Bunker Data/', file1);

path2 =
strcat('/Users/jeremypigeon/Documents/Science/Experimental
data/data 2016/2016 Large Bunker Data/', file2);

data1=load(path1);

one = data1;

data2=load(path2);

two = data2;



ii = 1;

n = size(data1,1);

Rmax = 10;   %Maximum allowed ratio between lambda1 and lambda2
```

```matlab
while ii < n+1 ;

  if data1(ii,4) <Rmax^(-1) || data1(ii,4) > Rmax


      data1(ii,:) = [];
      n = n - 1;
  end


  ii = ii +1;
end


ii = 1;
n = size(data2,1);


while ii < n +1;

  if data2(ii,4) <Rmax^(-1) || data2(ii,4) > Rmax


      data2(ii,:) = [];
      n = n - 1;
  end
  ii = ii + 1;
end
%Note that data(:,3) is 10.27 um and data(:,2) is 10.59 um
%Converting everything to real energy units:
```

```matlab
%FWM signal from volts to uJ

data1(:,1) = data1(:,1)*1e3;   %volts to mV

data1(:,1) = data1(:,1)*(2.2/15); %2.2 pJ/15 mV for LN2 HCT

data1(:,1) = data1(:,1)*1e-6;   %converting from pJ to uJ

data1(:,1) = data1(:,1)/1.2e-3; % In uJ factor is attenuation
through spect.


data2(:,1) = data2(:,1)*1e3;   %volts to mV

data2(:,1) = data2(:,1)*(2.2/15); %2.2 pJ/15 mV for LN2 HCT

data2(:,1) = data2(:,1)*1e-6;   %converting from pJ to uJ

data2(:,1) = data2(:,1)/1.2e-3; % In uJ


%==============================
%2.34 is the attenuation at 10.93 $\mu$m for the 2 mm CaF2

%(only noble gas measurements)


data1(:,1) = data1(:,1)*2.34;
data2(:,1) = data2(:,1)*2.34;


%===============================

%Lambda1 and Lambda2 from mV to uJ
data1(:,2) = data1(:,2)*607e3; %(543.2e3 uJ/V)

data2(:,2) = data2(:,2)*607e3;% (1517 uJ/V) 2/16/16 meas.
```

```matlab
data1(:,3) = data1(:,3)*856.5e3; %1517.6e3;  after taking CaF2

data2(:,3) = data2(:,3)*856.5e3;%1517.6e3; into account


y1 = data1(:,1);

y2 = data2(:,1);


x1 = (data1(:,2).^2).*data1(:,3);

x2 = (data2(:,2).^2).*data2(:,3);

%

%   x1 = data1(:,3);

%   x2 = data2(:,3);

%

  figure (1)


  [fit1, gof1] = fit(x1, data1(:,1), 'poly1');

  [fit2, gof2] = fit(x2, data2(:,1), 'poly1');


  hold on

  plot(fit1, x1,  data1(:,1),'o')

  plot(fit2, x2, data2(:,1),'x');

  leg = legend(file1, 'Fit1', file2, 'Fit2');

  %set(leg, 'Interpreter', 'none');  %turns Matlab Latex
interpreter off


  title(sprintf('R_m_a_x=%6.3g; m_1 = %6.3g, m_2 = %6.3g',Rmax,
fit1.p1, fit2.p1));
```

```
%axis([0 5e-5 0 3])

ylabel('W_1_0_._9 (\muJ)');

xlabel('W_1_0_._6^2 W_1_0_._3 (\muJ^3)');


%Code to look at uncertainty in slope

cf = fit2;

cf_coeff = coeffvalues(cf);

cf_confint = confint(cf);

a = cf_coeff(1);

b = cf_coeff(2);

a_uncert = (cf_confint(2,1) - cf_confint(1,1))/2;

b_uncert = (cf_confint(2,2) - cf_confint(1,2))/2;


sigma = (a_uncert/2)/cf.p1


b3 = 5.737e2;   %Prop constant in mm-1

A3 = 12.57;     %Area of stokes beam mm^2

I = 868.39;    %Result of numerical integration in mm^-4

tau = 197e-12;   %pulse length in picoseconds


del_m = fit1.p1 - fit2.p1;   %Slope difference in uJ^-2;


del_m = del_m*1e12; %converting units to J^-2;


n2 = sqrt(sqrt(3)*del_m/A3)*tau/(b3*I);
```

```
n2 = n2*1e-2
```

Appendix D

Cascaded Quadratic Nonlinearities

Phase-mismatched second-order nonlinear optical processes can create an effective nonlinear phase shift similar to the one produced via the third-order nonlinearity SPM. This was first recognized theoretically in 1967 [7] and has been observed experimentally as early as 1972 in mid-IR four-wave mixing experiments in GaAs [8]. However, it was only when this process was studied in detail in near-IR nonlinear index measurements of KTP [9] that this subject has become a mainstream part of contemporary nonlinear optics research [*e.g.* 10, 11]. In this situation, the total nonlinear index is modified by cascaded quadratic nonlinearities as:

$$n_{2,eff} = n_2 \pm n_{2,casc}. \tag{D.1}$$

Where $n_{2,casc}$ is the change in the nonlinear index from cascaded quadratic nonlinearities. This nonlinearity can be positive (self-focusing) or negative (self-defocusing) and its magnitude is a function of the phase-mismatch Δk. This nonlinearity can arise from any three-wave mixing process and can play an important role in materials with large second-order nonlinearities. Semiconductors that will be studied in this thesis have a formidable second-order nonlinearity.

Although nonlinear phase shifts can arise from any three-wave mixing process, only cascading from second harmonic generation has been studied experimentally [8 – 10]. In this situation, the correction to the third-order nonlinearity can be derived using coupled wave analysis. Using equation (2.5) of Chapter 2 the differential equation governing the fundamental field is:

$$\frac{\partial}{\partial z} \mathcal{E}(\omega_0) \approx -\frac{i\mu_0 \epsilon_0 \omega_0^2}{2k(\omega_0)} P_{NL}(\omega_0) \exp{-i\omega_0 t + ik(\omega_0)z} \tag{D.2}$$

The nonlinear polarizability oscillating at the fundamental frequency and describing the conversion of second harmonic back to the fundamental field is:

$$P_{NL}(\omega_0) = \frac{\epsilon_0}{2}\chi^{(2)}(\omega_0 = 2\omega_0 - \omega_0)\mathcal{E}(2\omega_0)\mathcal{E}^*(\omega_0)\exp\left[-i\omega_0 t - i\big(k(2\omega_0) - k(\omega_0)\big)z\right]$$

(D.3)

Substitution of Eq. D.3 into Eq. D.2 and contracting the syntax for the second-order susceptibility yields the following:

$$\frac{\partial}{\partial z}\mathcal{E}(\omega_0) = -\frac{i\mu_0\epsilon_0\omega_0^2}{4k(2\omega_0)}\mathcal{E}(2\omega_0)\mathcal{E}^*(\omega_0)\exp i\Delta kz \qquad \text{(D.4)}$$

Where Δk is the phase-mismatch for second harmonic generation defined in equation (2.8) of Chapter 2. Fortunately, we have derived a solution for the second harmonic field for the case in which the pump is not depleted in Chapter 2. Substitution of Eq. 2.9 of Chapter 2 into Eq. D.4 and using the definition of intensity, $I(\omega) = \frac{c\epsilon_0 n(\omega)}{2}\mathcal{E}(\omega)\mathcal{E}^*(\omega)$, gives the following expression for the evolution of the fundamental field:

$$\frac{\partial}{\partial z}\mathcal{E}(\omega_0) = -i\frac{\omega_0}{c}\left[\frac{{\chi^{(2)}}^2\omega_0}{8\Delta kn^2(\omega_0)n(2\omega_0)c^2\epsilon_0}\right]I(\omega_0)\mathcal{E}(\omega_0)(1 - \exp i\Delta kz) \qquad \text{(D.5)}$$

The second term of Eq. D.5 is similar in form to that of Eq. 2.7 and Eq. 2.13. After integration, this part of Eq. D.5 will describe the familiar oscillations of the amplitude of the fundamental field related to a finite coherence length. The first term of Eq. D.5, however, is similar in form to Eq. 2.17 that is responsible for SPM. The first term in Eq. D.5 will manifest in nonlinear phase changes to the fundamental field where the term $\left[\frac{{\chi^{(2)}}^2\omega_0}{8\Delta kn^2(\omega_0)n(2\omega_0)c^2\epsilon_0}\right]I(\omega_0)$ appears as a change

to the linear index of refraction. For this situation, the change to the nonlinear index from second-order effects, $n_{2,casc}$, is:

$$n_{2,casc} = \frac{1}{\Delta k} \frac{\omega_0 \chi^{(2)^2}}{8c^2 \epsilon_0 n^2(\omega_0) n(2\omega_0)} \tag{D.6}$$

The most important difference between the intensity dependent refractive index that arises from cascaded quadratic nonlinearities versus the third-order response (see Eq. 2.19) is that its magnitude depends on the phase-mismatch Δk. Equation D.6 is limited, however, in that it predicts that the nonlinear index infinity when the phase-match is zero. In reality, the nonlinear index from cascaded quadratic nonlinearities must tend to zero for the case that the three-wave mixing process is perfectly phase-matched. This can be explained by considering a physical picture of SPM via phase-mismatched second harmonic generation.

For a finite phase mismatch, a fraction of the fundamental field will be converted to the second harmonic until the field traverses two coherence lengths, upon which the second harmonic will convert back to the fundamental field. Under normal dispersion conditions, however, the second harmonic has a larger refractive index than the fundamental field. As a result, the fundamental field will suffer a change in its phase after it is converted back from the second harmonic. Further, since the second harmonic generation process is intensity-dependent, these cycles of conversion and back-conversion result in a nonlinear phase shift to the fundamental. Therefore, there is no nonlinear phase shift when the phase matching condition is perfect because the second harmonic does not convert back to the fundamental.

In semiconductors such as GaAs and CdTe, difference frequency generation (DFG) can be phase-matched by the anomalous dispersion of the phonon band to produce THz radiation by

mixing mid-IR frequencies [12, 13]. This effect may change the observed cubic nonlinearity, especially in FWM experiments. Since this thesis will present experiments on FWM in semiconductors it is important to describe this process.

Considering the case of non-degenerate FWM depicted in Fig. 1b, let the DFG angular frequency be denoted by $\Omega = \omega_2 - \omega_1$. The nonlinear polarizability for the THz wave is:

$$P_{NL}(\Omega) = \frac{\epsilon_0}{2}\chi^{(2)}\mathcal{E}_2\mathcal{E}_1^* \exp i[\omega_2 t - \omega_1 t - k(\omega_2)z + k(\omega_1)z] \qquad \text{(D.7)}$$

Where $\mathcal{E}_q$ is the complex envelope at frequency ω_q of Fig. 1b. Note that the THz wave can also be generated via $\Omega = \omega_1 - \omega_3$ and $\Omega = \omega_4 - \omega_2$ but these processes will be neglected under the assumption that $\mathcal{E}_{1,2} \gg \mathcal{E}_{3,4}$. Substitution of Eq. D.7 into Eq. 2.5 of Chapter 2 yields the following differential equation governing the growth of the DFG frequency:

$$\frac{d}{dz}\mathcal{E}(\Omega) = -\frac{i\Omega^2\mu_0\epsilon_0}{4k(\Omega)}\chi^{(2)}\mathcal{E}_2\mathcal{E}_1^* \exp -i\Delta k_{DFG}z. \qquad \text{(D.8)}$$

Where Δk_{DFG} is the phase-matching condition for DFG, $\Delta k_{DFG} = k(\omega_2) - k(\omega_1) - k(\Omega)$. Integrating Eq. D.8 under the assumption that the two pump fields are constant yields:

$$\mathcal{E}(\Omega) \approx \frac{\Omega^2\mu_0\epsilon_0}{4k(\Omega)}\frac{\mathcal{E}_2\mathcal{E}_1^*}{\Delta k_{DFG}}\left(e^{-i\Delta k_{DFG}z} - 1\right) \qquad \text{(D.9)}$$

Next, we consider how radiation at angular frequencies $\omega_{3,4}$ can be generated via three-wave mixing. The most efficient channels are $\omega_3 = \omega_1 - \Omega$ and $\omega_4 = \omega_2 + \Omega$ for which the nonlinear polarizabilities are:

$$P_{NL}(\omega_3) = \frac{\epsilon_0}{2}\chi^{(2)}\mathcal{E}_1\mathcal{E}_\Omega^* \exp(i\omega_1 t - i\Omega t - ik(\omega_1)z + ik(\Omega)z) \quad \text{(D.10)}$$

and,

$$P_{NL}(\omega_4) = \frac{\epsilon_0}{2} \chi^{(2)} \mathcal{E}_2 \mathcal{E}_\Omega \exp(i\omega_2 t + i\Omega t - ik(\omega_2)z - ik(\Omega)z) \quad \text{(D.11)}$$

Where $\mathcal{E}_\Omega$ is the complex amplitude of the THz wave. It is worth mentioning that the generation of light through the nonlinear polarizability in Eq. D.10 should be much more efficient than that generated through Eq. D.11 since $\mathcal{E}_\Omega \ll \mathcal{E}_{3,4} \ll \mathcal{E}_{1,2}$. This is because Eq. D.10 describes the creation of photons at ω_3 and Ω by the annihilation of photons at ω_1. In contrast, Eq. D.11 describes the creation of photons at ω_4 by the annihilation of photons at both ω_2 and Ω. We should, therefore, expect spectral asymmetry if cascaded DFG plays a role in FWM experiments.

To understand how cascading quadratic nonlinearities can alter the four-wave mixing process we substitute Eq. D.10 into Eq. 2.5 of Chapter 2:

$$\frac{d}{dz}\mathcal{E}_3 = -\frac{i\omega_3^2 \mu_0 \epsilon_0}{4k(\omega_3)} \chi^{(2)} \mathcal{E}_1 \mathcal{E}_\Omega^* \exp{-i\Delta k_{TWM} z} \,. \quad \text{(D.12)}$$

Where Δk_{TWM} is the phase-mismatch for this three-wave mixing process and is given by:

$$\Delta k_{TWM} = k(\omega_1) - k(\Omega) - k(\omega_3). \quad \text{(D.13)}$$

The final step is to substitute Eq. D.9 into Eq. D.10 and to compare this result with the four-wave mixing expression of Eq. 2.13. Substitution of Eq. D.9 into Eq. D.12 yields:

$$\frac{d}{dz}\mathcal{E}_3 = -\frac{i\omega_3}{4n(\omega_3)} \frac{1}{c^2} \frac{\Omega}{4n(\Omega)} [\chi^{(2)}]^2 \frac{\mathcal{E}_1^2 \mathcal{E}_2^*}{\Delta k_{DFG}} \left(e^{-i\Delta k_{FWM} z} - e^{-i\Delta k_{TWM} z}\right). \quad \text{(D.14)}$$

Where Δk_{FWM} is the phase-mismatch for four-wave mixing defined by $\Delta k = 2k(\omega_1) - k(\omega_2) - k(\omega_3)$. As can be inferred from above, the evolution of the field at ω_3 from the second-order nonlinearity has two terms. The second term is the usual three-wave mixing term and the first manifests exactly like four-wave mixing from the third-order nonlinearity. If the

complex amplitudes are converted into intensity units then the nonlinear index from this process

takes the following form:

$$n_{2,casc} = \frac{1}{\Delta k_{DFG}} \frac{\Omega[\chi^{(2)}]^2}{8c^2\epsilon_0 n(\Omega)n(\omega_1)\sqrt{n(\omega_2)n(\omega_3)}}. \tag{D.15}$$

Which is very similar in form to the cascaded second harmonic equivalent presented in Eq. D.6.

It should be noted that, while cascaded quadratic nonlinearities may manifest as a positive or

negative change to the nonlinear index, in most situations cascaded quadratic nonlinearities act to

reduce the intrinsic, third-order nonlinearity.

Appendix E

Simple Derivation of Miller's Rule to Estimate the Dispersion of the Third-order Nonlinearity of Gases

There are a number of models that have been put forth to estimate the dispersion of the third-order susceptibility [11, 12]. For gases, the most widely used model is the so-called Miller's rule that was originally developed to estimate the dispersion of the second-order nonlinearity in solids [12] and was later extended to estimate the dispersion of the third-order nonlinearity [13]. In this section, we present a simple, frequency-domain derivation of the Miller's rule wavelength scaling for the third-order susceptibility. It should be noted that a more rigorous, time-domain derivation of Miller's rule for the third-order susceptibility is presented in references [13, 14].

We begin the derivation by considering the equation of motion for a driven anharmonic oscillator:

$$\frac{d^2}{dt^2}r + \gamma \frac{d}{dt}r + \omega_0^2 r = -\frac{eE}{m}. \tag{E.1}$$

Where r is the radial position, γ is the damping term, ω_0 is the angular frequency of the oscillator, e is the charge of the electron, m is the mass of the electron and E is the electric field of the laser. Next we allow the radial position to be expressed as a perturbation series,

$$r(t) = r_0 + \delta r_1 + \delta^2 r_2. \tag{E.2}$$

Where δ is a smallness parameter and r_n represents the nth order of the perturbation series. To look for third-order nonlinearities we include a term cubic in the radial position in Eq. E.1 as follows,

$$\frac{d^2}{dt^2}r + \gamma \frac{d}{dt}r + \omega_0^2 r + \delta r^3 = -\frac{eE}{m}. \tag{E.3}$$

Next we limit ourselves to self-phase modulation type nonlinearities such that the photon conservation of energy argument is $\omega = \omega + \omega - \omega$. This ensures that all terms in Eq. E.3 oscillate at angular frequency, ω, thereby allowing us to express Eq. E.3 as:

$$\omega^2 \, \tilde{r} - i\omega\gamma\tilde{r} + \omega_0^2\tilde{r} + \delta\tilde{r}^3 = -\frac{e\tilde{E}}{m}.$$

(E.4)

Where the tilde denotes the Fourier transform and we have assumed that time derivatives can be replaced by $-i\omega$. Next, we substitute the frequency-domain version of Eq. E.2 into Eq. E.4 yielding,

$$\omega^2 \, (\tilde{r}_0 + \delta\tilde{r}_1 + \delta^2\tilde{r}_2) - i\omega\gamma(\tilde{r}_0 + \delta\tilde{r}_1 + \delta^2\tilde{r}_2) + \omega_0^2(\tilde{r}_0 + \delta\tilde{r}_1 + \delta^2\tilde{r}_2) + \delta(\tilde{r}_0 + \delta\tilde{r}_1 +$$

$$\delta^2\tilde{r}_2)^3 = -\frac{e\tilde{E}}{m}. \tag{E.5}$$

Neglecting higher-order terms and solving Eq. E.5 for the zeroth order term results in the familiar Lorentzian lineshape function,

$$\tilde{r}_0 = -\frac{\frac{e\tilde{E}}{m}}{(\omega^2 - i\gamma\omega + \omega_0^2)} = -\frac{e\tilde{E}}{m} Z(\omega). \tag{E.6}$$

To solve Eq. E.5 for the first order perturbation, we neglect higher order terms yielding,

$$\omega^2 \, (\delta\tilde{r}_1) - i\omega\gamma(\delta\tilde{r}_1) + \omega_0^2(\delta\tilde{r}_1) + \delta(\tilde{r}_0^3) = 0. \tag{E.7}$$

By substituting Eq. E.6 into Eq. E.7 we are able to solve for the first-order perturbation,

$$\tilde{r}_1 = \left(-\frac{e\tilde{E}}{m}\right)^3 (Z(\omega))^4. \tag{E.8}$$

132

Using the definition of the polarizability, $P(\omega)$, in the frequency domain as

$$\tilde{P}(\omega) = -Ne\tilde{r}(\omega) = \tilde{P}_1(\omega) + \tilde{P}_3(\omega) + \cdots \qquad (\text{E.9})$$

it is possible to relate the polarizability to the radial coordinate such that the polarizability becomes:

$$\tilde{P}(\omega) = -Ne\left(-\frac{e\tilde{E}}{m}Z(\omega) - \delta\left(\frac{e\tilde{E}}{m}\right)^3 Z^4(\omega) + \cdots\right). \qquad (\text{E.10})$$

The first order term, related to the linear response, is defined as $\tilde{P}_1(\omega) = \epsilon_0\chi^{(1)}(\omega)\tilde{E}(\omega)$ such that the first-order susceptibility is given by:

$$\chi^{(1)}(\omega) = \frac{Ne^2}{\epsilon_0 m}Z(\omega). \qquad (\text{E.11})$$

The third-order polarizability is defined as $\tilde{P}_3(\omega) = \epsilon_0\chi^{(3)}(\omega)\tilde{E}(\omega)\tilde{E}(\omega)\tilde{E}(\omega)$ such that the third-order susceptibility can be expressed as:

$$\chi^{(3)}(\omega) = \frac{Ne^4}{\epsilon_0 m^3}Z^4(\omega). \qquad (\text{E.12})$$

Finally, by comparing Eq. E.11 and Eq. E.12 we can express the third-order susceptibility in terms of the first-order susceptibility as:

$$\chi^{(3)}(\omega) = \frac{\epsilon_0 m}{N^3 e^4}\left(\chi^{(1)}(\omega)\right)^4. \qquad (\text{E.13})$$

The above is a succinct form of Miller's rule [13] for the third-order polarizability. A more general form, allowing any four-wave mixing process can be expressed as:

$$\chi^{(3)}(\omega_4 = \omega_1 + \omega_2 + \omega_3) = \frac{\epsilon_0 m}{N^3 e^4}\chi^{(1)}(\omega_1)\chi^{(1)}(\omega_2)\chi^{(1)}(\omega_3)\chi^{(1)}(\omega_4). \qquad (\text{E.14})$$

The above predicts that the nonlinear susceptibility is less dispersive than the first-order susceptibility. For the atomic and molecular gases considered in Chapter 4 of this dissertation, Miller's rule predicts that the nonlinear index of refraction should change by $1 - 2$ % when changing the driving laser wavelength from 1 to 10 μm.

References

[1] O. E. Martinez, "3000 Times Grating Compressor with Positive Group Velocity Dispersion: Application to Fiber Compensation in 1.3-1.6 μm Region", IEEE Journal of Quantum Electronics, **23**, 1, 59-64 (1987).

[2] B. Schmidt, M. Hacker, G.Stobrawa, T. Feurer, LAB2-A virtual femtosecond laser lab, http://www.lab2.de.

[3] C. V. Filip, R. Narang, S. Ya. Tochitsky, C. E. Clayton, and C. Joshi, "Optical Kerr switching technique for the production of picosecond, multiwavelength CO_2 laser pulse", Applied Optics, **41**, 18, 3743-3747 (2002).

[4] G. P. Agrawal, *Nonlinear Fiber Optics*, Academic Press, New York (2001)

[5] L. Yu, M. Huang, M. Chen, W. Chen, W. Huang, and Z. Zhu, "Quasi-discrete Hankel Transform" Opt. Lett. Vol. 23, No. 6 (1998).

[6] M. Guizar-Sicairos and J. C. Gutierrez-Vega, "Computation of quasi-discrete Hankel transforms of integer order for propagating optical wave fields" J. Opt. Soc. Am. A. Vol. 21, No.1 (2004)

[7] L. A. Ostrovskii, "Self-action of light in crystals", Journal of Experimental and Theoretical Physics Letters, **5**, 272-275 (1967).

[8] E. Yablonovitch, C. Flytzanis, and N. Bloembergen, "Anisotropic interference of three-wave and double two-wave mixing in GaAs", Physical Review Letters, **29**, 865-868 (1972).

[9] R. DeSalvo, D. J. Hagan, M. Sheik-Bahae, G. Stegeman, E. W. Van Stryland, and H. Vanherzeele, "Self-focusing and self-defocusing by cascaded second-order effects in KTP", Optics Letters, **17**, 1 (1992).

[10] J. Moses and F. W. Wise, "Controllable Self-Steepening of Ultrashort Pulses in Quadratic Nonlinear Media", Physical Review Letters, **97**, 073903 (2006).

[11] E. L. Dawes, "Optical Third-Harmonic Coefficients for the Inert Gases", Physical Review, **169**, 1 (1968)

[12] R. C. Miller, "Optical Second Harmonic Generation in Piezoelectric Crystals", Applied Physics Letters, **5**, 1 (1964)

[13] A. Owyoung, Ph.D. thesis, California Institute of Technology, 1972.

[14] W. Ettoumi, Y. Petit, J. Kasparian, and J. –P. Wolf, "Generalized Miller Formulae", Optics Express, **18**, 7 (2010).